UNIVERSITÉ LAVAL

Design and Analysis of GFDM-Based Wireless Communication Systems

Thèse

Yanpeng Wang

Doctorat en génie électrique
Philosophiæ doctor (Ph. D.)

Québec, Canada

Design and Analysis
of GFDM-Based Wireless Communication Systems

Thèse

Yanpeng Wang

Sous la direction de:

Paul Fortier, directeur de recherche

Résumé

Le multiplexage généralisé par répartition en fréquence (GFDM), une méthode de traitement par blocs de modulation multiporteuses non orthogonales, est une candidate prometteuse pour les technologies de forme d'onde pour les systèmes sans fil au-delà de la cinquième génération (5G). La capacité du GFDM à ajuster de manière flexible la taille du bloc et le type de filtres de mise en forme des impulsions en fait une méthode appropriée pour répondre à plusieurs exigences importantes, comme une faible latence, un faible rayonnement hors bande (OOB) et des débits de données élevés. En appliquant aux systèmes GFDM la technique des systèmes à entrées multiples et sorties multiples (MIMO), la technique de MIMO massif ou des codes de contrôle de parité à faible densité (LDPC), il est possible d'améliorer leurs performances. Par conséquent, l'étude de ces systèmes combinés sont d'une grande importance théorique et pratique.

Dans cette thèse, nous étudions les systèmes de communication sans fil basés sur le GFDM en considérant trois aspects. Tout d'abord, nous dérivons une borne d'union sur le taux d'erreur sur les bits (BER) pour les systèmes MIMO-GFDM, technique qui est basée sur des probabilités d'erreur par paires exactes (PEP). La PEP exacte est calculée en utilisant la fonction génératrice de moments (MGF) pour les détecteurs à maximum de vraisemblance (ML). La corrélation spatiale entre les antennes et les erreurs d'estimation de canal sont prises en compte dans l'environnement de canal étudié. Deuxièmement, les estimateurs et les précodeurs de canal de faible complexité basés sur une expansion polynomiale sont proposés pour les systèmes MIMO-GFDM massifs. Des pilotes sans interférence sont utilisés pour l'estimation du canal basée sur l'erreur quadratique moyenne minimale (MMSE) pour lutter contre l'influence de la non-orthogonalité entre les sous-porteuses dans le GFDM. La complexité de calcul cubique peut être réduite à une complexité d'ordre au carré en utilisant la technique d'expansion polynomiale pour approximer les inverses de matrices dans l'estimation MMSE conventionnelle et le précodage. De plus, nous calculons les limites de performance en termes d'erreur quadratique moyenne (MSE) pour les estimateurs proposés, ce qui peut être un outil utile pour prédire la performance des estimateurs dans la région de E_s/N_0 élevé. Une borne inférieure de Cramér-Rao (CRLB) est dérivée pour notre modèle de système et agit comme une référence pour les estimateurs. La complexité de calcul des estimateurs de canal proposés et des précodeurs et les impacts du degré du polynôme sont également étudiés. Enfin, nous analysons les performances de la probabilité d'erreur des systèmes GFDM combinés aux codes LDPC. Nous dérivons d'abord les expressions du ratio de vraisemblance logarithmique (LLR) initiale qui sont utilisées dans le décodeur de l'algorithme de

somme de produits (SPA). Ensuite, basé sur le seuil de décodage, nous estimons le taux d'erreur de trame (FER) dans la région de bas E_b/N_0 en utilisant le BER observé pour modéliser les variations du canal. De plus, une borne inférieure du FER du système est également proposée basée sur des ensembles absorbants. Cette borne inférieure peut agir comme une estimation du FER dans la région de E_b/N_0 élevé si l'ensemble absorbant utilisé est dominant et que sa multiplicité est connue. La quantification a également un impact important sur les performances du FER et du BER. Des codes LDPC basés sur un tableau et construit aléatoirement sont utilisés pour supporter les analyses de performances. Pour ces trois aspects, des simulations et des calculs informatiques sont effectués pour obtenir des résultats numériques connexes, qui vérifient les méthodes proposées.

Abstract

Generalized frequency division multiplexing (GFDM) is a block-processing based non-orthogonal multi-carrier modulation scheme, which is a promising candidate waveform technology for beyond fifth-generation (5G) wireless systems. The ability of GFDM to flexibly adjust the block size and the type of pulse-shaping filters makes it a suitable scheme to meet several important requirements, such as low latency, low out-of-band (OOB) radiation and high data rates. Applying the multiple-input multiple-output (MIMO) technique, the massive MIMO technique, or low-density parity-check (LDPC) codes to GFDM systems can further improve the systems performance. Therefore, the investigation of such combined systems is of great theoretical and practical importance.

This thesis investigates GFDM-based wireless communication systems from the following three aspects. First, we derive a union bound on the bit error rate (BER) for MIMO-GFDM systems, which is based on exact pairwise error probabilities (PEPs). The exact PEP is calculated using the moment-generating function (MGF) for maximum likelihood (ML) detectors. Both the spatial correlation between antennas and the channel estimation errors are considered in the investigated channel environment. Second, polynomial expansion-based low-complexity channel estimators and precoders are proposed for massive MIMO-GFDM systems. Interference-free pilots are used in the minimum mean square error (MMSE) channel estimation to combat the influence of non-orthogonality between subcarriers in GFDM. The cubic computational complexity can be reduced to square order by using the polynomial expansion technique to approximate the matrix inverses in the conventional MMSE estimation and precoding. In addition, we derive performance limits in terms of the mean square error (MSE) for the proposed estimators, which can be a useful tool to predict estimators performance in the high E_s/N_0 region. A Cramér-Rao lower bound (CRLB) is derived for our system model and acts as a benchmark for the estimators. The computational complexity of the proposed channel estimators and precoders, and the impacts of the polynomial degree are also investigated. Finally, we analyze the error probability performance of LDPC coded GFDM systems. We first derive the initial log-likelihood ratio (LLR) expressions that are used in the sum-product algorithm (SPA) decoder. Then, based on the decoding threshold, we estimate the frame error rate (FER) in the low E_b/N_0 region by using the observed BER to model the channel variations. In addition, a lower bound on the FER of the system is also proposed based on absorbing sets. This lower bound can act as an estimate of the FER in the high E_b/N_0 region if the absorbing set used is dominant and its multiplicity is known. The quantization scheme also has an important impact on the FER and BER performances. Randomly constructed and

array-based LDPC codes are used to support the performance analyses. For all these three aspects, software-based simulations and calculations are carried out to obtain related numerical results, which verify our proposed methods.

Contents

List of Abbreviations

1G	First Generation
2G	Second Generation
3G	Third Generation
4G	Fourth Generation
5G	Fifth Generation
AWGN	Additive White Gaussian Noise
BEC	Binary Erasure Channel
BER	Bit Error Rate
BP	Belief Propagation
BS	Base Station
CFO	Carrier Frequency Offset
CN	Check Node
CP	Cyclic Prefix
CP-OFDM	Cyclic Prefix based Orthogonal Frequency Division Multiplexing
CR	Cognitive Radio
CRLB	Cramér-Rao Lower Bound
CS	Cyclic Suffix
CSI	Channel State Information
DFT	Discrete Fourier Transform
DPC	Dirty Paper Coding
DVB-S2	Digital Video Broadcasting - Satellite - Second Generation
eMBB	enhanced Mobile Broadband
f-OFDM	Filtered Orthogonal Frequency Division Multiplexing
FBMC	Filter Bank Multi-Carrier
FDD	Frequency-Division Duplex
FER	Frame Error Rate
FFT	Fast Fourier Transform
FMT	Filtered Multi-Tone
FSC	Frequency-Selective Channel

FSK	Frequency-Shift Keying
GFDM	Generalized Frequency Division Multiplexing
IAI	Inter-Antenna Interference
ICI	Inter-Carrier Interference
IDFT	Inverse Discrete Fourier Transform
IFFT	Inverse Fast Fourier Transform
i.i.d.	independent and identically distributed
IoT	Internet of Things
ISI	Inter-Symbol Interference
LDPC	Low-Density Parity-Check
LDPC-BC	Low-Density Parity-Check Block Codes
LDPC-CC	Low-Density Parity-Check Convolutional Codes
LLR	Logarithmic Likelihood Ratio
log-SPA	logarithmic Sum-Product Algorithm
LS	Least Squares
LTE	Long Term Evolution
LTE-A	Long Term Evolution Advanced
MAP	Maximum-A-Posteriori
MCM	Multi-Carrier Modulation
MF	Matched Filter
MGF	Moment-Generating Function
MIMO	Multiple-Input Multiple-Output
ML	Maximum-Likelihood
MMSE	Minimum Mean Square Error
mMTC	massive Machine Type Communications
mmWave	millimeter Wave
MRT	Maximum Ratio Transmission
MSA	Min-Sum Algorithm
MSE	Mean Square Error
MTC	Machine Type Communications
MU-MIMO	Multi-User Multiple-Input Multiple-Output
MVU	Minimum Variance Unbiased
NEF	Noise Enhancement Factor
OFDM	Orthogonal Frequency Division Multiplexing
OOB	Out of Band
OQAM	Offset Quadrature Amplitude Modulation
PDF	Probability Density Function
PDP	Power Delay Profile

PEG	Progressive Edge Growth
PE-MMSE	Polynomial Expansion-based Minimum Mean Square Error
PEP	Pairwise Error Probability
PEP	Pairwise Error Probability
Ph.D.	Doctor of Philosophy
PMF	Probability Mass Function
PSD	Power Spectral Density
PSK	Phase-Shift Keying
QAM	Quadrature Amplitude Modulation
QC-LDPC	Quasi-Cyclic Low-Density Parity-Check
QPSK	Quadrature Phase-Shift Keying
RC	Raised Cosine
RRC	Root Raised Cosine
RZF	Regularized Zero-Forcing
SC-FDE	Single-Carrier Frequency Domain Equalization
SC-FDM	Single-Carrier Frequency Division Multiplexing
SC-LDPC	Spatially Coupled Low-Density Parity-Check
SC-LDPC-CC	Spatially Coupled Low-Density Parity-Check Convolutional Codes
SER	Symbol Error Rate
SIC	Successive Interference Cancellation
SINR	Signal-to-Interference plus Noise Ratio
SISO	Single-Input Single-Output
SNR	Signal-to-Noise Ratio
SPA	Sum-Product Algorithm
STO	Symbol Time Offset
SU-MIMO	Single-User Multiple-Input Multiple-Output
TDD	Time-Division Duplex
TDL	Tapped Delay Line
TPNR	Transmit Power-to-Noise Ratio
TV	Television
TVC	Time-Variant Channel
TVWS	Television White Space
UE	User Equipment
UFMC	Universal Filtered Multi-Carrier
UHF	Ultra High Frequency
URLLC	Ultra Reliable Low Latency Communications
VN	Variable Node
VP	Vector Perturbation

WiMAX	Worldwide Interoperability for Microwave Access
WPE-MMSE	Weighted Polynomial Expansion-based Minimum Mean Square Error
ZF	Zero-Forcing

List of Symbols

A	Transmitter matrix
$\mathbb{A}$	Absorbing set or trapping set
a	Cardinality of $\mathbb{A}$
B	Number of information bits
B	Receiver matrix
$\mathbf{B}_{\mathrm{MF}}$	Receiver matrix under MF criteria
$\mathbf{B}_{\mathrm{MMSE}}$	Receiver matrix under MMSE criteria
$\mathbf{B}_{\mathrm{ZF}}$	Receiver matrix under ZF criteria
$\mathbb{B}$	Allocated frequency band
b	Cardinality of $\mathbb{O}(\mathbb{A})$
b	Information vector
$\hat{\mathbf{b}}$	Recovered information vector
C	Length of a codeword
$\mathbb{C}(\mathbb{A})$	Union of $\mathbb{E}(\mathbb{A})$ and $\mathbb{O}(\mathbb{A})$
$\mathbf{C}_{\mathrm{CRLB}}$	CRLB on a covariance matrix
$\mathbf{C}_{\mathrm{h}}$	Channel covariance matrix
$\mathbf{C}_{\mathrm{n}}$	Noise covariance matrix
$\mathbb{C}$	Check nodes in a Tanner graph
d_{c}	Maximum degreee of CNs
$d_{k,m}$	Symbol transmitted on the kth subcarrier and in the mth time slot in GFDM
$d_t^{k,m}$	Symbol transmitted on the kth subcarrier and in the mth subsymbol of the GFDM block at the tth transmit antenna
d_{v}	Maximum degreee of VNs
d	Symbol vector
$\hat{\mathbf{d}}$	Recovered symbols
$\mathbf{d}_{\mathrm{d}}$	User data
$\mathbf{d}_k$	Symbol vector on the kth subcarrier in GFDM
$\mathbf{d}_m$	Symbol vector in the mth time slot in GFDM
$\mathbf{d}_{\mathrm{p}}$	Pilots

$\mathbf{d}_t$	Symbol vector at the tth transmit antenna
$\mathbb{E}(\mathbb{A})$	Set of the CNs that are connected to the VNs in $\mathbb{A}$ with even degrees
E_b	Average energy per information bit
E_s	Average energy per symbol
$\mathbf{E}_l$	Estimation error matrix
$\mathbb{E}$	Set of edges
$\mathbf{F}_M$	$M \times M$ discrete Fourier transform matrix
FER	Frame error rate
$\mathbf{G}_l$	Matrix with Gaussian distributed entries
$G_{\text{Xia}}[f]$	The 1st order Xia pulse
$G_{\text{Xia4}}[f]$	The 4th order Xia pulse
$g[n]$	Prototype filter
$g_{\text{Gauss}}[n]$	Gaussian pulse
$g_{k,m}[n]$	Time and frequency shifted filter
$\mathbf{g}_{k,m}$	Vector containing filter samples
$\mathbf{H}$	General channel matrix (circular convolution matrix in the case of GFDM)
$\check{\mathbf{H}}$	Equivalent channel matrix for MIMO-GFDM systems
$\hat{\mathbf{H}}$	Estimate of a channel
$\tilde{\mathbf{H}}$	Channel matrix for GFDM systems
$\mathbf{H}_{Kl}$	Channel matrix with the Kronecker model of the lth channel path
$\hat{\mathbf{H}}_{\text{LS}}$	LS channel estimate
$\hat{\mathbf{H}}_{\text{MMSE}}$	MMSE channel estimate for MU-MIMO
$\mathbf{H}_{\text{PC}}$	Parity-check matrix
$\mathbf{H}_{r,t}$	Channel matrix between transmit antenna t and receive antenna r
$h_{i,j}$	Transmission coefficient from transmit antenna j to receive antenna i
$\check{\mathbf{h}}_i$	i^{th} row of $\check{\mathbf{H}}$
$\mathbf{h}_{t,r}$	Channel impulse response between transmit antenna t and receive antenna r
$\hat{\mathbf{h}}_{\text{MMSE}}$	Channel estimates under MMSE
$\hat{\mathbf{h}}_{\text{PE}-\text{MMSE}}$	Channel estimates under PE-MMSE
$\hat{\mathbf{h}}_{\text{WPE}-\text{MMSE}}$	Channel estimates under WPE-MMSE
$\mathbf{I}$	Identity matrix
J	Size of the constellaion
K	Number of subcarriers in GFDM
L	LLR
L_{ch}	Number of channel taps
L_j	j^{th} LLR
L_j^{total}	Total LLR
$L_{i \to j}$	Outgoing CN message

$L_{j \to i}$	Outgoing VN message
L_{SC}	Length of an SC-LDPC chain
M	Number of subsymbols in GFDM
M_{UC}	Length of uncoupled LDPC codes
$\mathcal{M}_q(s)$	MGF
$\mathbf{m}$	Measurements
MSE	Mean square error
MSE_{CRLB}	Mean square error corresponding to the CRLB
MSE_{MMSE}	Mean square error of MMSE estimators
$MSE_{\mathrm{PE-MMSE}}$	Mean square error of PE-MMSE estimators
$MSE_{\mathrm{WPE-MMSE}}$	Mean square error of WPE-MMSE estimators
N	Total number of symbols or the number of absorbing sets
$\mathfrak{N}$	Number of rows of a square permutation matrix
N_0	Noise power density
N_{b}	Number of the bits per symbol vector
N_{ch}	Length of the channel impulse response
N_{CP}	Length of the CP
N_{CS}	Length of the CS
N_{e}	Number of erroneous bits in an incorrect detection of a symbol vector
N_{p}	Number of pilot samples
N_{r}	Number of receive antennas
$N_{\mathrm{r}}^{\mathrm{DL}}$	Number of receive antennas in the downlink
$N_{\mathrm{r}}^{\mathrm{UL}}$	Number of receive antennas in the uplink
N_{t}	Number of transmit antennas
$N_{\mathrm{t}}^{\mathrm{DL}}$	Number of transmit antennas in the downlink
$N_{\mathrm{t}}^{\mathrm{UL}}$	Number of transmit antennas in the uplink
N_{u}	Number of single-antenna users
N_{Wd}	Pinching length for the data block
N_{Wp}	Pinching length for the preamble
$\mathbf{n}$	Additive noise (equivalent noise in the case of GFDM)
$\tilde{\mathbf{n}}$	Additive noise for GFDM systems
$\mathbf{n}_{\mathrm{eq}}$	Equivalent noise
O	OOB radiation
$\mathbb{O}(\mathbb{A})$	Set of the CNs that are connected to the VNs in $\mathbb{A}$ with odd degrees
$\mathbb{OOB}$	Frequency range outside the allocated frequency band
$\mathbf{P}$	Permutation matrix
$P(\mathbf{d} \to \hat{\mathbf{d}})$	PEP
$P(f)$	Power spectral density of the baseband signal

P_{obs}	Observed BER
P_{UB}	Union bound on the BER
p^*	Probability of error at σ^*
p_0	Probability of error based on the LLR from channels
$p_{\text{AWGN}}(e)$	SER of GFDM systems over AWGN channels
$p_{\text{FSC}}(e)$	SER of GFDM systems over FSC channels
$p_{\text{TVC}}(e)$	SER of GFDM systems over TVC channels
q_{max}	Maximum quantization level
q_{min}	Minimum quantization level
R	Achievable rate
R_r	Achievable rate at the user terminal r
$\mathbf{R}$	Received training signal
$\mathbf{R}_{\text{r}l}$	Receive correlation matrix of the lth channel path
$\mathbf{R}_{\text{t}l}$	Transmit correlation matrix of the lth channel path
$\mathbf{R}_w^2$	Covariance of the noise
r	Coding rate
$\mathbf{s}$	Quantized channel LLR vector corresponding to the VNs in $\mathbb{A}$
$\mathbf{s}_{\text{d}}$	Downlink source signal
$\mathbf{s}_n$	Downlink source signal for user terminal n
$SINR_r$	Signal-to-interference-plus-noise ratio at the user terminal r
T	Number of decoding iterations
T_{s}	Symbol duration
$\mathbf{T}$	Training sequences
$\mathbf{t}_r$	Training sequence of the rth user
$TPNR$	Transmit power-to-noise ratio
$\mathbf{U}$	LLRs input to CNs in $\mathbb{C}(\mathbb{A})$ from VNs outside $\mathbb{A}$
$\mathbf{u}$	Parameters of a channel model
$\hat{\mathbf{u}}$	Estimates of parameters
V	Polynomial degree
$\mathbb{V}$	Variable nodes in a Tanner graph
$\mathbf{v}$	Codeword vector
$\hat{\mathbf{v}}$	Estimated codeword vector
W	Set of all possible realizations of $\mathbf{U}$
$\mathbf{W}$	Precoding matrix
$\mathbf{W}_k$	A realization of $\mathbf{U}$
$\mathbf{W}_{\text{linc}}$	Special case of $\mathbf{W}_k$ with entries increasing linearly
$\mathbf{W}_{\text{MMSE}}$	MMSE precoding matrix
$\mathbf{W}_{\text{PE-MMSE}}$	PE-MMSE precoding matrix

$\mathbf{W}_{\text{sat}}$	Special case of $\mathbf{W}_k$ with all entries having saturated values
$\mathbf{w}$	Weight vector in the WPE-MMSE estimation
$\mathbf{w}_{\text{opt}}$	Optimal weights
$x[n]$	Transmit signal
$x_t[n]$	Transmit signal at the tth transmit antenna
$\mathbf{x}$	Vector form of transmit signals
$\tilde{\mathbf{x}}$	Transmit signal with CP
$\mathbf{x}_{\text{MF}}$	Transmit signal with MF precoding
$\mathbf{x}_{\text{MMSE}}$	Transmit signal with MMSE precoding
$\mathbf{x}_{\text{p}}$	Transmit signal at pilot subcarriers
$\mathbf{x}_t$	Vector form of transmit signals at the tth transmit antenna
$\mathbf{x}_{\text{ZF}}$	Transmit signal with ZF precoding
$\mathbf{y}$	General received signal (received signal after CP removal in the case of GFDM)
$\tilde{\mathbf{y}}$	Received signal of a GFDM system
$\mathbf{y}_r$	Received signal at the rth receive antenna
$\mathbf{y}_r^{\text{f}}$	Received signal in the frequency domain
$\mathbf{y}_{\text{p}_r}{}^{\text{f}}$	Received pilot signal at receive antenna r
$\mathbf{y}_{\text{s}}$	Received signal after synchronization
$\mathbf{Z}$	Positive-definite Hermitian matrix
$\mathbf{z}$	Received signal after equalization
α	Scaling parameter in polynomial expansion
β	Total number of the bits of a quantizer
β_1	Number of the bits for representing the integer part of a fixed-point number
β_2	Number of the bits for representing the fractional part of a fixed-point number
Δk	Pilot subcarrier spacing
Δ_{q}	Step size of a quantizer
δ_{ij}	Kronecker delta
ε	Transmit power
$\varepsilon(\mathbb{A})$	Event of incorrectly decoding $\mathbb{A}$ based on the full code graph
$\varepsilon(\mathbb{V})$	Event of incorrectly decoding $\mathbb{V}$ based on the full code graph
ζ	Channel parameter
ζ^*	Decoding threshold
θ	Cardinality of $\mathbb{C}(\mathbb{A})$
ϑ_r	SNR associated with the rth user
ι	Variance of the Gaussian pulse in time domain
$\lambda(\mathbb{A})$	Lower bound on the error probability of the absorbing set
λ_i	Fraction of edges corresponding to the VNs with degree i
μ	Number of bits per QAM symbol

ξ	Power normalization factor
$\xi(\mathbb{A})$	Event of incorrectly decoding $\mathbb{A}$ based on the graph of the absorbing set
ρ_i	Fraction of edges corresponding to the CNs with degree i
σ^2	Noise variance
σ^*	Decoding threshold for AWGN channels
$\tilde{\sigma}^*$	Equivalent decoding threshold for GFDM systems over AWGN channels
$\tilde{\sigma}_j^2$	Equivalent noise variance for GFDM systems
σ_r	Parameter of a Rayleigh distribution
τ	Length of a training sequence
χ	Noise enhancement factor
ω	Roll-off factor

List of Tables

List of Figures

To my family

Acknowledgments

First of all, I would like to express my sincere gratitude to my respected supervisor, Professor Paul Fortier, for his devotion to my doctoral study and research. His profound expertise led me to the world of wireless communications. His patient guidance not only taught me how to do doctoral research but also improved my ability to write high-quality technical articles. He helped to verify or improve my research methods and results, and to revise the technical papers that I wrote. Apart from providing essential research resources, he recommended to me many local and international conferences, so that I could exchange ideas with other professionals and broaden my horizons. Moreover, his encouragement kept me always confident in my project. I appreciate all he has done for me, without which I could not finish this thesis.

I thank the members of the doctoral supervisory committee for their time in evaluating my report for the pre-doctoral exam and my research progress. They provided me with insightful comments and recommendations, therefore, improving or accelerating my research. I should also thank the jury members, who are responsible for this thesis, for their time in reading and evaluating the thesis.

In addition, I thank Laval University and the China Scholarship Council for granting me the 48-month *Laval University/China Scholarship Council Joint Scholarship* to support my doctoral study and research. I would also like to thank Professor Paul Fortier for offering me a scholarship to support my research after the aforementioned joint shcolarship ended. These scholarships allowed me to focus on my Ph.D. program and to have no worries about the financial issues, which was quite important for me.

I also want to extend my thanks to the colleagues in the Radiocommunications and Signal Processing Laboratory at Laval University. They all made the laboratory a friendly and plesant workplace. Particular thanks go to Professor Jean-Yves Chouinard for his wonderful lectures and insightful discussions. He also provided me with useful materials on the topic of error-correcting codes. I also thank Professor Leslie Rusch for her outstanding lectures. Sincere thanks go to Seyedeh Samira Moosavi and Marwa Chouk for their support, encouragement and friendship. I thank the administrative staff and technicians in the Department of Electrical and Computer Engineering at Laval University. They provided me with a convenient and friendly study and research environment.

Moreover, heartfelt thanks should go to all my friends in Quebec City, Canada. They showed great enthusiasm and friendliness and helped me a lot in my daily life. I will cherish the memory of the

happy days that I spent with them.

Finally and importantly, my gratitude goes to my parents for their endless love and encouragement. They have been teaching me the philosophy of life and meaningful social values, making me a responsible man. I will be always grateful to them.

Foreword

This thesis is written on a basis of technical articles. Chapers 2, 3 and 4, respectively, contain the materials of three journal papers that I wrote during my Ph.D. study. For each paper-based chapter, a French abstract, i.e. the section *Résumé*, is added at its beginning in order to facilitate the reading of French-speaking audiences. In addition, some symbols in the original papers are adjusted in this thesis to form consistent representations of the used variables. The authors' contributions to these papers and the information about where the papers are used in this thesis are elaborated below.

Chaper 2 is based on the following paper: Yanpeng Wang and Paul Fortier, "Union Bound on the Bit Error Rate for MIMO-GFDM Systems," submitted to *Wireless Personal Communications*, Springer Science+Business Media, on April 22, 2020, under review. In this paper, a union bound on the BER is derived for MIMO-GFDM systems based on exact PEP caculations. The spatial correlation between antennas and the channel estimation errors are investigated for realistic multipath MIMO channel environments. Dr. Paul Fortier and I jointly conceived the basic idea of this work. I developed the methodology and conducted related simulations and numerical calculations. Dr. Paul Fortier provided critical guidance and comments on this work. The manuscript was written by me and revised by Dr. Paul Fortier.

Chaper 3 is based on the following paper: Yanpeng Wang and Paul Fortier, "Polynomial Expansion-Based MMSE Channel Estimation and Precoding for Massive MIMO-GFDM Systems," submitted to *Wireless Personal Communications*, Springer Science+Business Media, on June 10, 2020, under review. In this paper, we propose low-complexity channel estimators and precoders for massive MIMO-GFDM systems. Polynomial expansion is used to approximate the matrix inverses in the conventional MMSE estimation and precoding, consequently reducing the cubic computational complexity to a square order. In addition, performance limits in terms of the MSE are derived for the proposed estimators. These performance limits can provide a useful tool in predicting the estimators' performance in the high E_s/N_0 region. The fundamental idea of this work was mainly conceived by me with the guidance of Dr. Paul Fortier. I developed the methodology, conducted related simulations and calculations, and wrote the manucsript. Dr. Paul Fortier provided important comments and suggestions on the methodology and numerical results, and revised the manuscript. It is worth noting that part of the above paper about low-complexity channel estimators was presented in a conference paper: Yanpeng Wang and Paul Fortier, "Polynomial Expansion-Based MMSE Channel Estimation for Massive MIMO-GFDM

Systems," *2020 IEEE 92nd Vehicular Technology Conference (VTC2020-Fall)*, Victoria, BC, Canada, November-December 2020.

Chaper 4 is based on the following paper: Yanpeng Wang and Paul Fortier, "Performance Analysis of LDPC Coded GFDM Systems," submitted to *IEEE Transactions on Vehicular Technology*, IEEE, on February 8, 2021, under review. In this paper, we analyze the error probability performance of LDPC coded GFDM systems. We first derive the initial LLR expressions for the GFDM system in question and then estimate the FER in the low E_b/N_0 region based on the decoding threshold and the observed BER. In addition, based on absorbing sets, a lower bound on the FER is proposed for quantized SPA decoders, which can act as an estimate of the FER in the high E_b/N_0 region. The fundamental idea of this work was conceived by me with the guidance of Dr. Paul Fortier. Again, I developed the methodology, carried out related simulations and calculations, and wrote the manuscript. Dr. Paul Fortier provided critical guidance and comments on this work and revised the manuscript.

Introduction

Background

Mobile wireless communications advanced rapidly over the past decades. The first generation (1G) of mobile wireless communication systems supported basic voice services with analogue design, which improved the way people communicate. The second generation (2G) became digital, in which voice services with greater capacity and better quality, and short message service could be provided. The third generation (3G) introduced the Internet access ability on the basis of voice service and short message service. The access to the Internet was a new milestone for wireless communications, which, in many ways, enriched people's lives. The fourth generation (4G) provided higher throughput than the third generation due to the rapid development of electronics. The fifth generation (5G) is currently being deployed in many countries and areas of the world, which supports diverse application scenarios, such as enhanced mobile broadband (eMBB), ultra reliable low latency communications (URLLC), and massive machine type communications (mMTC), etc. Future wireless communication systems will face new and challenging requirements. Higher data rates will be expected as always. Greater connection density should be provided to support the massive connectivity of Internet of Things (IoT). Lower latency and higher reliability are the key factors enabling some critical control processes such as telemedicine and autonomous vehicles. Technologies with ultra-low energy consumption need to be investigated to extend the battery life cycles of the devices. In addition, higher spectral efficiency and new frequency bands, such as millimeter wave (mmWave), should be exploited to increase the data rate and bandwidth.

Waveform technologies in the physical layer are critical in the whole communication chain. Orthogonal frequency division multiplexing (OFDM) is an important multi-carrier modulation scheme which has been widely adopted in wireless communication systems, such as Long Term Evolution (LTE) and Long Term Evolution Advanced (LTE-A), due to its advantages. OFDM is robust in multi-path channels and can be easily applied in multiple-input multiple-output (MIMO) channels. In OFDM, the transmit signal can be generated by an inverse fast Fourier transform (IFFT) operation at the transmitter and the transmitted data symbols can be separated by a fast Fourier transform (FFT) operation at the receiver. However, the inherent high peack-to-average power ratio (PAPR) in OFDM can lead to high levels of out-of-band (OOB) radiation, which might be a serious problem for some scenarios such as dynamic spectrum access because of its rectangular pulse shape. In cyclic prefix (CP) based

1

OFDM (CP-OFDM), one symbol is accompanied with a CP, which leads to lower spectral efficiency. Therefore, OFDM is no longer suitable for many beyond 5G application scenarios. At present, several promising alternative waveform candidates are investigated widely, such as generalized frequency division multiplexing (GFDM) [1], universal filtered multi-carrier (UFMC) [2], filter bank multi-carrier (FBMC) [3], and filtered orthogonal frequency division multiplexing (f-OFDM) [4].

The UFMC waveform was originally proposed to overcome the problem of inter-carrier interference in OFDM. UFMC is the outcome of applying post-filtering to OFDM waveforms. A pulse shaping filter with smooth edges is applied to a group of sub-carriers to reduce the OOB radiation and as a result, the inter-carrier interference (ICI) can be effectively suppressed. UFMC is suitable for short burst communication scenarios because its filter length is shorter than the CP length of OFDM. Well designed UFMC scheme can get rid of CP so that higher spectral efficiency can be achieved [2]. UFMC is compatible with common-used techniques that are currently used in OFDM, such as MIMO transmissions. However, UFMC is sensitive to time misalignment if there is no CP. Therefore, it may not be applicable to scenarios in which loose time synchronization exists.

In FBMC, the filtering operation is applied to every sub-carrier. A set of parallel symbols are processed by a bank of modulated filters which can be well designed to offer very low frequency leakage. There are two categories of FBMC. One of them is called filtered multi-tone (FMT) which is based on a complex value scheme, such as quadrature amplitude modulation (QAM). The other one is called FBMC/OQAM and is based on the real value offset QAM (OQAM) scheme. In order to obtain orthogonality among sub-carriers, FMT has to reduce the frequency domain overlapping, which leads to low spectral efficiency. Nevertheless, FBMC/OQAM imposes the orthogonality in the real domain to get maximum frequency efficiency. FBMC is not suitable for low latency application scenarios because it can get high spectral efficiency only when a large number of symbols are transmitted.

f-OFDM is based on the regular OFDM numerology (i.e. the configurations of subcarrier spacing, CP and FFT size) but the difference is that it provides more flexibility in the parameterization. For example, different widths of the sub-bands, different filters and CP lengths can be applied to different sub-bands. As a consequence, f-OFDM can offer lower OOB emission and more flexible usage of frequency resources than OFDM.

GFDM, the focus of this thesis, is a flexible block-processing based modulation scheme that can generate flexibly configurable waveforms. Every block consists of K subcarriers with M subsymbols each, leading to KM symbols in total, where K and M can be adjusted according to the system requirements. With its high flexibility, GFDM is a unified scheme which can be also configured to be OFDM, single-carrier frequency domain equalization (SC-FDE) or single-carrier frequency division multiplexing (SC-FDM) to serve different use cases. In the GFDM block, each symbol is processed by a certain filter that is a shifted version of a prototype filter in time and frequency domains. The level of the OOB radiation can be reduced due to this filtering operation, which is important for dynamic spectrum allocation and fragmented spectrum scenarios, e.g. cognitive radio (CR) systems. Unlike

OFDM, the orthogonality among subcarriers in GFDM is altered, which consequently might result in larger ICI and inter-symbol interference (ISI). In this case, corresponding interference cancellation methods should be designed at the receiving end. While offering new features, GFDM preserves most benefits of OFDM at the price of higher complexity. GFDM can be suitable for low latency scenarios because of its flexible block structure design.

MIMO technology can increase data throughput and strengthen the robustness and reliability of wireless systems. A common configuration for MIMO in LTE mobile networks is a 2×2 mode, which places 2 antennas at the transmit end and 2 others at the receive end. Other configurations are 4×2, 4×4, 8×2, etc. In recent years, massive MIMO (also called large-scale MIMO) architectures are drawing more research attention and becoming a promising technology for the next generation of wireless communication systems. In massive MIMO, the base stations (BSs) are equipped with a large number of antennas, generally more than 100. Massive MIMO provides various advantages, such as increasing the capacity 10 times or more, improving the radiation energy efficiency in the order of 100 times and simplifying the multi-access layer due to channel hardening. The size of antennas can get smaller when the carrier frequency goes higher with the assumption that the size of antenna is proportional to the wavelength. Therefore, in mmWave bands, more antennas can be easily installed onto a given area with smaller size. Massive MIMO combined with small cells will be an important architecture for obtaining massive connectivity and seamless coverage. Massive MIMO can be equipped with inexpensive and low-power components. Massive MIMO increases the robustness both to unintended man-made interference and to intentional jamming. At the same time, massive MIMO brings several problems to be solved, including fast and distributed coherent signal processing, hardware impairments, internal power consumption, channel modeling, accurate acquisition of spatial correlation, holographic massive MIMO, application to cell-free networks, application to sub-THz communications, amalgamation with machine learning, etc. [5], [6], [7].

Low-density parity-check (LDPC) codes are capacity-approaching linear block error correction codes, which were initially discovered by Gallager in 1962 [8]. Due to their high computation complexity and the level of electronic systems at that time, LDPC codes did not get much research attention. However, with the development of electronics, LDPC codes were reinvented by D. J. C. Mackay and R. M. Neal in 1996 [9]. Near-Shannon limit performance with belief propagation (BP) method was achieved. In general, LDPC codes have better performance than Turbo codes if the block length is large. In addition, great flexibility, simple description, high throughput and low decoding complexity are also the advantages of LDPC codes. LDPC decoding can also provide low latency and more parallelization. LDPC codes have been adopted into several standards, including worldwide interoperability for microwave access (WiMAX), digital video broadcasting (DVB-S2), and the eMBB scenario in 5G. It is worth conducting further research on LDPC codes to achieve better performance.

Motivations

By gathering their advantages, the combination of GFDM, massive MIMO and LDPC codes should have the potential to provide a sophisticated and efficient wireless system. Applying MIMO technology to GFDM systems can further improve the system performance by increasing data throughput and system reliability. The error probability performance is one of the key criteria in evaluating wireless systems. Monte-Carlo simulations are often used to obtain the error probability, but, for complex systems, those simulations may take too much time to obtain reliable numerical results. Deriving analytical performance bounds is an alternative to performing Monte-Carlo simulations, which usually needs less time. Although massive MIMO technology has great potential, the increase in the number of antennas brings a problem of high computational complexity. The increase in computational complexity will consume more energy and time. This issue may be more notable at the user terminal end because complex computation will badly drain the batteries of electronic devices. As a specific example, conventional MMSE based channel estimators and precoders have cubic complexity whose computation cost is expensive as the number of antennas increases. Therefore, low-complexity solutions need to be found to keep related systems energy-efficient. The application of LDPC codes to GFDM systems can effectively improve the recovery of the transmitted information owing to their capacity-approaching performance and low decoding complexity. There are several factors that can impact the system performance, such as channel types, decoding algorithms, quantization schemes, etc. It is of great theoretical and practical importance to investigate LDPC-coded GFDM systems with these factors taken into consideration. Moreover, deriving performance bounds is quite useful because LDPC codes can have very low error probability and regular Monte-Carlo simulations will take much more time to obtain desired numerical results.

Contributions

The contributions of this thesis are as follows:

1 Develop union bounds on the error probability performance for MIMO-GFDM systems to serve as a reference for future design.

2 Propose low-complexity channel estimators for massive MIMO-GFDM systems and propose low-complexity precoders based on the channel estimates obtained from the proposed estimators.

3 Analyze the error probability performance of LDPC-coded GFDM systems. The frame error rate (FER) in the low E_b/N_0 region is efficiently estimated based on the decoding threshold and the observed bit error rate (BER). By exploiting absorbing sets, a lower bound on the FER is also proposed for LDPC coded GFDM systems when quantized SPA decoders are used.

Thesis Outline

This thesis investigates several critical issues of GFDM-based wireless systems, including performance bounds on the BER of MIMO-GFDM systems, low-complexity channel estimators and precoders for massive MIMO-GFDM systems, and error probability performances of LDPC-coded GFDM systems. To be specific, the organization of this thesis is described below.

In Chapter 1, literature reviews are provided in the areas of GFDM, MIMO/massive MIMO, and LDPC codes, respectively.

In Chapter 2, we present the first contribution of the thesis. A union bound on the BER is derived for MIMO-GFDM systems with ML detection, which is based on exact PEP calculations using MGF methods. Realistic channel environments are considered in deriving the union bound that include the spatial correlation between antennas, and channel estimation errors.

In Chapter 3, we present the second contribution of the thesis. Low-complexity MMSE channel estimators and precoders are proposed for massive MIMO-GFDM systems. In order to reduce the impact of non-orthogonality between GFDM subcarriers, we employ interference-free pilots in the channel estimation. Polynomial expansion technique is used to approximate the matrix inverses in the MMSE estimation and precoding, consequently reducing the cubic computational complexity to square order. The computational complexity of the proposed channel estimators and precoders is analyzed. In addition, performance limits in terms of MSE are also derived for the proposed estimators, which are useful tools in predicting the performance in the high E_s/N_0 region.

In Chapter 4, the third contribution of the thesis is presented. We investigate the error probability performances of LDPC-coded GFMD systems. The initial LLRs are first derived for our system model and then used in SPA decoders. We estimate the system's FER in the low E_b/N_0 region by considering the decoding threshold and observed BER. A lower performance bound on the FER is proposed based on the absorbing sets of the LDPC code when quantization is taken into account in the SPA decoding. This bound can be an accurate estimate of the FER in the high E_b/N_0 region if the absorbing set is dominant and its multiplicity is known. Both randomly constructed and array-based LDPC codes are used to verify the performance.

Finally, the thesis ends with a conclusion.

Chapter 1

Literature Review

In this chapter, we present detailed literature reviews of GFDM, MIMO, massive MIMO and LDPC codes.

1.1 Generalized Frequency Division Multiplexing

1.1.1 Basic Model of GFDM

The concept of GFDM [10] was proposed by Gerhard Fettweis et al. in 2009. It was originally designed to opportunistically exploit white spaces in the spectrum for wireless communications, such as the spectrum holes in the ultra high frequency (UHF) television (TV) bands, i.e. TV white spaces (TVWS). Therefore, the motivation therein is to develop a GFDM system which can provide low OOB radiation, simple equalization, flexible signal bandwidths and digital implementation. Because OFDM has strong spectral leakage, it will interfere with the legacy TV signals. GFDM was intended to combine the simplicity and flexibility of OFDM with effective interference reduction mechanisms.

According to [1], a typical GFDM-based communication chain can be described as in Fig. 1.1. The
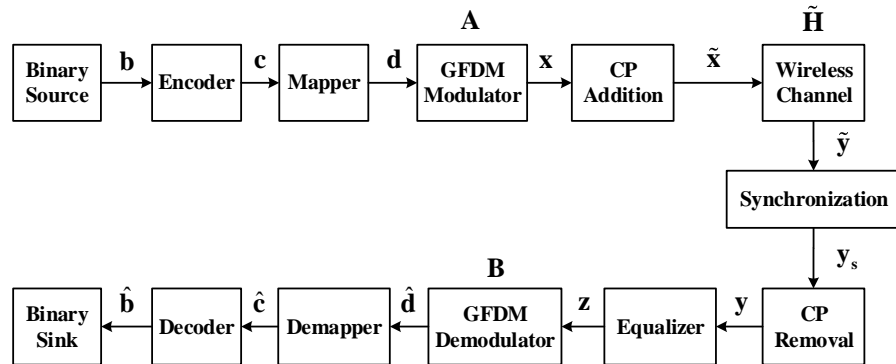

Figure 1.1: Block diagram of a typical GFDM system.

GFDM modulator is located between the mapper and CP addition. The binary information source generates the binary data vector **b** and then, **b** is encoded with an appropriate coding scheme to produce a codeword vector **c**. **c** is mapped to symbols **d** by a mapper, such as phase-shift keying (PSK), frequency-shift keying (FSK) and QAM. **d** denotes a data block that contains a total of $N = KM$ elements and can be decomposed into K sub-carriers with M sub-symbols according to $\mathbf{d} = (\mathbf{d}_0^{\mathrm{T}}, \ldots, \mathbf{d}_m^{\mathrm{T}}, \ldots, \mathbf{d}_{M-1}^{\mathrm{T}})^{\mathrm{T}}$ and $\mathbf{d}_m = (d_{0,m}, \ldots, d_{k,m}, \ldots, d_{K-1,m})^{\mathrm{T}}$. Therefore, each element $d_{k,m}$ corresponds to the data transmitted on the kth sub-carrier and in the mth sub-symbol of the GFDM block. The symbols are then modulated in the GFDM modulator unit to obtain the transmit samples $\mathbf{x} = (x[0], \ldots, x[n], \ldots, x[N-1])^{\mathrm{T}}$.

$$x[n] = \sum_{k=0}^{K-1} \sum_{m=0}^{M-1} g_{k,m}[n] d_{k,m}, \quad n = 0, \ldots, N-1, \tag{1.1}$$

where $g_{k,m}[n] = g\left[(n - mK) \bmod N\right] \exp\left(j2\pi \frac{k}{K} n\right)$ is obtained by the time and frequency shift of a prototype filter $g[n]$. $g_{k,m}[n]$ is a circularly shifted version of $g_{k,0}[n]$ because of the modulo operation. The shifting operation in frequency is performed by the complex exponential. If the filter samples are collected in a vector as $\mathbf{g}_{k,m} = (g_{k,m}[0], g_{k,m}[1], \ldots, g_{k,m}[N-1])^{\mathrm{T}}$, then we obtain the following compact form

$$\mathbf{x} = \mathbf{A}\mathbf{d}, \tag{1.2}$$

where $\mathbf{A} = (\mathbf{g}_{0,0} \quad \cdots \quad \mathbf{g}_{0,M-1} \quad \mathbf{g}_{1,0} \quad \cdots \quad \mathbf{g}_{K-1,M-1})$ denotes the $KM \times KM$ transmitter matrix. Then, a CP is added to **x** to obtain the signal $\tilde{\mathbf{x}}$ that is transmitted over a wireless channel. $\tilde{\mathbf{y}} = \tilde{\mathbf{H}}\tilde{\mathbf{x}} + \tilde{\mathbf{n}}$ is the received signal, where $\tilde{\mathbf{H}}$ is the channel matrix and $\tilde{\mathbf{n}}$ is the AWGN. $\mathbf{y}_{\mathrm{s}}$ is obtained after the received signal is synchronized. Assuming perfect synchronization ($\mathbf{y}_{\mathrm{s}} = \tilde{\mathbf{y}}$) and after the operation of CP removal, we have

$$\begin{aligned} \mathbf{y} &= \mathbf{H}\mathbf{x} + \mathbf{n} \\ &= \mathbf{H}\mathbf{A}\mathbf{d} + \mathbf{n}, \end{aligned} \tag{1.3}$$

where **H** is the corresponding circular convolution matrix with size of $N \times N$ and **n** denotes the equivalent noise. After that, a channel equalization procedure is conducted to produce **z**. When zero-forcing (ZF) equalization is assumed, $\mathbf{z} = \mathbf{H}^{-1}\mathbf{H}\mathbf{A}\mathbf{d} + \mathbf{H}^{-1}\mathbf{n} = \mathbf{A}\mathbf{d} + \bar{\mathbf{n}}$, where $\bar{\mathbf{n}} = \mathbf{H}^{-1}\mathbf{n}$. $\hat{\mathbf{d}} = \mathbf{B}\mathbf{z}$ is obtained after demodulating **z**, where **B** is the corresponding $KM \times KM$ receiver matrix. **B** is different for different receiver options: for matched filter (MF) receivers, $\mathbf{B}_{\mathrm{MF}} = \mathbf{A}^{\mathrm{H}}$; for ZF receivers, $\mathbf{B}_{\mathrm{ZF}} = \mathbf{A}^{-1}$; for linear minimum mean square error (MMSE) receivers, $\mathbf{B}_{\mathrm{MMSE}} = \left(\mathbf{R}_w^2 + \mathbf{A}^{\mathrm{H}}\mathbf{H}^{\mathrm{H}}\mathbf{H}\mathbf{A}\right)^{-1} \mathbf{A}^{\mathrm{H}}\mathbf{H}^{\mathrm{H}}$, where $\mathbf{R}_w^2$ is the covariance matrix of the noise. The ZF channel equalization is not required for the MMSE receiver due to the fact that the channel is jointly equalized in the process. In this case, $\hat{\mathbf{d}} = \mathbf{B}\mathbf{y}$. Then, $\hat{\mathbf{d}}$ is demapped to yield $\hat{\mathbf{c}}$. Finally, $\hat{\mathbf{b}}$ is obtained by decoding $\hat{\mathbf{c}}$.

GFDM features a low OOB radiation, which is defined as the ratio of the energy emitted into the range outside the allocated frequency band $\mathbb{OOB}$ to the energy contained in the allocated frequency band $\mathbb{B}$,

$$O = \frac{|\mathbb{B}|}{|\mathbb{OOB}|} \cdot \frac{\int_{f \in \mathbb{OOB}} P(f)\mathrm{d}f}{\int_{f \in \mathbb{B}} P(f)\mathrm{d}f}, \tag{1.4}$$

where $P(f)$ denotes the power spectral density (PSD) of the baseband signal. A number of guard sub-carriers can be inserted between the $\mathbb{B}$ and the $\mathbb{OOB}$. As reported in [1], the OOB radiation in GFDM is approximately 15 dB below that in OFDM by default. In order to achieve further reduction of OOB radiation, the techniques of inserting guard symbols and pinching the block boundary were discussed in [1]. An abrupt signal change between GFDM blocks leads to high OOB radiation. Guard symbols can be inserted into each GFDM block to obtain smoother transitions between blocks, consequently reducing the OOB radiation. Certainly, the insertion of guard symbols will decrease the spectral efficiency, but the related reduction can be neglected when the number of symbols is set to be large enough. The operation of pinching the block boundary means that each GFDM block at the transmitter is multiplied by a window function in the time domain to achieve smooth boundaries, which is based on the redundancy in the transmitted data introduced by the addition of the CP.

1.1.2 Symbol Error Rate Performance for Different Channels

With the assumption of a ZF receiver, the symbol error rate (SER) performance of GFDM has been analyzed in [1] under AWGN channels, static frequency-selective channels (FSC) and flat time-variant channels (TVC). The related channel impulse responses and delay spread of these considered channels are summarized in Table 1.1. The ZF receiver is capable of removing self-generated interference at the

Table 1.1: Channel impulse response and delay spread [1]

Channel	Impulse Response	Delay Spread
AWGN	$\mathbf{h} = (1)$	$N_{\text{ch}} = 1$
FSC	$\mathbf{h} = \left(10^{\frac{-i}{N_{\text{ch}}-1}} \right)^{\text{T}}_{i=0,\ldots,N_{\text{ch}}-1}$	$N_{\text{ch}} = N_{\text{CP}}$
TVC	$\mathbf{h} = (h), h \sim \mathcal{CN}(0,1)$	$N_{\text{ch}} = 1$

cost of introducing noise enhancement that depends on the pulse shaping filters. The signal-to-noise ratio (SNR) reduction is determined by the noise enhancement factor (NEF) $\chi = \sum_{n=0}^{MK-1} \left| [\mathbf{B}_{\text{ZF}}]_{k,n} \right|^2$ over flat channels, which is equal for every k.

AWGN channels: The SER expressions of GFDM and OFDM under AWGN [11] are only different in terms of the equivalent SNR that is adjusted by the NEF for GFDM at the receiver. Thus the SER of a GFDM system under AWGN is

$$p_{\text{AWGN}}(e) = 2\left(\frac{\kappa - 1}{\kappa} \right) \text{erfc}(\sqrt{\gamma}) + -\left(\frac{\kappa - 1}{\kappa} \right) \text{erfc}^2(\sqrt{\gamma}), \tag{1.5}$$

where

$$\gamma = \frac{3R_T}{2(2^\mu - 1)} \cdot \frac{E_s}{\chi N_0} \tag{1.6}$$

and

$$R_T = \frac{KM}{KM + N_{\text{CP}} + N_{\text{CS}}}. \tag{1.7}$$

$\kappa = \sqrt{2^\mu}$ and μ denotes the number of bits per QAM symbol. N_{CP} and N_{CS} denote the length of the CP and cyclic suffix (CS), respectively. E_s and N_0 denote the average energy per symbol and the noise power density, respectively. It is important to choose appropriate pulse shapes to reduce the performance loss caused by noise enhancement.

Frequency-Selective Channels: When a ZF receiver is used, the input signal of the demapper in Fig. 1.1 is $\hat{\mathbf{d}} = \mathbf{d} + \mathbf{n}_{\text{eq}}$, where $\mathbf{n}_{\text{eq}}$ is the equivalent noise. The variance of the equivalent noise for the lth sub-carrier can be given by $\sigma_l^2 = \chi_l \sigma^2$, where σ^2 denotes the variance of the AWGN and χ_l denotes the corresponding NEF. This variance is equal for every m. Therefore, the SER of a GFDM system over FSC is

$$p_{\text{FSC}}(e) = 2\left(\frac{\kappa-1}{\kappa K}\right) \sum_{l=0}^{K-1} \text{erfc}\left(\sqrt{\gamma_l}\right) + -\frac{1}{K}\left(\frac{\kappa-1}{\kappa}\right)^2 \sum_{l=0}^{K-1} \text{erfc}^2\left(\sqrt{\gamma_l}\right), \qquad (1.8)$$

where

$$\gamma_l = \frac{3R_T}{2(2^\mu - 1)} \cdot \frac{E_s}{\chi_l N_0}. \qquad (1.9)$$

GFDM can provide better mitigation of the frequency selectivity in each sub-carrier than OFDM because GFDM has more samples per sub-carrier.

Time-Variant Channels: A TVC can be described as a multiplicative channel whose amplitude gain is Rayleigh distributed with parameter σ_r and whose phase is uniformly distributed in $[-\pi, \pi]$. Assume that the channel is static during the transmission of one GFDM symbol. The SER of a GFDM system over TVC is

$$p_{\text{TVC}}(e) = 2\left(\frac{\kappa-1}{\kappa}\right)\left(1 - \sqrt{\frac{\gamma_r}{1+\gamma_r}}\right) + -\left(\frac{\kappa-1}{\kappa}\right)^2\left[1 - \frac{4}{\pi}\sqrt{\frac{\gamma_r}{1+\gamma_r}}\,\text{atan}\left(\frac{1+\gamma_r}{\gamma_r}\right)\right], \qquad (1.10)$$

where

$$\gamma_r = \frac{3\sigma_r^2 R_T}{2^\mu} \cdot \frac{E_s}{\chi N_0}. \qquad (1.11)$$

Closed-form SER performance of GFDM over AWGN channels has been presented in [12], which is under the assumption that an MF receiver is employed. In the low SNR region, MF receivers outperform ZF ones because of the impact of the noise enhancement. However, in the high SNR region, ZF receivers outperform MF ones because MF receivers suffer from self-interference. Simulation results of the SER performance of MMSE receivers have also been presented in [13]. The MMSE receiver can provide the best performance because it balances the noise enhancement and the self-interference.

The union bound can be used to provide a tight bound on BER or SER of communication systems [14], [15]. Therefore, it is an appropriate performance criterion for optimizing algorithms used in the related designs.

1.1.3 Impacts of Pulse Shaping Filters

The operation of pulse shaping in each sub-carrier can adjust the OOB radiation and will produce non-orthogonal waveforms. The circular pulse shaping filters in GFDM, such as root raised cosine

(RRC), raised cosine (RC), Xia pulse, Gaussian pulse and Dirichlet pulse were investigated in [12]. The Xia pulses are a family of real asymmetric pulses that can be defined in the frequency domain by a roll-off function and a roll-off factor [16]. The 1st order Xia pulse can be formulated as [1]

$$G_{\text{Xia}}[f] = \frac{1}{2}\left[1 - e^{-j\pi\lin_\omega\left(\frac{f}{M}\right)\text{sign}(f)}\right],\tag{1.12}$$

where

$$\lin_\omega(x) = \min\left(1, \max\left(0, \frac{1+\omega}{2\omega} + \frac{|x|}{\omega}\right)\right),\tag{1.13}$$

which is a truncated linear function and can describe the roll-off area systematically. ω denotes the roll-off factor. The 4th order Xia pulse can be formulated as [1]

$$G_{\text{Xia4}}[f] = \frac{1}{2}\left[1 - e^{-j\pi p_4\left(\lin_\omega\left(\frac{f}{M}\right)\right)\text{sign}(f)}\right],\tag{1.14}$$

where

$$p_4(x) = x^4\left(35 - 84x + 70x^2 - 20x^3\right).\tag{1.15}$$

The Xia pulse turns into a Dirichlet pulse when the roll-off factor decreases to 0. Another example is the Gaussian pulse that can be described in the time domain as [12]

$$g_{\text{Gauss}}[n] = \frac{\sqrt{\pi}}{\iota}\exp\left(-\frac{\pi^2 n}{\iota^2 N}\right),\tag{1.16}$$

where ι denotes its variance in the time domain.

Gaussian pulses can provide the lowest OOB radiation when 6 guard carriers are used but it has the highest interference variance which is relatively independent of ι. The interference variance of RRC filters is comparable to that of RC and Xia pulses, while RRC filters show stronger OOB radiation. RC filters can suppress the OOB radiation to 50 dB below that of OFDM with 6 guard carriers. The 1st order Xia pulse provides an equal reduction of the OOB radiation to the RC filter but its interference is stronger. The 4th order Xia pulse shows higher level of OOB radiation with lower interference variance than the RC filter. The Dirichlet pulse is free of self-interference and can provide an OOB radiation of -68 dB. In addition, Dirichlet pulses can make GFDM orthogonal and consequently provide the same BER performance as OFDM over AWGN channels with notably lower OOB radiation. The BER of GFDM systems over AWGN channels is affected by the variance of the self-interference that is caused by the pulse shaping filter. To be specific, the BER increases with the variance of the self-interference when the self-interference is larger than a critical value. This value increases with the level of the noise. Therefore, in the case of low SNR, the above-mentioned critical value is large and the constraint for low self-interference can be relaxed, which means a pulse shaping filter with high interference can be employed in order to obtain other benefits like better spectral properties. On the contrary, in the case of high SNR, the above-mentioned critical value is small and pulse shaping filters with low interference should be chosen to achieve acceptable BER performance [12].

In [17], two kinds of improved Nyquist filters from [18], namely, the flipped-hyperbolic secant (Fsech) pulse shaping filter and the flipped-inverse hyperbolic secant (Farcsech) pulse shaping filter were

introduced into GFDM. Their SER performance was evaluated over an AWGN channel with 16-QAM mapping and compared with RRC filters. The concept of wavelet was used to obtain a better time-frequency localization of the pulse shaping filters, where a Meyer auxiliary function [19] was employed. Simulation results showed that these two improved Nyquist pulse shaping filters can achieve better SER performance in GFDM compared to RRC pulse shaping filters.

1.1.4 Receiver Design and Interference Cancellation

Although GFDM provides attractive properties, the non-orthogonality of GFDM is a critical issue to tackle. This non-orthogonality between sub-carriers can lead to interference. ZF, MF and MMSE receivers have been derived to reduce the self-interference [13]. The ZF receiver can remove ICI but suffers from some BER performance loss due to the problem of noise enhancement. The MF receiver cannot completely eliminate the ICI. The MMSE receiver can reduce the noise enhancement and maximize the signal-to-interference plus noise ratio (SINR). These receivers perform large matrix inversion and multiplication operations. Therefore, their computational complexity is very high. A time domain successive interference cancellation (SIC) method was introduced to completely remove the self-interference [20]. But it was a computationally exhaustive procedure. The interference cancellation performed in the frequency domain was introduced in [21]. The sparsity of the pulse shaping filter in the frequency domain was employed to reduce the computational complexity at the receiver. This method can remove the self-interference but can result in error propagation problems. A fast algorithm based on the Gabor transform structure has been proposed in [22] to calculate the ZF and MF filters at the receiver. Gabor analysis and time-frequency analysis were proposed by Dennis Gabor in 1946 [23]. His idea was to transmit an arbitray signal as the linear combination of time-shifted and frequency-shifted Gaussian impulses. The authors of [22] showed that the transmission and linear reception in GFDM are equivalent to a critically sampled finite discrete Gabor expansion and transform, respectively. In this approach, the matrix inversion is avoided but the matrix to vector multiplication still has high computational complexity. In [24], a low-complexity modem structure was proposed. Block circulant matrices were exploited. A unified structure of the ZF, MF and MMSE receiver was also presented. This receiver structure for interference cancellation is not iterative, which makes it possible to run the computations in parallel, consequently reducing the system processing delay. At the transmitter, the sparsity of the modulation matrix was obtained to reduce the computational complexity by use of block discrete Fourier transform (DFT) and inverse discrete Fourier transform (IDFT) matrices. At the receiver, block diagonalization was used to design the low-complexity ZF, MF and MMSE demodulators.

The non-orthogonality caused by pulse shaping results in self-generated ICI. ICI, in turn, will degrade the performance of GFDM. In [20], a basic serial and a double sided serial interference cancellation approach were introduced into the GFDM system. Self-generated ICI introduced by the RRC pulse shaping can be successfully suppressed. In GFDM, if RRC filters are used at the transmitter and receiver, ICI just exists in the neighbouring sub-carriers. Fig. 1.2 illustrates the principle of how

the ICI occurs between the adjacent sub-carriers in the frequency domain. The basic idea therein
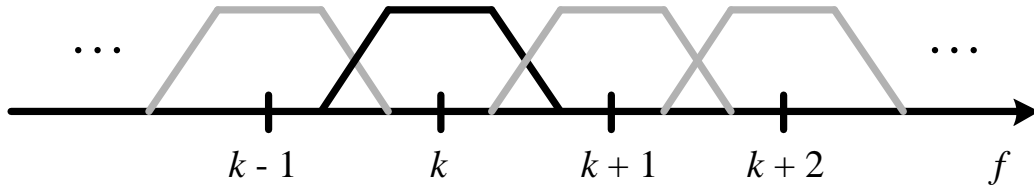

Figure 1.2: Illustration of the interference in the kth sub-carrier from adjacent sub-carriers [20].

was that the received data symbols are fed back to the interference cancellation unit and in the ith sub-iteration, the signal for interference cancellation is subtracted from the composite received signal. In the sub-iteration $i = k$, the interference from the $(k-1)^{th}$ sub-carrier will be removed and at the same time we obtain the symbols on the kth sub-carrier. Then, a similar process can be perform for all the sub-carriers. At the end of this procedure, the ICI caused by the preceding sub-carriers can be mitigated. For the cancellation of ICI from the succeeding sub-carriers, another K similar sub-iterations should be performed.

In the previous basic serial interference cancellation approach, the ICI effects from preceding and succeeding sub-carriers can be eliminated successively. However, they can also be removed simultaneously through the double sided serial interference cancellation approach. For the cancellation on the kth sub-carrier, the data symbols on the $(k-1)^{th}$ and $(k+1)^{th}$ sub-carriers are processed simultaneously to get the cancellation signal that is subtracted from the composite received signal. A similar procedure can be performed in a pattern of iteration to mitigate the ICI in other sub-carriers. It was shown that the double sided SIC outperforms the basic SIC for both quadrature phase-shift keying (QPSK) and QAM modulation and the BER performance of the GFDM system with the double sided SIC can match the theoretical BER performance of the OFDM system [20]. It is possible to carry out the interference cancellation procedure in a parallel way. All the received symbols will be detected simultaneously and be used to build the cancellation signal for every sub-carrier.

1.1.5 Synchronization in GFDM

Synchronization is significant for the signal processing at the receiver. Various synchronization techniques [25], [26] have been proposed for the OFDM scheme due to its prevalence in existing wireless systems. However, there is a deficiency of synchronization techniques for the GFDM scheme. Symbol time offset (STO) and carrier frequency offset (CFO) estimation [27] are important challenges in multicarrier receiving. The block structure of GFDM along with the CP addition allows for the fundamental synchronization solutions designed for OFDM to be employed in GFDM. Low OOB radiation design should be taken into consideration when these techniques are used in GFDM. A windowed GFDM preamble can be defined with $M = 2$ and in the kth sub-carrier, the sub-symbols

$d_{k,0}$ and $d_{k,1}$ are composed of the same pseudo-noise sequence. Pinching the block boundary can ensure low OOB radiation [1]. This structure is illustrated in Fig. 1.3. Different pinching lengths
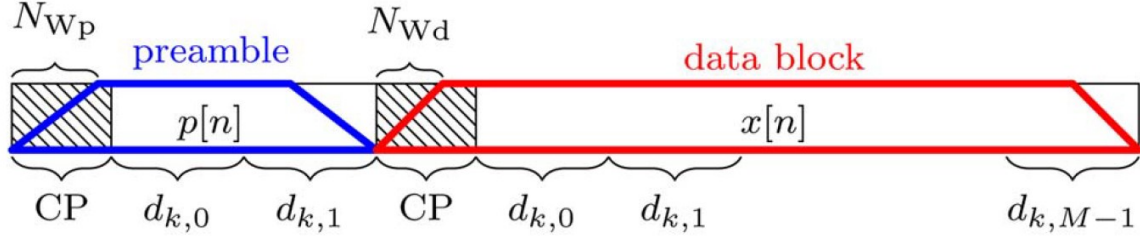

Figure 1.3: Illustration of the GFDM preamble and data block [1].

(N_{Wd} and N_{Wp}) can be chosen for the data block and preamble, respectively, for obtaining a desired emission mask. The two identical halves of the GFDM preamble that result from the use of the same pseudo-noise sequence can be identified with an autocorrelation metric. Then, the STO and CFO can be estimated to serve the synchronization. In addition, an approximate maximum-likelihood (ML) blind synchronization approach was investigated in [28] for GFDM systems by neglecting some weak self-introduced interference and approximately averaging the time-varying signal power. The effect of timing and carrier frequency offset on GFDM systems was investigated in [29]. The simulation results therein indicated that GFDM systems are more sensitive to timing offset but robust to CFO (with large frequency errors) compared with OFDM systems.

1.2 Multiple-Input Multiple-Output and Massive Multiple-Input Multiple-Output

1.2.1 Basic MIMO Model

A typical MIMO channel can be illustrated as the structure shown in Fig. 1.4. On the left are N_{t} transmit antennas and on the right are N_{r} receive antennas. Generally, there are multiple transmit antennas and multiple receive antennas. If there is only one transmit antenna and one receive antenna, then the channel model is called single-input single-output (SISO). For MIMO, if there is just one user equipment (UE) configured with multiple antennas, it is called single-user MIMO (SU-MIMO); if there are more than one UE, it is called multi-user MIMO (MU-MIMO). Let $\mathbf{x}$, $\mathbf{y}$ and $\mathbf{H}$ denote the transmitted signal, received signal and channel matrix, respectively. Then, we have the following model:

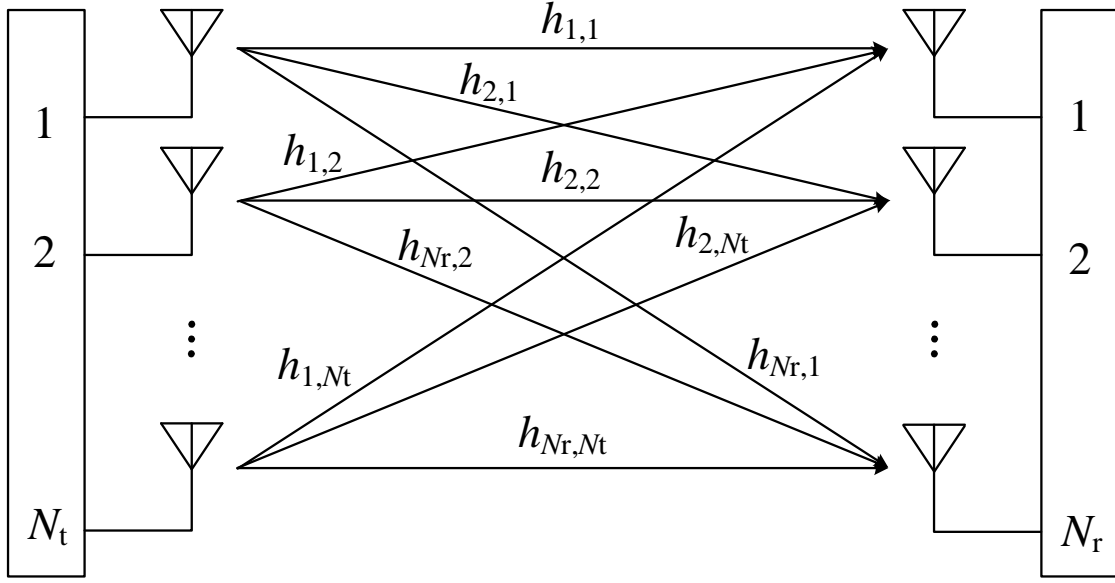$$\mathbf{y} = \mathbf{H}\mathbf{x} + \mathbf{n}, \tag{1.17}$$

Figure 1.4: Illustration of an MIMO channel.

where $\mathbf{n}$ is the additive noise, and $\mathbf{H}$ can be expressed as

$$
\mathbf{H} = \begin{bmatrix} h_{1,1} & h_{1,2} & \dots & h_{1,N_t} \\ h_{2,1} & h_{2,2} & \dots & h_{2,N_t} \\ \dots & \dots & h_{i,j} & \dots \\ h_{N_r,1} & h_{N_r,2} & \dots & h_{N_r,N_t} \end{bmatrix}, \tag{1.18}
$$

where $i = 1, 2, \dots, N_r$ and $j = 1, 2, \dots, N_t$. $h_{i,j}$, the entry of $\mathbf{H}$, denotes the transmission coefficient from the jth transmit antenna to the ith receive antenna. In practice, the channel matrix $\mathbf{H}$ needs to be estimated to obtain the estimation of the transmitted signal $\mathbf{x}$. However, for theoretical analyses, $\mathbf{H}$ can be assumed to be known at the receiver. If $\mathbf{H}$ is a deterministic and constant channel matrix of a narrow-band time-invariant channel, we have $\mathbf{y} = \sqrt{\varepsilon}\mathbf{H}\mathbf{x} + \mathbf{n}$ [30], where ε denotes the transmit power if we assume that the total power of $\mathbf{x}$ is normalized and that the noise is zero-mean circularly symmetric complex Gaussian with an identity covariance matrix $\mathbf{I}$. With independent and identically distributed (i.i.d.) Gaussian transmit signals and perfect channel state information (CSI) at the receiver, the instantaneous achievable rate is given by [30]

$$
R = \log_2 \det\left(\mathbf{I} + \frac{\varepsilon}{N_t}\mathbf{H}\mathbf{H}^{\text{H}}\right). \tag{1.19}
$$

When the entries of $\mathbf{H}$ are normalized such that $\text{Tr}(\mathbf{H}\mathbf{H}^{\text{H}}) \approx N_t N_r$, lower and upper bounds on the capacity can be formulated as [31]

$$
\log_2(1 + \varepsilon N_r) \leq R \leq \min(N_t, N_r)\log_2\left(1 + \frac{\varepsilon \max(N_t, N_r)}{N_t}\right). \tag{1.20}
$$

The singular values of $\mathbf{HH^H}$ determine the achievable rate. With the same normalization, channels whose singular values are all equal can achieve the upper bound in (1.20), and channels with only one non-zero singular value exhibit the lower bound in (1.20). When N_t goes to infinity and N_r remains constant, the achievable rate reaches the upper bound in (1.20) [30]

$$R \approx N_r \log_2\left(1 + \varepsilon\right). \tag{1.21}$$

When N_r goes to infinity and N_t remains constant, the achievable rate reaches the upper bound in (1.20) as well [30]

$$R \approx N_t \log_2\left(1 + \frac{\varepsilon N_r}{N_t}\right). \tag{1.22}$$

The expressions in (1.21) and (1.22) show that a higher capacity can be achieved when a large number of antennas are installed in the MIMO link. It should be noted that the above discussion is based on the assumption that the row or column vectors of $\mathbf{H}$ are asymptotically orthogonal.

1.2.2 Massive MIMO

Massive MIMO appears when the number of antennas increases to a higher order of magnitude than that of conventional MIMO configurations, i.e. 100 or more. The first base station (BS) architecture with a large number of antennas is Argos [32] which support 64 antennas and can serve 15 user terminals simultaneously. Information theoretical analyses of conventional MIMO and massive MIMO have been presented in [30] to demonstrate the advantages of massive MIMO. In massive MIMO, pilot contamination can be introduced by non-orthogonal pilot sequences used by different users in the neighbouring cells. Pilot contamination will affect both uplink and downlink transmission in a multi-cell massive MIMO system. Pilot contamination was initially viewed as a fundamental limitation that leads to a finite spectral efficiency limit in massive MIMO. However, the results in [33] later showed that this is generally not true and that the spectral efficiency can grow without bound in the presence of pilot contamination, despite the fact that there is a power loss and reduced estimation quality. Appropriate precoding or blind techniques might be used to mitigate the effect of pilot contamination. Precoding is a critical beamforming technique to enable multi-stream transmission in massive MIMO wireless systems. There are linear and non-linear precoding algorithms. Non-linear precoding methods include dirty-paper-coding (DPC) [34], lattice-aided methods [35] and vector perturbation (VP) [36], which may bring better performance but have higher implementation complexity at the same time. Linear precoding methods include ZF and MF and are shown to be a better choice for massive MIMO systems [31]. Energy efficiency is the ratio of spectral efficiency and transmit power. Massive MIMO can improve the system energy efficiency. But there should be tradeoff between spectral efficiency and energy efficiency. Current theoretical research on massive MIMO is based on crucial assumptions about the channels. These assumptions are still in the need of validation through practical channel measurements. Channel measurements for massive MIMO in [37] showed that most of the advantages in theoretical work are still available over the measured channels. Considering the cost at the terminal end and the difficulty in acquiring CSI for a large number of terminals, a practical deployment of

massive MIMO is to have a large number of antennas at the BS which serves a limited number of terminals with a single antenna or several antennas. The massive MU-MIMO system shown in Fig. 1.5 is a typical application form. With a large scale antenna array, massive MIMO can provide several advantages, such as higher capacity, higher energy and spectral efficiency and lower latency. Meanwhile, many problems caused by the large number of antennas must be resolved, such as channel characterization, pilot contamination, and hardware impairments.
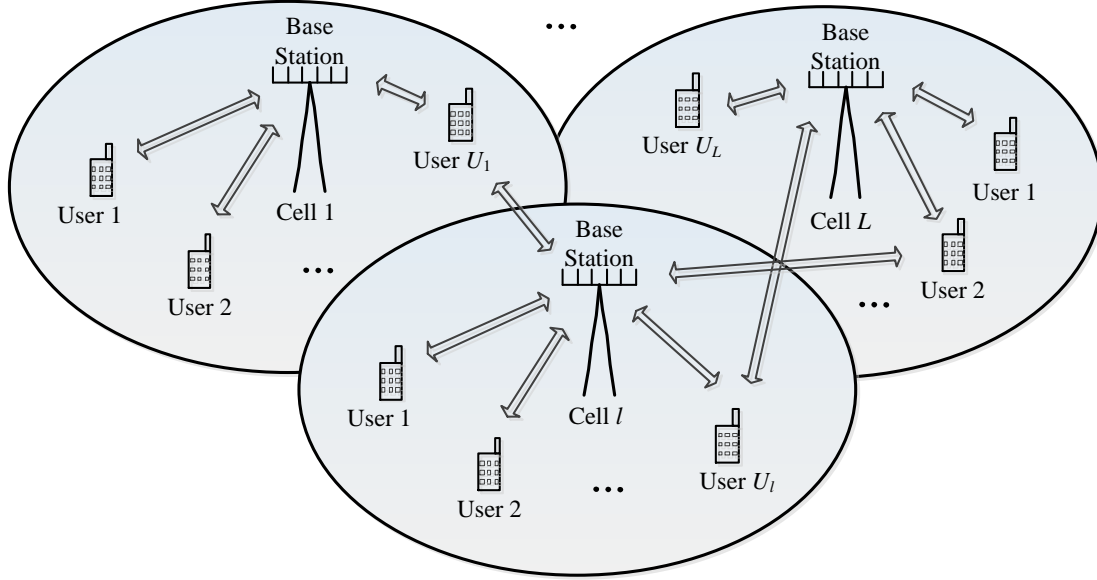
Figure 1.5: Illustration of a massive MU-MIMO system.

1.2.3 Channel Estimation

CSI is necessarily required for MIMO systems at the BS for the signal detection in the uplink and precoding in the downlink. There are two duplex modes under consideration, namely frequency-division duplex (FDD) and time-division duplex (TDD). In the FDD mode, the CSI is different for the uplink and downlink. The uplink channel estimation can be performed at the BS by the use of different pilots from all terminals. The channel estimation in the downlink is not that simple. Pilot sequences are sent by the BS to all terminals. Then the terminals estimate their downlink CSI and send those estimates back to the BS. The resource used for channel estimation is proportional to the number of the transmit antennas and independent of the receive antennas. Therefore, the time resource for the downlink CSI acquisition is proportional to the number of antennas at the BS. Because the number of antennas in massive MIMO is very large, conventional channel estimation techniques will impose a heavy burden on the system and will not be feasible any more. In TDD mode, the CSI estimation process can benefit from the channel reciprocity. The downlink channel estimation can be obtained from the results of the uplink channel estimation. Therefore, only the channel estimation in the uplink is required given the

assumption of channel reciprocity. The procedure is as follows: all the terminals send pilot sequences and the BS performs the channel estimation using the received pilots. Based on the channel reciprocity, the BS can acquire the CSI for the downlink. However, there is a problem called pilot contamination [38] if we reuse the same pilot sequences in all cells. This inter-cell interference will not disappear as the number of antennas increases. Pilot contamination degrades the transmission performance both in the uplink and in the downlink for multi-cell deployment. Therefore, it is important to take the pilot contamination into account when we develop techniques for massive MIMO systems. Several different techniques for mitigating the pilot contamination were introduced in [30].

A commonly used channel estimation approach is linear MMSE which has near-optimal performance and low complexity. With the assumption of a system model using Rayleigh block fading channels with the OFDM scheme, the linear MMSE estimation of an MU-MIMO channel in the TDD mode has been presented in [39]

$$\hat{\mathbf{H}}_{\mathrm{MMSE}} = \mathrm{diag}\left(\left(\begin{array}{ccc} \dfrac{\sqrt{\vartheta_1 \tau}}{1 + \vartheta_1 \tau} & \cdots & \dfrac{\sqrt{\vartheta_{N_{\mathrm{u}}} \tau}}{1 + \vartheta_{N_{\mathrm{u}}} \tau} \end{array} \right)^{\mathrm{T}} \right) \mathbf{T}^{\mathrm{T}} \mathbf{R}^{\mathrm{T}}, \tag{1.23}$$

where τ and ϑ_r denote the number of symbols in the training sequence and the SNR associated with the rth user, respectively. N_{u} denotes the number of single-antenna users. $\mathbf{T} = \begin{bmatrix} \mathbf{t}_1 & \mathbf{t}_2 & \cdots & \mathbf{t}_{N_{\mathrm{u}}} \end{bmatrix}$ and $\mathbf{T}^{\mathrm{H}}\mathbf{T} = \mathbf{I}$. $\sqrt{\tau}\mathbf{t}_r^{\mathrm{H}}$ is the training sequence vector transmitted by the rth user. The training sequences here are orthogonal, i.e., $\mathbf{t}_i^{\mathrm{H}}\mathbf{t}_j = \delta_{ij}$, where δ_{ij} denotes the Kronecker delta. The orthogonal sequences imply the condition $N_{\mathrm{u}} \leq \tau$. $\mathbf{H}$ is the forward channel matrix (i.e., in the downlink) and $\hat{\mathbf{H}}_{\mathrm{MMSE}}$ is the conditional mean of $\mathbf{H}$, given $\mathbf{R}$. $\mathbf{R}$ is the training signal received at the BS.

Another approach for channel estimation is least squares (LS). According to the description of LS channel estimation in [40], we have

$$\hat{\mathbf{H}}_{\mathrm{LS}} = \mathbf{R}\mathbf{T}^{\mathrm{H}}\left(\mathbf{T}\mathbf{T}^{\mathrm{H}}\right)^{-1}, \tag{1.24}$$

where $\mathbf{R}$ denotes the training sequences received at the BS and $\mathbf{T}$ contains the training sequences transmitted by the users. It is worth noting that $\hat{\mathbf{H}}_{\mathrm{LS}}$ here is an estimate of the reverse channel, i.e., in the uplink.

In addition, a compressive sensing based approach for channel estimation was proposed in [40]. As for the CSI acquisition at the terminal end, an efficient channel estimation scheme called beamforming training was presented in [41]. In this scheme, pilot sequences were precoded and sent by the BS to all terminals. Each terminal estimated the CSI with the MMSE algorithm according to the received pilot sequences. The related overhead for channel estimation is proportional to the number of the terminals and independent of the number of antennas at the BS.

The Cramér-Rao bound can provide a lower bound on the mean square error (MSE) of unbiased estimates. Therefore, we can use it as a performance criterion for evaluating different channel estimators. Let the parameters used in the channel model be collected in a vector $\mathbf{u}$ with probability density function

(PDF) $f(\mathbf{m};\mathbf{u})$, where $\mathbf{m}$ contains the measurements from which $\mathbf{u}$ can be estimated. The estimates of these parameters are denoted by $\hat{\mathbf{u}}$. Then, the Cramér-Rao bound can be given as

$$\mathrm{E}\left[(\hat{\mathbf{u}}-\mathbf{u})(\hat{\mathbf{u}}-\mathbf{u})^{\mathrm{H}}\right] \geq I(\mathbf{u})^{-1}, \tag{1.25}$$

where

$$I(\mathbf{u}) = \mathrm{E}\left[\mathrm{E}\left[\left(\frac{\partial \ln f(\mathbf{m}|\mathbf{u})}{\partial \mathbf{u}^*}\right)\left(\frac{\partial \ln f(\mathbf{m}|\mathbf{u})}{\partial \mathbf{u}^*}\right)^{\mathrm{H}}\bigg|\mathbf{u}\right]\right] + \mathrm{E}\left[\left(\frac{\partial \ln f(\mathbf{u})}{\partial \mathbf{u}^*}\right)\left(\frac{\partial \ln f(\mathbf{u})}{\partial \mathbf{u}^*}\right)^{\mathrm{H}}\right] \tag{1.26}$$

is the so-called Fisher information matrix [42] under regularity conditions.

1.2.4 Precoding

As mentioned above, linear precoding techniques, including ZF, MF and MMSE, are preferred in massive MIMO systems. In the case of MF precoding, the transmit signal from the BS can be formulated as

$$\mathbf{x}_{\mathrm{MF}} = \frac{1}{\sqrt{\xi}}\left(\mathbf{H}^{\mathrm{T}}\right)^{\mathrm{H}}\mathbf{s}_{\mathrm{d}} = \frac{1}{\sqrt{\xi}}\mathbf{H}^*\mathbf{s}_{\mathrm{d}}, \tag{1.27}$$

where ξ is the power normalization factor [43] and $\mathbf{s}_{\mathrm{d}}$ is the downlink source information vector. $\mathbf{H}$ denotes the uplink channel matrix. In TDD mode, the downlink channel matrix can be regarded as the transpose of the uplink channel matrix. In the case of ZF precoding, the transmit signal from the BS can be formulated as

$$\mathbf{x}_{\mathrm{ZF}} = \frac{1}{\sqrt{\xi}}\mathbf{H}^*\left(\mathbf{H}^{\mathrm{T}}\mathbf{H}^*\right)^{-1}\mathbf{s}_{\mathrm{d}}. \tag{1.28}$$

In the case of MMSE precoding, the transmit signal from the BS can be formulated as

$$\mathbf{x}_{\mathrm{MMSE}} = \frac{1}{\sqrt{\xi}}\mathbf{H}^*\left(\mathbf{H}^{\mathrm{T}}\mathbf{H}^* + \varphi\mathbf{I}\right)^{-1}\mathbf{s}_{\mathrm{d}}, \tag{1.29}$$

where $\varphi = N_{\mathrm{r}}/\varepsilon$ and N_{r} denotes the number of the single-antenna users.

In [44], the authors analyzed the performance of ZF precoding in a single-cell massive MIMO context, where the number of BS antennas is much larger than the number of the terminals. A lower bound for the sum rate of the ZF precoding has been derived. The ZF precoding outperforms the MF precoding in the high spectral efficiency region but the MF precoding outperforms the ZF precoding in the low spectral efficiency region.

Low-complexity precoding techniques are vital to massive MIMO systems because the computational complexity in precoding will increase with the number of antennas at the BS. A matrix-inversion-based low-complexity design has been introduced to reduce the computational complexity of the ZF and MMSE precoding [45]. A low-complexity precoding scheme based on a matrix polynomial was proposed in [46]. Simulations therein indicated that this scheme can achieve near MMSE performance in terms of the sum rate and provide better performance than the conjugate beamforming by orders of magnitude. The computational complexity of the matrix-polynomial-based precoding scheme, conjugate beamforming and MMSE have been analyzed in [46].

1.3 Low-Density Parity-Check Codes

1.3.1 Representations of LDPC Codes

LDPC codes can be defined with sparse parity-check matrices, where the term *sparse* means that most of the elements in a parity-check matrix (both in each row and column) are 0's and there are only a few 1's. There are two kinds of LDPC codes, namely, regular and irregular LDPC codes. An LDPC code can be defined as (n, j, k), where n denotes the code length, j denotes the number of 1's in each column of the parity-check matrix, and k denotes the number of 1's in each row of the parity-check matrix. If j and k are fixed for all columns and rows, then the code is called a regular LDPC code; if j and k are variable for all columns and rows, then the code is called an irregular LDPC code. In addition to the algebraic representation, LDPC codes can also be represented by Tanner graphs [47] that are essentially bipartite graphs. A typical Tanner graph representing an LDPC code is illustrated in Fig. 1.6. The nodes on the left part of Fig. 1.6 are the so-called variable nodes (VN) and the nodes on the
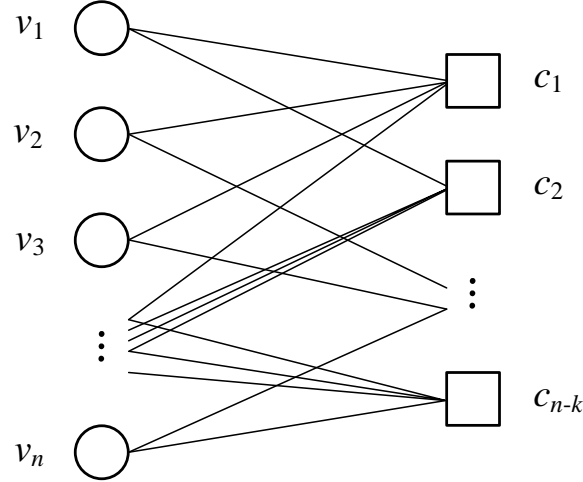
Figure 1.6: Illustration of a Tanner graph.

right part are the so-called check nodes (CN). Each VN corresponds to a column of the parity-check matrix and each CN corresponds to a row of the parity-check matrix. In a Tanner graph, for an n-bit codeword with k source bits, the number of the VNs is n and the number of the CNs is $(n - k)$. There will be an edge for each non-zero element in the parity-check matrix. The degree of a node can be defined as the number of edges incoming on it. The sparse parity-check matrix of an LDPC code is denoted as $\mathbf{H}_{PC}$. Then the degree distribution pair (λ, ρ) of $\mathbf{H}_{PC}$ can be described as follows [48]

$$\lambda(x) = \sum_{i=2}^{d_v} \lambda_i x^{i-1}, \tag{1.30}$$

$$\rho(x) = \sum_{i=2}^{d_c} \rho_i x^{i-1}, \tag{1.31}$$

where λ_i and ρ_i are the fraction of edges which corresponds to the VNs and CNs with degree i, respectively. d_v and d_c are the maximum degreee of the VNs and CNs, respectively. In fact, a given degree distribution pair determines an ensemble of matrices because distinct matrices might have the same degree distribution pair.

1.3.2 Fundamentals of LDPC Codes

As described in [49], there are two steps for the encoding of LDPC codes. The first step is to create a sparse parity-check matrix and the second step is to generate codewords based on the matrix. Although irregular LDPC codes can outperform regular ones [50], it is difficult to establish the irregular parity-check matrices. Several decoding algorithms were presented in [49], including the sum-product algorithm (SPA), logarithmic sum-product algorithm (log-SPA) and the min-sum algorithm (MSA). The logarithmic sum-product algorithm introduces logarithmic likelihood ratio (LLR) that can reduce most multiplication to addition. The MSA eliminates the need for addition in the process of message update, trading precision for speed.

The progressive edge growth (PEG) algorithm was introduced in [51] to construct Tanner graphs with a large girth. The term *girth* is the length of the shortest cycle in a graph. This algorithm established edges between symbol nodes and CNs in an edge-by-edge manner. PEG-based Tanner graphs for both regular and irregular LDPC codes were investigated. It was shown that the PEG algorithm is powerful for generating high-quality short-block-length LDPC codes. LDPC codes based on finite geometries were described in [52]. This kind of LDPC codes can provide relatively good performance in terms of minimum distances. There were no cycles of length 4 in the corresponding Tanner graphs. These codes performed well with iterative decoding in the case of high rate and long block length. The parallel LLR update in a bipartite graph and serial LLR update in a tripartite graph were investigated and compared in an LDPC coded massive MIMO system with the BP algorithm [53]. It was shown that the tripartite graph can provide faster convergence when showing the same performance with the bipartite graph. The authors of [54] proposed a generalized space shift keying scheme with codebook-assisted low-complexity detector for massive MIMO systems, in which an LDPC code is used to gain better error performance with low computational complexity.

The threshold under BP decoding scheme is close to the Shannon limit for well-designed LDPC block codes (LDPC-BCs). However, this threshold is typically strictly smaller than the threshold under maximum-a-posteriori (MAP) decoding scheme which is optimal. For proper convolutional codes, these two thresholds can coincide. This phenomenon is called *threshold saturation* [55]. LDPC convolutional codes (LDPC-CCs) are the convolutional counterparts of LDPC-BCs and can be defined by parity-check equations with a small number of non-zero taps. These codes have very large constraint lengths and the number of the taps does not depend on the constraint length. LDPC-CCs can be constructed by repeating the constraint structure of quasi-cyclic LDPC (QC-LDPC) codes to infinity

[56]. The Viterbi algorithm is typically used to decode standard convolutional codes with the fact that the complexity of the Viterbi algorithm is exponential in the constraint length. Therefore, the Viterbi algorithm is not suitable for codes with large constraint lengths. Message-passing algorithms, such as BP, are feasible for these codes due to the low-density nature of the parity-checks [57].

1.3.3 Spatially Coupled LDPC Codes

Spatially coupled LDPC (SC-LDPC) codes can be seen as an example of (terminated) LDPC-CC [58] due to the fact that spatial coupling is equivalent to introducing memory into the process of encoding. It was shown that spatially coupled codes were capacity achieving. The scheme of unwrapping a cyclic block code into a convolutional structure was introduced by Tanner [56]. Felström and Zigangirov first introduced the low-density convolutional ensembles [59]. The mechanism explaining why convolutional LDPC ensembles perform so well over the binary erasure channel (BEC) was provided in [55]. SC-LDPC codes can be constructed by coupling a series of L_{SC} disjoint or uncoupled LDPC codes (each one with a length of M_{UC} bits) together with certain boundary conditions, where L_{SC} is the length of the SC-LDPC chain. If M_{UC} goes to infinity and L_{SC} is sufficiently large, the SC-LDPC ensembles showed a BP threshold which is very close to the MAP threshold of uncoupled LDPC codes [55]. Protograph-based spatially coupled LDPC convolutional codes (SC-LDPC-CC) were constructed by applying an edge spreading operation in [60]. A protograph [61] is a small bipartite graph $(\mathbb{V}, \mathbb{C}, \mathbb{E})$. Assuming the design rate $r = 1 - n_c/n_v$, a protograph connects a set of n_v VNs $\mathbb{V} = (v_0, \ldots, v_{n_v-1})$ to a set of n_c CNs $\mathbb{C} = (c_0, \ldots, c_{n_c-1})$ by a set of edges $\mathbb{E}$. Edge spreading is an operation for spatial coupling to generate convolutional protographs. An illustration of protographs with the operation of edge spreading is given in Fig. 1.7. SC-LDPC codes can achieve capacity for binary-input memoryless output-symmetric channels with iterative decoding [62]. The minimum distance properties can be improved by the inherent structure of the protograph-based SC-LDPC codes [63]. It was shown that irregular protograph-based LDPC-BCs often exhibit better thresholds than the unstructured irregular codes given the same degree distributions [64].

1.3.4 Quasi-Cyclic LDPC Codes

QC-LDPC codes form a significant subclass of LDPC codes. A QC-LDPC code can be described by a parity-check matrix $\mathbf{H}_{PC}$ that consists of small square sub-matrices, which are either null matrices or circulant permutation matrices. A $\mathfrak{N} \times \mathfrak{N}$ permutation matrix $\mathbf{P}^\mathfrak{n}$ can be obtained through shifting the identity matrix $\mathbf{I}$ of the same size to the left or right by $\mathfrak{n}$ times, where $\mathfrak{n}$ is an integer and $0 \leq \mathfrak{n} < \mathfrak{N}$. For example, a 3×3 permutation matrix is expressed as

$$\mathbf{P} = \begin{bmatrix} 0 & 1 & 0 \\ 0 & 0 & 1 \\ 1 & 0 & 0 \end{bmatrix}, \tag{1.32}$$

which circularly shifts the 3×3 identity matrix $\mathbf{I}$ to the right by one time. A $m\mathfrak{N} \times n\mathfrak{N}$ parity-check matrix $\mathbf{H}_{PC}$ contains $m \times n$ permutation sub-matrices (null matrices may be included), which
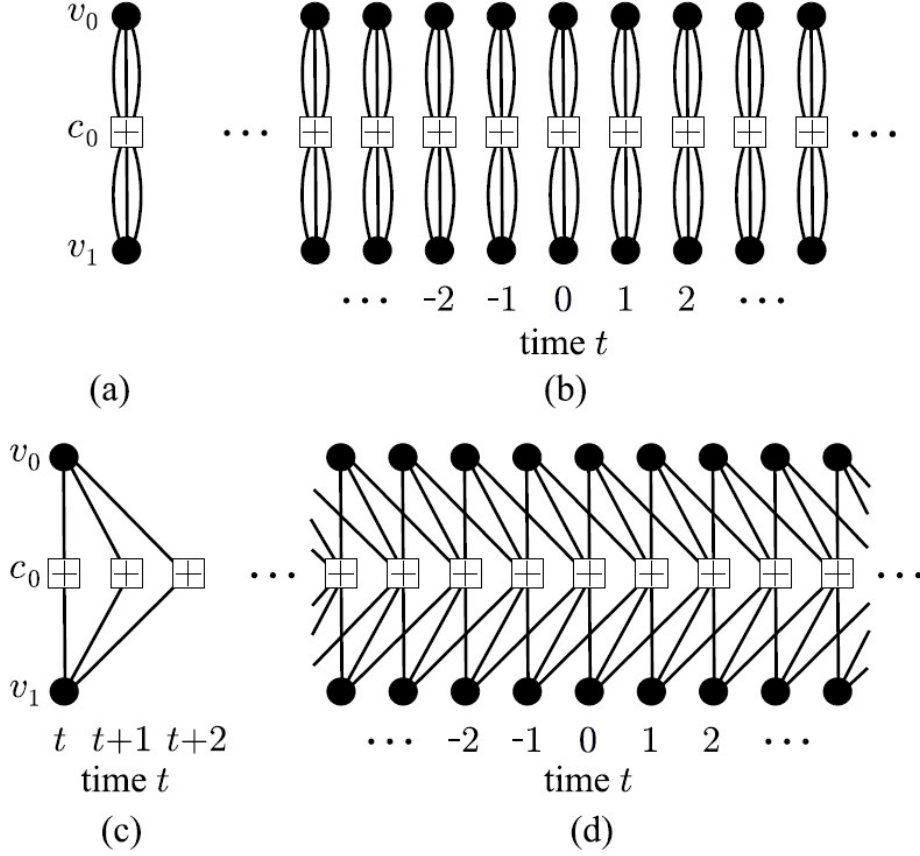
Figure 1.7: (a) Protograph representing a $(3,6)$-regular LDPC-BC ensemble, (b) sequence of $(3,6)$-regular LDPC-BC protographs, (c) edge spreading for one segment of the graph at time t with a coupling width of 2, (d) protograph representing a spatially coupled $(3,6)$-regular LDPC-CC ensemble with a coupling width of 2 [60].

corresponds to a QC-LDPC code of length $n \times \mathfrak{N}$. The code rate of such a code is $r = (n\mathfrak{N} - m\mathfrak{N})/n\mathfrak{N} = 1 - m/n$ if $\mathbf{H}_{PC}$ is of full rank. QC-LDPC codes can be constructed to be regular or irregular codes by placing different sub-matrices in $\mathbf{H}_{PC}$. QC-LDPC codes are attractive especially in the sense of implementation because they can be encoded efficiently and implemented with simple shift registers [65]. In addition, QC-LDPC codes can be efficiently decoded using SPA decoders [66].

Chapter 2

Union Bound on the Bit Error Rate for MIMO-GFDM Systems

Résumé

Dans ce chapitre, une borne d'union pour le taux d'erreur sur les bits (BER) pour les systèmes généralisés de multiplexage par répartition en fréquence à entrées multiples et sorties multiples (MIMO-GFDM) est dérivée en se basant sur des paires de probabilités d'erreur (PEP) exactes. La fonction génératrice de moments (MGF) est utilisée pour calculer la paire de probabilités d'erreur exactes en supposant qu'un détecteur par maximum de vraisemblance (ML) est utilisé au récepteur. Un environnement de canal MIMO à trajets multiples réaliste est étudié dans lequel la corrélation spatiale entre les antennes et les erreurs d'estimation de canal sont incluses. Le modèle de Kronecker et un modèle additif sont utilisés pour décrire respectivement les erreurs de corrélation spatiale et d'estimation de canal. Les impacts de la corrélation spatiale et des erreurs d'estimation de canal sur la borne dérivée sont également étudiés. Des calculs numériques pour la borne d'union et des simulations de Monte-Carlo pour calculer le BER sont effectués pour vérifier la borne d'union. Les résultats numériques montrent que la borne d'union est une limite supérieure serrée du BER pour les systèmes MIMO-GFDM.

Abstract

In this chapter, a union bound on the bit error rate (BER) for multiple input multiple output generalized frequency division multiplexing (MIMO-GFDM) systems is derived based on exact pairwise error probabilities. The moment-generating function (MGF) is used to calculate the exact pairwise error probability (PEP) under the assumption that a maximum likelihood (ML) detector is used at the receiver. A realistic multipath MIMO channel environment is investigated in which the spatial correlation between antennas and the channel estimation errors are included. The Kronecker model and an additive model are used to describe the spatial correlation and channel estimation errors, respectively. The

impacts of the spatial correlation and the channel estimation errors on the derived bound are also investigated. Numerical calculations of the union bound and computer-based Monte-Carlo simulations of BER are carried out to verify the derived bound. Numerical results show that the derived union bound is a tight upper bound on the BER for MIMO-GFDM systems.

2.1 Introduction

Generalized frequency division multiplexing (GFDM) is a block-based multi-carrier modulation scheme which can generate flexibly configurable waveforms [10, 1]. Each GFDM block consists of a number of sub-carriers and sub-symbols and the block size is configurable to meet different requirements. The sub-carriers are filtered with time- and frequency-shifted prototype pulses. Because of the filtering operation in GFDM, the level of the out-of-band (OOB) radiation can be reduced, which is important for dynamic spectrum allocation and fragmented spectrum scenarios, such as cognitive radio (CR) systems [67]. Another important feature of GFDM is the non-orthogonality between the sub-carriers introduced by the filtering operation, which is the main difference to the orthogonal frequency division multiplexing (OFDM) system. A cyclic prefix (CP) and cyclic suffix (CS) can be added to an entire GFDM block instead of each symbol, which consequently increases the spectral efficiency. Therefore, GFDM is efficient in relaxing the synchronization requirements with CP and CS addition for machine type communications (MTC) [68]. By limiting the block size, GFDM has the potential to enable low-latency applications, such as the Tactile Internet [69]. Therefore, GFDM is a promising candidate waveform technology for beyond 5G.

It has been shown that multiple input multiple output (MIMO) technology can provide high capacity [70] and reliability for wireless systems. Effective detection techniques are required to recover the signals in MIMO systems and maximum likelihood (ML) detection is an optimal detection technique. The application of MIMO technology in GFDM systems can provide high throughput and flexibility at the same time. The MIMO-GFDM system, in fact, outperforms the MIMO-OFDM system in terms of error performance in multipath fading channels [71, 72]. In order to investigate the potentialities of MIMO-GFDM systems, effective tools for evaluating the system performance are necessary. A common approach to approximate the bit error rate (BER) is using a union bound [73]. Despite the fact that ML detection has high complexity for MIMO-GFDM systems [72, 74], it is useful to find union bounds on BER using the ML criterion due to its optimality. This can offer a benchmark for the receiver design in MIMO-GFDM systems. The union bound can be derived from the pairwise error probability (PEP) and the exact calculation of PEP is the key to obtain a tight bound on BER. Techniques for the calculation of exact PEP have been presented in [75, 76]. In [75], a general derivation of PEP using Gauss-Chebyshev quadrature and moment-generating function (MGF) was presented and applied to independent and block fading MIMO channels. The MGF-based approach can also be used in the calculation of the exact PEP over spatially correlated MIMO channels and has been evaluated in realistic propagation environments [76]. The derivation of PEP from another perspective has been proposed in [77], where the probability density function-based approach was used to calculate the

PEP over correlated MIMO channels and certain error types were introduced to evaluate the error performance.

Motivated by MIMO-GFDM systems ability to be applied to diversified future wireless scenarios and the need to develop effective performance evaluation tools, in this chapter, we derive a union bound on the BER for MIMO-GFDM systems over realistic multipath fading channels. The MIMO system operates in a spatial multiplexing mode and the ML detection is used at the receiver. The effect of filtering in GFDM is included in an equivalent channel matrix. The Kronecker model [78] is used to formulate the spatial correlation in MIMO Rayleigh channels and we use an additive model to describe the imperfect channel state information (CSI). Numerical calculations and Monte-Carlo simulations are carried out to evaluate the derived union bound.

The rest of the chapter is organized as follows. The system model is described in Section 2.2. The union bound on the BER for MIMO-GFDM systems is derived based on exact PEPs in Section 2.3. Numerical results are presented in Section 2.4 to evaluate the derived union bound. Section 2.5 concludes the chapter.

Notation: Scalars are denoted by italic lower/upper case letters. Vectors are denoted by bold lower case letters. Matrices are denoted by bold upper case letters. $a_{i,j}$ refers to the $(i, j)^{\text{th}}$ element of matrix $\mathbf{A}$. $\mathbf{I}$ denotes the identity matrix. $(\cdot)^{\text{T}}$ and $(\cdot)^{\text{H}}$ denote the matrix transpose and conjugate transpose, respectively. $\|\cdot\|$ denotes the Euclidean norm of a vector. $\otimes$ denotes the Kronecker product. $(\cdot)^{1/2}$ denotes the matrix square root.

2.2 System Description

As shown in Fig. 2.1, the MIMO channel consists of N_{t} transmit antennas and N_{r} receive antennas. The serial input symbols $\mathbf{d}$ are demultiplexed into N_{t} parallel streams, each of which, denoted by $\mathbf{d}_t$ ($t = 1, 2, \ldots, N_{\text{t}}$), corresponds to a symbol vector processed at the tth transmit antenna. At each transmit antenna, the symbols $\mathbf{d}_t$ go through a GFDM modulation block of length $N = K \times M$ to produce the transmit signal. The details of the GFDM modulation are shown in Fig. 2.2, where the transmit antenna index 't' is omitted for simplicity.

The transmit signal is given by [1]

$$x_t[n] = \sum_{k=0}^{K-1} \sum_{m=0}^{M-1} g_{k,m}[n] d_t^{k,m}, \quad n = 0, \ldots, N-1, \tag{2.1}$$

where N is the total number of symbols and K and M are the number of sub-carriers and sub-symbols, respectively. n is the sampling index, $x_t[n]$ is the transmit signal at the tth transmit antenna and $d_t^{k,m}$ denotes the symbol transmitted on the kth sub-carrier and in the mth sub-symbol of the GFDM block at the tth transmit antenna. $g_{k,m}[n]$ is obtained by the time and frequency shift of a prototype filter $g[n]$.

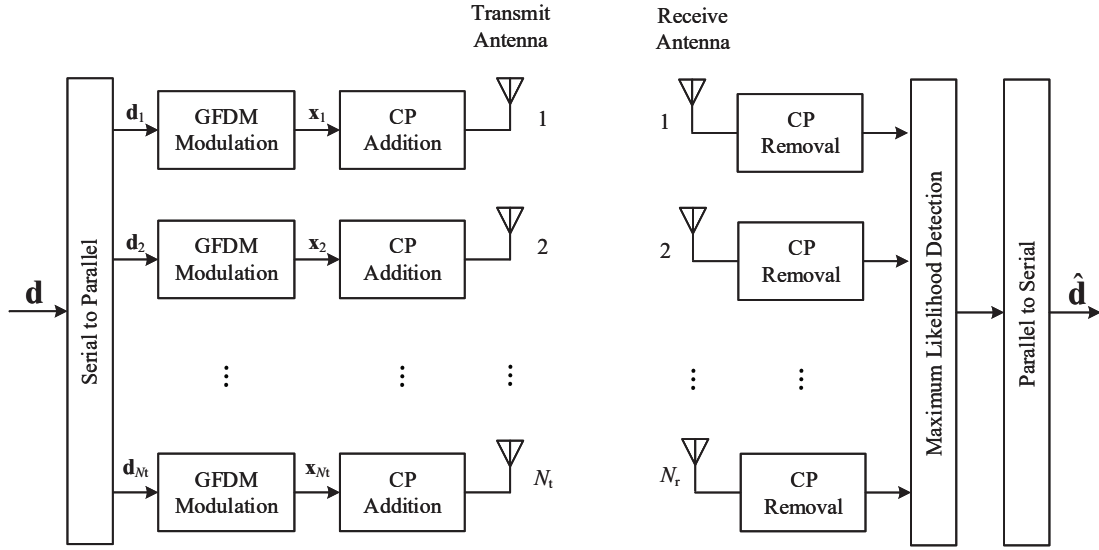$$g_{k,m}[n] = g[(n - mK) \bmod N]e^{j2\pi \frac{k}{K} n}. \tag{2.2}$$

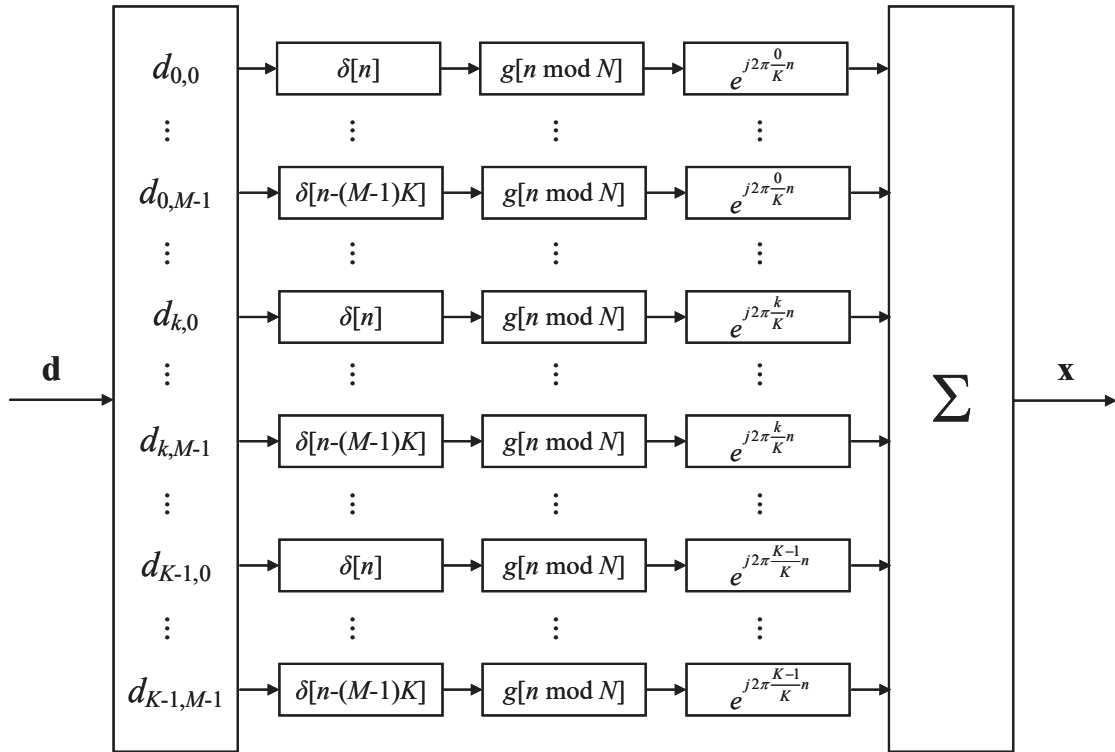Figure 2.1: Transceiver diagram of an MIMO-GFDM system.

Figure 2.2: Details of the GFDM modulation.

26

The prototype filter can be chosen from raised cosine (RC) filters, root raised cosine (RRC) filters, etc. For example, if the prototype filter is an RC pulse, we have

$$g[n] = \frac{\sin(\pi n/T_\mathrm{s})}{\pi n/T_\mathrm{s}} \frac{\cos(\pi \omega n/T_\mathrm{s})}{1 - 4\omega^2 n^2/T_\mathrm{s}^2}, \tag{2.3}$$

where T_s is the symbol duration and ω is the roll-off factor. Note that we use the same GFDM block for all the streams. If we write (2.1) in a compact form, we have

$$\mathbf{x}_t = \mathbf{A}\mathbf{d}_t, \tag{2.4}$$

where $\mathbf{x}_t = (x_t[0], x_t[1], \ldots, x_t[N-1])^\mathrm{T}$ and

$$\mathbf{d}_t = \left(\left(\mathbf{d}_t^0\right)^\mathrm{T}, \left(\mathbf{d}_t^1\right)^\mathrm{T}, \ldots, \left(\mathbf{d}_t^{K-1}\right)^\mathrm{T} \right)^\mathrm{T} \tag{2.5}$$

with

$$\mathbf{d}_t^k = \left(d_t^{k,0}, d_t^{k,1}, \ldots, d_t^{k,M-1} \right)^\mathrm{T}. \tag{2.6}$$

The $N \times N$ transmitter matrix is denoted by

$$\mathbf{A} = \begin{pmatrix} \mathbf{g}_{0,0} & \mathbf{g}_{0,1} & \cdots & \mathbf{g}_{0,M-1} & \mathbf{g}_{1,0} & \cdots & \mathbf{g}_{K-1,M-1} \end{pmatrix} \tag{2.7}$$

where $\mathbf{g}_{k,m} = (g_{k,m}[0], g_{k,m}[1], \ldots, g_{k,m}[N-1])^\mathrm{T}$.

After the addition of a CP, $x_t[n]$ is transmitted through a quasi-static Rayleigh fading channel which is assumed to be constant over one GFDM block and to vary from one block to another.

2.3   Derivation of the Union Bound on Bit Error Rate

In this section, we derive a generic union bound on the BER for MIMO-GFDM systems under realistic multipath channel environments. In practical applications, the wireless channels need to be estimated and estimation errors are usually inevitable. It is necessary to investigate the influence of estimation errors on the system performance. In addition, spatial correlation exists between antennas in many MIMO wireless systems. Therefore, in order to describe the realistic channel as accurately as possible, we incorporate the channel estimation error and spatial correlation into the channel model.

After CP removal, the signals at the receive antennas are given by

$$\begin{bmatrix} \mathbf{y}_1 \\ \vdots \\ \mathbf{y}_{N_\mathrm{r}} \end{bmatrix} = \begin{bmatrix} \mathbf{H}_{1,1}\mathbf{A} & \cdots & \mathbf{H}_{1,N_\mathrm{t}}\mathbf{A} \\ \vdots & \ddots & \vdots \\ \mathbf{H}_{N_\mathrm{r},1}\mathbf{A} & \cdots & \mathbf{H}_{N_\mathrm{r},N_\mathrm{t}}\mathbf{A} \end{bmatrix} \begin{bmatrix} \mathbf{d}_1 \\ \vdots \\ \mathbf{d}_{N_\mathrm{t}} \end{bmatrix} + \mathbf{n}, \tag{2.8}$$

where $\mathbf{y}_i$ ($i = 1, 2, \ldots, N_\mathrm{r}$) denotes the signal received at the ith receive antenna. $\mathbf{H}_{r,t}$ ($r = 1, 2, \ldots, N_\mathrm{r}$ and $t = 1, 2, \ldots, N_\mathrm{t}$) is a circulant convolution matrix of size $N \times N$ which denotes the channel matrix between the tth transmit antenna and the rth receive antenna. $\mathbf{n} \sim \mathcal{CN}(\mathbf{0}, N_0\mathbf{I}_{N_\mathrm{r}N})$ denotes additive white Gaussian noise.

We use the well-known Kronecker model to describe the correlated channel. The Kronecker model is based on the assumption that the correlation between transmit antennas is independent of that between receive antennas. This model is valid when the transmitter and receiver are separated by enough distance and are only affected by the scatterers around them. Combined with the tapped delay line (TDL) channel model, for a given tap l, the channel matrix with the Kronecker model can be written as [79]

$$\mathbf{H}_{\mathrm{K}l} = \mathbf{R}_{\mathrm{r}l}^{1/2} \mathbf{G}_l \left(\mathbf{R}_{\mathrm{t}l}^{1/2} \right)^{\mathrm{T}}, \tag{2.9}$$

where $\mathbf{R}_{\mathrm{t}l} = \mathrm{E} \left[\mathbf{H}_{\mathrm{K}l}^{\mathrm{H}} \mathbf{H}_{\mathrm{K}l} \right]^{\mathrm{T}}$ and $\mathbf{R}_{\mathrm{r}l} = \mathrm{E} \left[\mathbf{H}_{\mathrm{K}l} \mathbf{H}_{\mathrm{K}l}^{\mathrm{H}} \right]$ are the transmit and receive correlation matrices of the lth path, respectively. $\mathbf{G}_l$ is populated with i.i.d. complex Gaussian random variables with zero mean and unit variance (0.5 per dimension), as follows

$$\mathbf{G}_l = \begin{bmatrix} g_{1,1}^l & \cdots & g_{1,N_t}^l \\ \vdots & \ddots & \vdots \\ g_{N_r,1}^l & \cdots & g_{N_r,N_t}^l \end{bmatrix}, \tag{2.10}$$

where the entry $g_{r,t}^l$ ($l = 1, 2, \ldots, L$) denotes the channel gain of the lth path between the tth transmit antenna and the rth receive antenna. It should be noted that no channel estimation error is assumed in (2.9).

An additive model [80, 81] is used to describe the channel estimation errors. In the case of uncorrelated channels,

$$\hat{g}_{r,t}^l = g_{r,t}^l + \varepsilon_{r,t}^l, \tag{2.11}$$

where $\hat{g}_{r,t}^l$ is the estimate of $g_{r,t}^l$ and is a zero-mean complex Gaussian random variable that is dependent of $g_{r,t}^l$. $\varepsilon_{r,t}^l$ is the channel estimation error, which is a Gaussian variable with mean zero and variance σ_ε^2 and is independent of $g_{r,t}^l$.

Now we include simultaneously the Kronecker and additive channel estimation models in the MIMO channel. The channel matrix becomes

$$\begin{aligned} \mathbf{H}_l &= \mathbf{H}_{\mathrm{K}l} + \mathbf{E}_l \\ &= \mathbf{R}_{\mathrm{r}l}^{1/2} \mathbf{G}_l \left(\mathbf{R}_{\mathrm{t}l}^{1/2} \right)^{\mathrm{T}} + \mathbf{E}_l, \end{aligned} \tag{2.12}$$

where $\mathbf{E}_l$ is the estimation error matrix with entries $\varepsilon_{r,t}^l$ denoting corresponding channel estimation errors, as follows

$$\mathbf{E}_l = \begin{bmatrix} \varepsilon_{1,1}^l & \cdots & \varepsilon_{1,N_t}^l \\ \vdots & \ddots & \vdots \\ \varepsilon_{N_r,1}^l & \cdots & \varepsilon_{N_r,N_t}^l \end{bmatrix}. \tag{2.13}$$

Note that this channel matrix is a general model which includes the spatial correlation and channel estimation errors at the same time. Special channel cases can be obtained with proper choices of $\mathbf{R}_{\mathrm{r}l}$, $\mathbf{R}_{\mathrm{t}l}$ and $\mathbf{E}_l$. For example, we will get a correlated channel without channel estimation errors if $\mathbf{E}_l$ has all-zero entries and will get a uncorrelated channel if $\mathbf{R}_{\mathrm{r}l} = \mathbf{I}$ and $\mathbf{R}_{\mathrm{t}l} = \mathbf{I}$.

In (2.12), $\mathbf{H}_l$ has the following structure

$$\mathbf{H}_l = \begin{bmatrix} h_{1,1}^l & \cdots & h_{1,N_t}^l \\ \vdots & \ddots & \vdots \\ h_{N_r,1}^l & \cdots & h_{N_r,N_t}^l \end{bmatrix}. \tag{2.14}$$

With some rearrangements, we have

$$\mathbf{H}_{r,t} = \begin{bmatrix} h_{r,t}^1 & 0 & \cdots & 0 & h_{r,t}^L & \cdots & h_{r,t}^2 \\ \vdots & h_{r,t}^1 & & \vdots & 0 & \ddots & \vdots \\ \vdots & \vdots & \ddots & 0 & \vdots & & h_{r,t}^L \\ h_{r,t}^L & \vdots & & h_{r,t}^1 & 0 & & 0 \\ 0 & h_{r,t}^L & & \vdots & h_{r,t}^1 & & \vdots \\ \vdots & 0 & \ddots & \vdots & \vdots & \ddots & 0 \\ 0 & \vdots & \cdots & h_{r,t}^L & \vdots & \cdots & h_{r,t}^1 \end{bmatrix}. \tag{2.15}$$

For the convenience of notation, we rewrite (2.8) in the following form

$$\mathbf{y} = \mathbf{\breve{H}}\mathbf{d} + \mathbf{n}, \tag{2.16}$$

where $\mathbf{y} = (\mathbf{y}_1^T, \mathbf{y}_2^T \ldots, \mathbf{y}_{N_r}^T)^T$, $\mathbf{d} = (\mathbf{d}_1^T, \mathbf{d}_2^T, \ldots, \mathbf{d}_{N_t}^T)^T$ and

$$\mathbf{\breve{H}} = \begin{bmatrix} \mathbf{H}_{1,1}\mathbf{A} & \cdots & \mathbf{H}_{1,N_t}\mathbf{A} \\ \vdots & \ddots & \vdots \\ \mathbf{H}_{N_r,1}\mathbf{A} & \cdots & \mathbf{H}_{N_r,N_t}\mathbf{A} \end{bmatrix}. \tag{2.17}$$

The entries of $\mathbf{H}_{r,t}\mathbf{A}$ are linear transformations of the channel impulse vector $\mathbf{h}_{r,t} = (h_{r,t}^1, h_{r,t}^2, \ldots, h_{r,t}^L)$ and therefore, are complex Gaussian variables with zero mean. Consequently, all the entries of $\mathbf{\breve{H}}$ are complex Gaussian variables with zero mean.

At the receiver, we use an ML detector to process the received signal. The ML detector makes a decision based on the minimal Euclidean distance between the received and estimated signal as follows

$$\mathbf{\hat{d}} = \arg\min_{\mathbf{d} \in \mathcal{D}} \left\| \mathbf{y} - \mathbf{\breve{H}}\mathbf{d} \right\|^2, \tag{2.18}$$

where $\mathcal{D}$ is the set of all possible transmitted symbol vectors. The PEP is defined as the error probability when $\mathbf{d}$ is sent but erroneously detected as $\mathbf{\hat{d}}$ and is denoted as $P(\mathbf{d} \to \mathbf{\hat{d}})$. The PEP conditioned on $\mathbf{\breve{H}}$ is calculated as [82]

$$P(\mathbf{d} \to \mathbf{\hat{d}} | \mathbf{\breve{H}}) = Q_n\left(\sqrt{\frac{E_s}{2N_0} d^2(\mathbf{d}, \mathbf{\hat{d}})}\right), \tag{2.19}$$

where E_s is the energy per symbol at each transmit antenna.

$$Q_n(x) = \frac{1}{\sqrt{2\pi}} \int_x^\infty e^{-t^2/2} dt \tag{2.20}$$

and

$$d^2\left(\mathbf{d},\hat{\mathbf{d}}\right) = \left\|\check{\mathbf{H}} \cdot \left(\mathbf{d} - \hat{\mathbf{d}}\right)\right\|^2, \tag{2.21}$$

which is the Euclidean distance between $\check{\mathbf{H}}\mathbf{d}$ and $\check{\mathbf{H}}\hat{\mathbf{d}}$. The exact PEP can be obtained by averaging the conditional PEP in (2.19) over the distribution of channel gains

$$P\left(\mathbf{d} \to \hat{\mathbf{d}}\right) = \mathrm{E}\left[Q_{\mathrm{n}}\left(\sqrt{\frac{E_s}{2N_0}d^2\left(\mathbf{d},\hat{\mathbf{d}}\right)}\right)\right]. \tag{2.22}$$

Let $\mathbf{d}_\Delta = \mathbf{d} - \hat{\mathbf{d}}$. We have

$$\begin{aligned}
d^2\left(\mathbf{d},\hat{\mathbf{d}}\right) &= \left\|\check{\mathbf{H}}\mathbf{d}_\Delta\right\|^2 \\
&= \sum_{i=1}^{NN_{\mathrm{r}}} \check{\mathbf{h}}_i \mathbf{d}_\Delta \mathbf{d}_\Delta^{\mathrm{H}} \check{\mathbf{h}}_i^{\mathrm{H}} \\
&= \left[\check{\mathbf{h}}_1,\ldots,\check{\mathbf{h}}_{NN_{\mathrm{r}}}\right]\left[\mathbf{I}_{NN_{\mathrm{r}}} \otimes \left(\mathbf{d}_\Delta \mathbf{d}_\Delta^{\mathrm{H}}\right)\right]\left[\check{\mathbf{h}}_1,\ldots,\check{\mathbf{h}}_{NN_{\mathrm{r}}}\right]^{\mathrm{H}},
\end{aligned} \tag{2.23}$$

where $\check{\mathbf{h}}_i$ denotes the ith row of the matrix $\check{\mathbf{H}}$.

Based on [83], we have the following fact. Let $\mathbf{B}$ be a Hermitian matrix and $\mathbf{z}$ be a circularly symmetric complex Gaussian vector with mean $\boldsymbol{\mu}_{\mathrm{z}}$ and covariance matrix $\mathbf{C}_{\mathrm{z}}$, i.e., $\mathbf{z} \sim \mathcal{CN}(\boldsymbol{\mu}_{\mathrm{z}}, \mathbf{C}_{\mathrm{z}})$. The MGF of the quadrature form $q = \mathbf{z}\mathbf{B}\mathbf{z}^{\mathrm{H}}$ is

$$\begin{aligned}
\mathcal{M}_q(s) &= \int_0^\infty e^{sq} p_q(q)\mathrm{d}q \\
&= \frac{\exp\left(s\boldsymbol{\mu}_{\mathrm{z}}\mathbf{B}\left(\mathbf{I} - s\mathbf{C}_{\mathrm{z}}\mathbf{B}\right)^{-1}\boldsymbol{\mu}_{\mathrm{z}}^{\mathrm{H}}\right)}{\det\left(\mathbf{I} - s\mathbf{C}_{\mathrm{z}}\mathbf{B}\right)},
\end{aligned} \tag{2.24}$$

where s is a complex number and $p_q(q)$ denotes the probability density function of q.

Now let $\mathbf{z} = \left[\check{\mathbf{h}}_1,\ldots,\check{\mathbf{h}}_{NN_{\mathrm{r}}}\right]$ with mean $\boldsymbol{\mu}_{\mathrm{z}} = \mathbf{0}$ and covariance matrix $\mathbf{C}_{\mathrm{z}}$. $\mathbf{B} = \left(E_s/\left(2N_0\right)\right)\mathbf{I}_{NN_{\mathrm{r}}} \otimes \left(\mathbf{d}_\Delta \mathbf{d}_\Delta^{\mathrm{H}}\right)$. $\Gamma = \mathbf{z}\mathbf{B}\mathbf{z}^{\mathrm{H}} = \left(E_s/\left(2N_0\right)\right)d^2\left(\mathbf{d},\hat{\mathbf{d}}\right)$, then

$$\mathcal{M}_\Gamma(s) = \det\left(\mathbf{I} - \left(E_s/2N_0\right)s\mathbf{C}_{\mathrm{z}}\left(\mathbf{I}_{NN_{\mathrm{r}}} \otimes \left(\mathbf{d}_\Delta \mathbf{d}_\Delta^{\mathrm{H}}\right)\right)\right)^{-1}. \tag{2.25}$$

Following [75], let $\Phi_\Gamma(s) = \mathcal{M}_\Gamma(-s) = \mathrm{E}\left[e^{-s\Gamma}\right]$ and $\Delta = \Gamma - \vartheta^2$ (ϑ is a real Gaussian random variable with zero mean and unit variance). We have

$$\begin{aligned}
P\left(\mathbf{d} \to \hat{\mathbf{d}}\right) &= \mathrm{E}\left[Q_{\mathrm{n}}\left(\sqrt{\Gamma}\right)\right] \\
&= \frac{1}{2}P\left(\Delta < 0\right) \\
&= \frac{1}{2\pi j}\int_{c-j\infty}^{c+j\infty}\frac{\Phi_\Delta(s)}{2s}\mathrm{d}s,
\end{aligned} \tag{2.26}$$

where c is a real number in the region of convergence of $\Phi_\Delta(s)$, and

$$\begin{aligned}
\Phi_\Delta(s) &= \mathrm{E}\left[e^{-s\Delta}\right] \\
&= \Phi_\Gamma(s)\Phi_{\vartheta^2}(-s) \\
&= \Phi_\Gamma(s)(1-2s)^{-\frac{1}{2}}.
\end{aligned} \tag{2.27}$$

30

Methods for properly selecting c have been reported in [75, 84] and the references therein. Rewrite (2.26) by expanding the real and imaginary parts of s and we have

$$
\begin{aligned}
P\left(\mathbf{d} \to \hat{\mathbf{d}}\right) &= \frac{1}{2\pi j} \int_{c-j\infty}^{c+j\infty} \frac{\Phi_\Delta\left(c+j\varphi\right)}{2\left(c+j\varphi\right)} \mathrm{d}\left(c+j\varphi\right) \\
&= \frac{1}{4\pi} \int_{-\infty}^{+\infty} \frac{c\mathrm{Re}\left[\Phi_\Delta\left(c+j\varphi\right)\right]+\varphi\mathrm{Im}\left[\Phi_\Delta\left(c+j\varphi\right)\right]}{c^2+\varphi^2} \mathrm{d}\varphi.
\end{aligned}
\tag{2.28}
$$

Using the change of variable $\varphi = c\sqrt{1-x^2}/x$, (2.28) becomes

$$
P\left(\mathbf{d} \to \hat{\mathbf{d}}\right) = \frac{1}{4\pi} \int_{-1}^{1} \left(\mathrm{Re}\left[\Phi_\Delta\left(c+j\frac{c\sqrt{1-x^2}}{x}\right)\right] + \frac{\sqrt{1-x^2}}{x}\mathrm{Im}\left[\Phi_\Delta\left(c+j\frac{c\sqrt{1-x^2}}{x}\right)\right] \right) \frac{\mathrm{d}x}{\sqrt{1-x^2}}.
\tag{2.29}
$$

Note that (2.29) is of the form $\int_{-1}^{1} \left(f\left(x\right)/\sqrt{1-x^2}\right) \mathrm{d}x$. Therefore, it can be numerically computed using the Gauss-Chebyshev quadrature rule with v nodes, as follows

$$
P\left(\mathbf{d} \to \hat{\mathbf{d}}\right) = \frac{1}{4v} \sum_{k=1}^{v} \left(\mathrm{Re}\left[\Phi_\Delta\left(c\left(1+j\tau_k\right)\right)\right] + \tau_k\mathrm{Im}\left[\Phi_\Delta\left(c\left(1+j\tau_k\right)\right)\right]\right) + E_v,
\tag{2.30}
$$

where $\tau_k = \tan\left(\left(k-1/2\right)\pi/v\right)$. E_v is an error term which goes to 0 as v goes to infinity. In practice, one can determine the parameter v by computing (2.30) for increasing values of v. For example, a value can be chosen for v if the resulting value of (2.30) does not change significantly when v reaches that value.

Then the union bound on the BER is defined as the weighted sum of all PEPs, given by [15]

$$
P_{\mathrm{UB}} = \sum_{\mathbf{d}} \sum_{\hat{\mathbf{d}}|\hat{\mathbf{d}}\neq\mathbf{d}} r\left(\mathbf{d},\hat{\mathbf{d}}\right) P\left(\mathbf{d} \to \hat{\mathbf{d}}\right) P\left(\mathbf{d}\right),
\tag{2.31}
$$

where $P\left(\mathbf{d}\right)$ is the a priori probability that $\mathbf{d}$ is transmitted. $r\left(\mathbf{d},\hat{\mathbf{d}}\right)$ is the error ratio when $\mathbf{d}$ is sent but $\hat{\mathbf{d}}$ is detected. $r\left(\mathbf{d},\hat{\mathbf{d}}\right)$ can be defined as $r\left(\mathbf{d},\hat{\mathbf{d}}\right) = N_e/N_b$, where N_e is the number of erroneous bits due to the detection error $\left(\mathbf{d} \to \hat{\mathbf{d}}\right)$ and N_b is the number of the bits per symbol vector.

2.4   Numerical Results

We evaluate the union bounds on BER by carrying out numerical simulations. 16-QAM (quadrature amplitude modulation) is used to generate the symbol vector which is the input of the GFDM unit. In the GFDM unit, $K = 16$ and $M = 5$. An RC pulse with roll-off factor $\omega = 0.5$ is used as the prototype pulse shaping filter. $L = 3$, that is, there are 3 paths in the channel of each transmit-receive antenna pair. $c = 1/4$ and $v = 64$. For the case of uncorrelated channel and imperfect CSI, we let $\sigma_\varepsilon^2 = 0.01$ to examine the impact of the channel estimation errors on the union bound. Correlation matrices $\mathbf{R}_{tl}$ and $\mathbf{R}_{rl}$ are generated by the exponential model [85], whose components are

$$
r_{ij} = \begin{cases} r^{j-i}, & i \leq j; \\ r_{ji}^*, & i > j. \end{cases}
\tag{2.32}
$$

31

where $|r| \leq 1$ is the correlation coefficient. The value of r reflects the correlation strength between antennas. We let $r = 0.5$ in the simulations to impose the spatial correlation. Simultaneously let $\sigma_{\varepsilon}^2 = 0.01$ and $r = 0.5$ for the case of correlated channel and imperfect CSI. The exact union bounds on BER for the four different cases are shown in Fig. 2.3 for 2×2 MIMO. Corresponding BER simulation results are also shown in the figure to demonstrate the accuracy of the union bounds. From Fig. 2.3, it can be seen that the derived exact union bounds are tight for the BER in the high signal-to-noise ratio (SNR) region for all cases. The system with imperfect CSI shows higher BER than the case of perfect CSI. It is worth noting that fixed σ_{ε}^2's are used here, whereas in practical applications the channel estimation errors decrease as the SNR increases [80]. This is why the curves with $\sigma_{\varepsilon}^2 = 0.01$ exhibit significant performance losses trending toward flatness for high SNR. For a correlated channel, both the derived union bounds and the simulated results show larger BER values than the uncorrelated case. The reason is that the correlation between antennas introduces non-zero entries in the off-diagonal elements of the channel covariance matrix, consequently leading to higher error probability. In the case of correlated channel and imperfect CSI, both the union bound and simulated BER exhibit the highest BER values due to a superposition effect of the channel estimation error and the channel correlation. Therefore, as expected, both channel estimation errors and correlation between antennas contribute to the increase of BER.
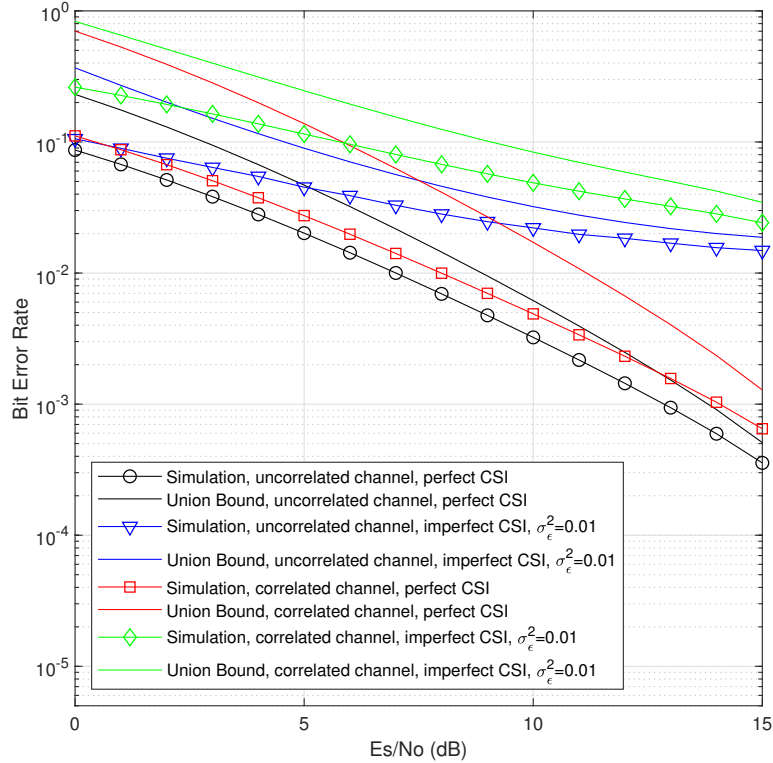

Figure 2.3: Union bounds on BER of MIMO-GFDM systems, $N_{\mathrm{t}} = N_{\mathrm{r}} = 2$.

The derived union bounds on BER and simulation results for 4×4 MIMO channels are shown in Fig. 2.4. Other simulation settings remain the same as in Fig. 2.3. It can be seen that for 4×4 MIMO

channels, both the union bounds and simulated BERs have lower BER values compared to the 2×2 MIMO system while they have similar trends, as expected.
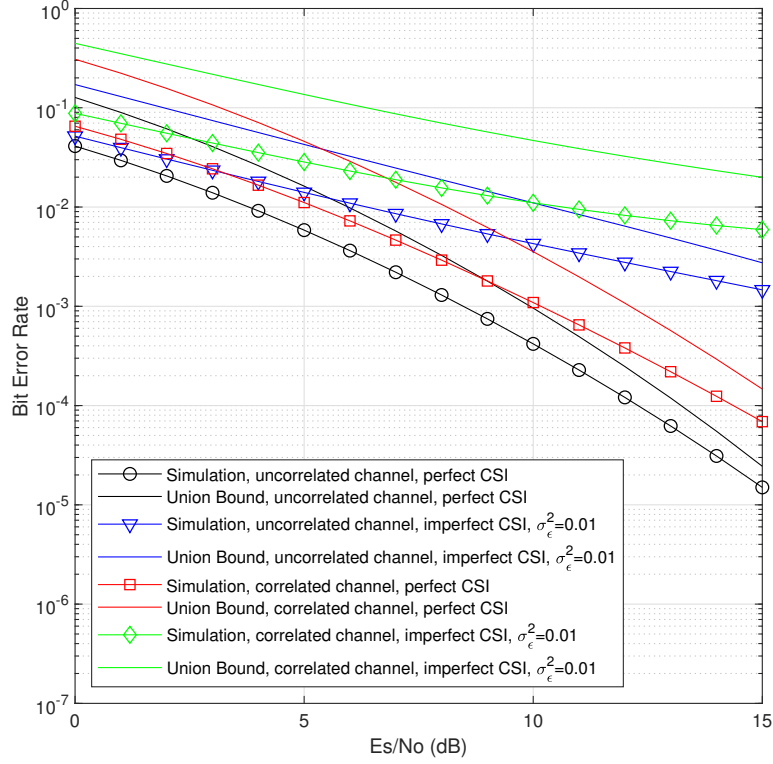

Figure 2.4: Union bounds on BER of MIMO-GFDM systems, $N_t = N_r = 4$.

The impacts of the channel estimation errors and the channel correlation on the derived union bound are shown in Figs. 2.5 and 2.6 for 2×2 and 4×4 MIMO channels, respectively. E_s/N_0 is set to 15 dB. It is shown that both r and σ_ε^2 have significant influences on the derived union bound, specifically, which increases with the increase of these two parameters. In addition, there is a superposition effect of r and σ_ε^2.

2.5 Conclusion

We derived a union bound on the BER for MIMO-GFDM systems over realistic Rayleigh channels. The union bound is obtained from the exact PEPs which are calculated based on an MGF-based approach. We incorporated the effect of filtering in GFDM into an equivalent channel matrix. We investigated the effects of the spatial correlation between antennas and the channel estimation errors on the union bound. Computer-based simulations were performed in four different channel cases to verify the validity of the derived union bound. It is shown that both the spatial correlation and the channel estimation error have significant influence on the BER performance and the derived bound. The derived bound is a tight upper bound for the BER of MIMO-GFDM systems.
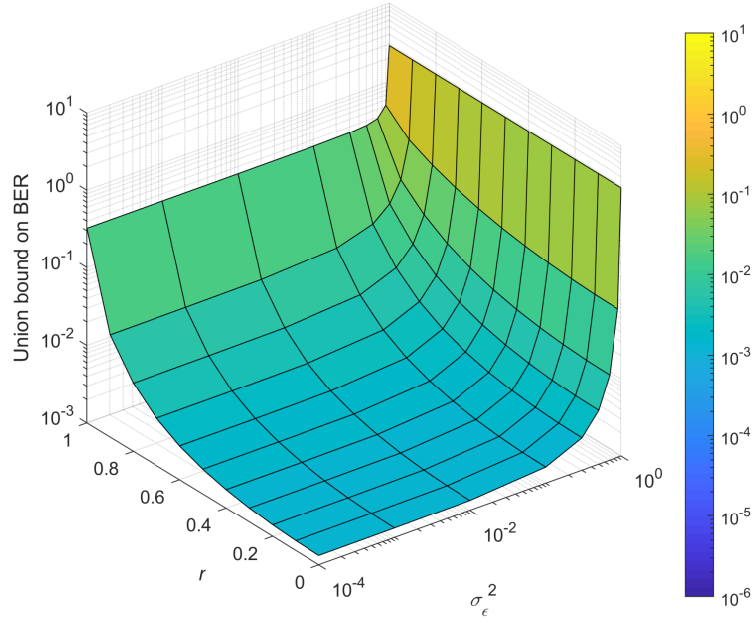
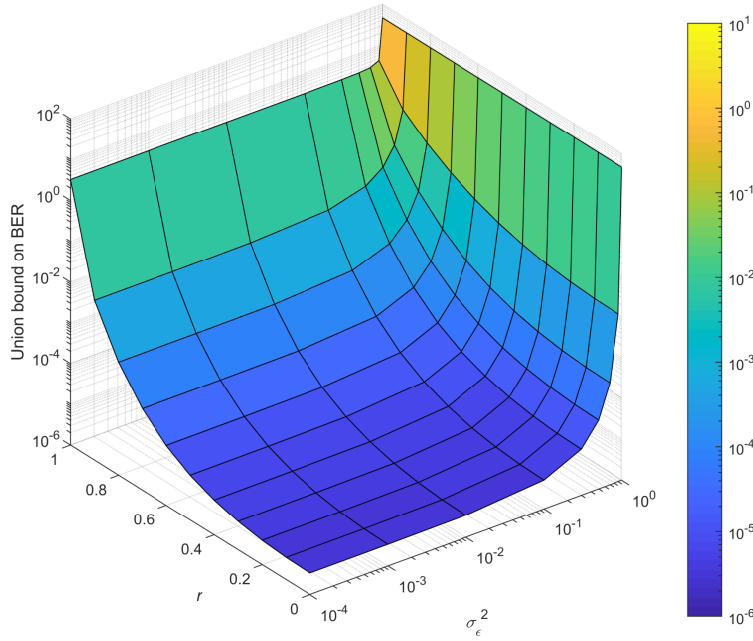Figure 2.5: The impact of r and σ_ε^2 on the union bound on BER, $N_{\text{t}} = N_{\text{r}} = 2$.

Figure 2.6: The impact of r and σ_ε^2 on the union bound on BER, $N_{\text{t}} = N_{\text{r}} = 4$.

Chapter 3

Polynomial Expansion-Based MMSE Channel Estimation and Precoding for Massive MIMO-GFDM Systems

Résumé

Dans ce chapitre, des estimateurs et des précodeurs de canal de faible complexité sont proposés pour des systèmes de multiplexage généralisé par répartition en fréquence combinés à un système à entrées multiples et sorties multiples massif (MIMO-GFDM). Afin de lutter contre l'effet de la non-orthogonalité dans le GFDM, des pilotes sans interférence sont utilisés dans le domaine des fréquences pour l'estimation du canal par l'erreur quadratique moyenne minimale (MMSE). Une expansion polynomiale est utilisée pour calculer approximativement les inverses des matrices dans l'estimation et le précodage MMSE conventionnels, réduisant par conséquent la complexité de calcul cubique à l'ordre carré. Le degré du polynôme matriciel peut être correctement choisi pour obtenir un compromis entre la complexité et l'estimation ou les performances de précodage. Différents poids peuvent être attribués aux termes de l'expansion polynomiale et les valeurs de ces poids peuvent être optimisées pour obtenir une erreur quadratique moyenne (MSE) minimale. Les limites dérivées pour la MSE des estimateurs proposés peuvent prédire les performances dans la région du E_s/N_0 élevé. Ensuite, nous dérivons une borne inférieure de Cramér-Rao (CRLB) et l'utilisons comme référence pour les estimateurs. De plus, la complexité de calcul et les impacts du degré du polynôme sont également étudiés. Les résultats numériques montrent la précision des estimateurs et des précodeurs de canal proposés.

Abstract

In this chapter, low-complexity channel estimators and precoders are proposed for massive multiple-input multiple-output generalized frequency division multiplexing (MIMO-GFDM) systems. In order to

combat the effect of non-orthogonality in GFDM, interference-free pilots are used in frequency-domain minimum mean square error (MMSE) channel estimation. Polynomial expansion is used to approximately compute the matrix inverses in the conventional MMSE estimation and precoding, consequently reducing the cubic computational complexity to square order. The degree of the matrix polynomial can be properly selected to get a required trade-off between complexity and estimation/precoding performance. Different weights can be assigned to the terms in the polynomial expansion and be optimized to achieve a minimal mean square error (MSE). Derived limits on the MSE of the proposed estimators can predict their performance in the high E_s/N_0 region. Then, we derive a Cramér-Rao lower bound (CRLB) and use it as a benchmark for the estimators. In addition, the related computational complexity and the impacts of the polynomial degree are also investigated. Numerical results show the accuracy of the proposed channel estimators and precoders.

3.1 Introduction

Generalized frequency division multiplexing (GFDM) [10, 1] is a promising non-orthogonal candidate waveform technology [68] for 5G and beyond. It is a block-based multi-carrier modulation scheme. The number of subcarriers and subsymbols and the type of pulse-shaping filters in each block can be flexibly modified to meet different requirements, such as low latency, high data rates and low out-of-band (OOB) radiation. GFDM can meet the low-latency requirement for the Tactile Internet [69] by limiting its block size. The filtering operation in GFDM reduces the OOB radiation, which makes GFDM a good choice for dynamic spectrum allocation in cognitive radio (CR) systems [67]. The subcarriers in GFDM are no longer orthogonal because of the filtering operation. Therefore, apart from inter-symbol interference (ISI), GFDM systems suffer inter-carrier interference (ICI) as well. In multiple-input multiple-output (MIMO) applications, inter-antenna interference (IAI) generally exists and will degrade the signal quality. All the interferences increase the complexity in receiver design. In GFDM, a cyclic prefix (CP) and a cyclic suffix (CS) are assigned to an entire block instead of each symbol, which increases the spectral efficiency and relaxes the related synchronization requirements in machine type communications (MTC) [68]. The application of MIMO technique to GFDM systems can further improve the system performance [86, 87]. In recent years, massive MIMO (also known as large-scale MIMO) architectures are drawing more and more research attention and have evolved from a promising concept to a reality [5, 30, 7, 6, 88]. In massive MIMO, the base stations (BSs) are equipped with a large number of antennas, generally more than 100.

Accurate channel state information (CSI) is a key factor to ensure reliable data transmission in wireless communication systems. Typically, CSI can be obtained with the help of reference signals, i.e., pilots [89, 90]. The GFDM system sends pilots and data within the same time-frequency block and estimates the channel using received pilot signals with a specific estimator. The received pilot signal suffers not only from noise but also from data interference due to the non-orthogonality between subcarriers [91, 92]. Fortunately, interference-free pilots have been proposed to ensure clean pilot observations at the receiver [93]. The minimum mean square error (MMSE) estimator is optimal when the channel

statistics are available [90, 94]. However, the MMSE estimator involves matrix inversion which has cubic computational complexity. Therefore, the direct use of the MMSE channel estimator in massive MIMO systems could result in unacceptable complexity. The polynomial expansion technique can be used to reduce the computational complexity of matrix inversion [95, 96]. The principle of polynomial expansion is to approximate the matrix inverse with a V-degree matrix polynomial which converges to the exact matrix inverse as V goes to infinity. In practical applications, V can be appropriately selected to balance complexity against estimation performance. Polynomial expansion-based low-complexity channel estimators have been recently proposed and validated for massive MIMO systems [97].

Precoding technology enables reliable multi-stream transmission for MIMO systems. Pilot contamination is a common issue in massive MIMO systems due to pilot reuse [98]. Precoding can mitigate the effect of pilot contamination to a certain extent. There are linear and non-linear precoding algorithms. Non-linear precoding methods include dirty-paper coding (DPC) [34], lattice-aided methods [35] and vector perturbation (VP) [36], which bring better performance with more implementation complexity. Linear precoding methods include zero-forcing (ZF), maximum ratio transmission (MRT) and MMSE, which is shown to be the better choice for massive MIMO systems [31]. The ZF precoder transmits the signal only to its target user terminal and is effective if there is no noise or the noise is weak due to its noise amplification effect [99]. The MRT precoder maximizes the signal gain at the target user terminal and is near-optimal when there are much more BS antennas than user terminals [99, 100]. The MMSE precoder is also known as the regularized ZF (RZF) precoder and is a trade-off between the ZF and MRT precoders [101]. Matrix inversion is involved in the implementation of the MMSE precoder and consequently, the direct computation is costly with large dimensions in massive MIMO. In order to reduce the computational complexity of the MMSE precoder, the truncated polynomial expansion-based precoder has been proposed [102, 103].

Motivated by the previous work on polynomial expansion-based detectors, estimators and precoders, in this chapter, we consider low-complexity channel estimation and precoding algorithms in massive MIMO-GFDM systems. We extend the interference-free pilot pattern in [93] to the context of massive MIMO for channel estimation and approximate the matrix inverses in the MMSE estimator and precoder with the related matrix polynomials. For the proposed polynomial expansion-based channel estimators, we derive performance limits on the mean square error (MSE) when the covariance matrix of the noise goes to zero. A Cramér-Rao lower bound (CRLB) is also derived as a benchmark for the estimators. The computational complexity of the channel estimators and precoders is also analyzed. Numerical results verify that the proposed channel estimators and precoders achieve near-optimal performance with lower complexity.

The rest of this chapter is organized as follows. A system model for massive MIMO-GFDM systems in which the uplink pilot transmission and downlink precoding are included is described in Section 3.2. We propose low-complexity polynomial expansion-based MMSE (PE-MMSE) channel estimators for massive MIMO-GFDM systems in Section 3.3. Polynomial expansion-based precoders are proposed in Section 3.4. The computational complexity is analyzed in Section 3.5. Numerical results are presented

in Section 3.6 to verify the proposed estimators. Section 3.7 concludes the chapter.

Notation: Scalars are denoted by italic lower/upper case letters. Vectors are denoted by bold lower case letters. Matrices are denoted by bold upper case letters. $\mathbf{I}_M$ and $\mathbf{0}_M$ denote the identity matrix and the null matrix of size $M \times M$, respectively. $(\cdot)^{\mathrm{T}}$ and $(\cdot)^{\mathrm{H}}$ denote the matrix transpose and conjugate transpose, respectively. $\mathbb{E}(\mathbf{A})$ and $\mathrm{Tr}(\mathbf{A})$ denote the expectation and trace of matrix $\mathbf{A}$, respectively. $\mathrm{vec}(\mathbf{A})$ denotes the vectorization of matrix $\mathbf{A}$ by stacking its columns. $\mathrm{diag}(\mathbf{a})$ denotes a diagonal matrix with the entries of a column vector $\mathbf{a}$ as its diagonal entries. $\mathrm{blkdiag}(\mathbf{A}, \cdots, \mathbf{B})$ denotes a block diagonal matrix with $\mathbf{A}$ being its top-left block entry and $\mathbf{B}$ being its bottom-right block entry. $\mathrm{circ}(\cdot)$ produces a circulant matrix based on its argument. $\|\cdot\|_{\mathrm{F}}$ denotes the Frobenius norm of a vector or a matrix. $\otimes$ and $\circ$ denote the Kronecker product and Hadamard product, respectively. $\circledast$ denotes the circular convolution. $\lfloor \cdot \rfloor$ rounds its argument to the nearest integer less than or equal to it. The big-O notation $O(M^n)$ denotes that complexity is bounded by CM^n for certain $0 < C < \infty$. $a_{i,j}$ refers to the $(i, j)^{\mathrm{th}}$ element of matrix $\mathbf{A}$. b_i denotes the ith element of vector $\mathbf{b}$.

3.2 System Description

3.2.1 Massive MIMO-GFDM System

We consider a massive MIMO system using GFDM modulation. There are K subcarriers and M subsymbols in each GFDM block, containing a total of $N = K \times M$ symbols. The subsymbol at the kth subcarrier and m^{th} time slot is denoted by $d_{k,m}$. All the symbols are processed by pulse shaping filters and superimposed to produce the transmit samples [1]

$$x[n] = \sum_{k=0}^{K-1} \sum_{m=0}^{M-1} g_{k,m}[n] d_{k,m}, \quad n \in \{0, 1, \ldots, N-1\}. \tag{3.1}$$

$g_{k,m}[n]$ is obtained by the time and frequency shift of a prototype filter $g[n]$, as follows

$$g_{k,m}[n] = g[(n - mK) \bmod N] e^{j2\pi \frac{k}{K} n}. \tag{3.2}$$

If we rewrite (3.1) in a compact form, we have

$$\mathbf{x} = \mathbf{A}\mathbf{d}, \tag{3.3}$$

where $\mathbf{x} = (x[0], \ldots, x[n], \ldots, x[N-1])^{\mathrm{T}}$ and

$$\mathbf{d} = \left((\mathbf{d}_0)^{\mathrm{T}}, \ldots, (\mathbf{d}_k)^{\mathrm{T}}, \ldots, (\mathbf{d}_{K-1})^{\mathrm{T}} \right)^{\mathrm{T}}$$

with $\mathbf{d}_k = (d_{k,0}, \ldots, d_{k,m}, \ldots, d_{k,M-1})^{\mathrm{T}}$. $\mathbf{A}$ denotes the $N \times N$ transmitter matrix

$$\mathbf{A} = (\mathbf{g}_{0,0} \quad \cdots \quad \mathbf{g}_{0,M-1} \quad \cdots \quad \mathbf{g}_{k,0} \quad \cdots$$
$$\mathbf{g}_{k,M-1} \quad \cdots \quad \mathbf{g}_{K-1,0} \quad \cdots \quad \mathbf{g}_{K-1,M-1}),$$

where $\mathbf{g}_{k,m} = (g_{k,m}[0], g_{k,m}[1], \ldots, g_{k,m}[N-1])^{\mathrm{T}}$.

From another perspective, (3.3) can be reformulated as [104]

$$\mathbf{x} = \mathbf{F}_N^{\mathrm{H}} \sum_{k=0}^{K-1} \mathbf{P}^{(k)} \mathbf{G}^{(S)} \mathbf{R}^{(S)} \mathbf{F}_M \mathbf{d}_k, \tag{3.4}$$

where $\mathbf{F}_M = \{f_{i,j}\}_{M \times M}$ is the discrete Fourier transform (DFT) matrix with $f_{i,j} = e^{-j2\pi \frac{ij}{M}}$ which transforms symbols $\mathbf{d}_k$ to the frequency domain. $\mathbf{R}^{(S)} = (\mathbf{I}_M, \ldots, \mathbf{I}_M)^{\mathrm{T}}$ is a repetition matrix which concatenates S identity matrices, corresponding to an S times upsampling in the time domain [105]. $\mathbf{G}^{(S)} = \mathrm{diag}\left(\mathbf{F}_{SM}\mathbf{g}^{(S)}\right)$ is the filtering matrix, where $\mathbf{F}_{SM}$ is a DFT matrix of size $SM \times SM$ and $\mathbf{g}^{(S)}$ is obtained by downsampling $\mathbf{g}$ by a factor of K/S. The function of the permutation matrix $\mathbf{P}^{(k)}$ is to shift signals to corresponding subcarriers [104].

$$\mathbf{P}^{(k)} = \mathbf{B}_\ell \begin{pmatrix} \mathbf{0}_{MS/2} & \mathbf{I}_{MS/2} & \mathbf{0}_{MS/2 \times (N-MS)} \\ \mathbf{I}_{MS/2} & \mathbf{0}_{MS/2} & \mathbf{0}_{MS/2 \times (N-MS)} \end{pmatrix}^{\mathrm{T}}, \tag{3.5}$$

where $\ell = kM - MS/2$. $\mathbf{B}_\ell$ is a circulant matrix and is given by

$$\mathbf{B}_\ell = \mathrm{circ}\left(\begin{bmatrix} \mathbf{0}_{\ell \mod N}^{\mathrm{T}}, & 1, & \mathbf{0}_{(N-\ell-1) \mod N}^{\mathrm{T}} \end{bmatrix}\right). \tag{3.6}$$

A CP is added to the whole GFDM block once the transmit samples are produced. Then the transmit signal passes over a multipath MIMO channel with N_{t} transmit antennas and N_{r} receive antennas. In the context of massive MIMO, hundreds of antennas might be placed at one side of the communication link, typically at the BS. It is assumed that the channel length L is shorter than the CP length. After the CP is removed, the received signal at receive antenna r is

$$\mathbf{y}_r = \sum_{t=1}^{N_{\mathrm{t}}} \mathbf{x}_t \circledast \mathbf{h}_{t,r} + \mathbf{n}_r, \tag{3.7}$$

where $\mathbf{x}_t$ denotes the transmit signal at the transmit antenna t and $\mathbf{n}_r$ denotes the additive white Gaussian noise (AWGN) at receive antenna r. $\mathbf{h}_{t,r}$ denotes the channel impulse response between transmit antenna t and receive antenna r, which is formulated as [106]

$$\mathbf{h}_{t,r} = \sqrt{\mathrm{diag}\left(\mathbf{p}_{t,r}\right)}\mathbf{a}_{t,r}, \tag{3.8}$$

where $\mathbf{p}_{t,r} \in \mathbb{R}^{L \times 1}$ is the normalized power delay profile (PDP), such that $\|\mathbf{p}_{t,r}\|_{\mathrm{F}} = 1$. $\mathbf{a}_{t,r} \in \mathbb{C}^{L \times 1}$ denotes a basic Rayleigh fading channel and its entries are complex Gaussian variables with zero mean and unit variance. In the frequency domain, we have

$$\mathbf{y}_r^{\mathrm{f}} = \sum_{t=1}^{N_{\mathrm{t}}} \mathbf{X}_t \mathbf{h}_{t,r}^{\mathrm{f}} + \mathbf{n}_r^{\mathrm{f}}, \tag{3.9}$$

where the superscript "f" indicates the related terms are in the frequency domain. $\mathbf{X}_t = \mathrm{diag}\left(\mathbf{F}_N \mathbf{x}_t\right)$ denotes the frequency-domain transmit signal and $\mathbf{h}_{t,r}^{\mathrm{f}} = \mathbf{F}_{N \times L} \mathbf{h}_{t,r}$ with $\mathbf{F}_{N \times L} \subset \mathbf{F}_N$ comprising the first L columns of $\mathbf{F}_N$. Moreover, $\mathbf{n}_r^{\mathrm{f}} = \mathbf{F}_N \mathbf{n}_r$.
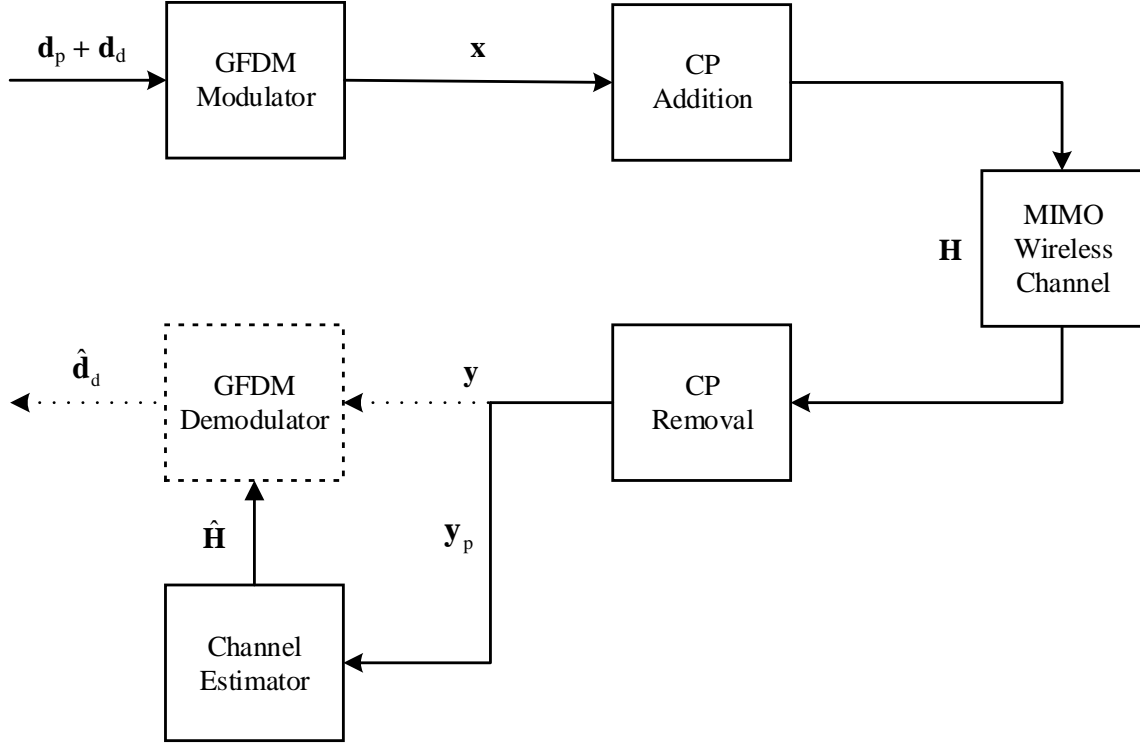
Figure 3.1: Illustration of the pilot transmission in the uplink.

3.2.2 Uplink Pilot Transmission

The uplink pilot transmission is depicted in Fig. 3.1. In order to perform channel estimation, we include the pilots $\mathbf{d}_p \in \mathbb{C}^{N \times 1}$ into the GFDM signals $\mathbf{x}$, in which user data $\mathbf{d}_d \in \mathbb{C}^{N \times 1}$ are also included. $\mathbf{d} = \mathbf{d}_p + \mathbf{d}_d$. $\mathbf{d}_p$ comprises pilot information only at pilot subcarriers with zeros at data subcarriers, while $\mathbf{d}_d$ comprises user data only at data subcarriers with zeros at pilot subcarriers. Therefore, $\mathbf{d}_p \circ \mathbf{d}_d = \mathbf{0}_N$, which implies there is no overlap between the pilot sequence and data. The GFDM signals are transmitted over a MIMO wireless channel $\mathbf{H}$ after the CP addition. Here, $\mathbf{H}$ is an equivalent channel matrix that consists of all the channel impulse responses. At the receiver, after removing the CP, the received pilot signals $\mathbf{y}_p$ are extracted from the hybrid signals $\mathbf{y}$ and then used by a channel estimator to obtain the channel estimates $\hat{\mathbf{H}}$. In practice, the demodulator can obtain the recovered user data $\hat{\mathbf{d}}_d$ based on $\hat{\mathbf{H}}$ once it is available.

For pilot patterns in [91] and [92], the GFDM data act as interference to the pilots at the receiver, which reduces the estimation accuracy. An interference-free pilot pattern has been proposed in [93] for GFDM systems. The transmit signal becomes

$$\mathbf{x} = \mathbf{F}_N^H \sum_{k=0}^{K-1} \mathbf{P}^{(k)} \mathbf{G}^{(S)} \mathbf{R}^{(S)} \left(\boldsymbol{\Gamma} \mathbf{d}_{p_k} + \mathbf{F}_M \mathbf{d}_{dk} \right), \tag{3.10}$$

where $\boldsymbol{\Gamma} = \mathbf{P}' \text{blkdiag} \left(\gamma \mathbf{I}_{N_t^{\text{UL}}}, \mathbf{F}_{M-N_t^{\text{UL}}} \right)$ with $\mathbf{P}'$ being a permutation matrix which allocates pilots at the

pilot subcarriers. The pilot energy is normalized by γ to one. It is worth noting that $\mathbf{F}_M \mathbf{d}_{\mathrm{d}k} = \mathbf{0}_{M \times 1}$ for the subcarrier k being a pilot subcarrier and $\boldsymbol{\Gamma} \mathbf{d}_{\mathrm{p}k} = \mathbf{0}_{M \times 1}$ for the subcarrier k being a data subcarrier. Then, the transmit signal at pilot subcarriers is

$$\mathbf{x}_{\mathrm{p}} = \mathbf{F}_N^{\mathrm{H}} \sum_{k=0}^{K-1} \mathbf{P}^{(k)} \mathbf{G}^{(S)} \mathbf{R}^{(S)} \boldsymbol{\Gamma} \mathbf{d}_{\mathrm{p}k}. \tag{3.11}$$

Pilots are placed at frequency bins such that there is no intercarrier interference. Each orthogonal subsymbol is reserved for a specific transmit antenna and consequently, an $N_{\mathrm{t}}^{\mathrm{UL}} \times N_{\mathrm{r}}^{\mathrm{UL}}$ MIMO channel can be considered in terms of $N_{\mathrm{t}}^{\mathrm{UL}} N_{\mathrm{r}}^{\mathrm{UL}}$ individual SISO channels, where the superscript "UL" means the corresponding parameter is for the uplink. This interference-free pilot pattern is illustrated in Fig. 3.2 for a 2×2 MIMO channel, where the pilot subcarrier spacing $\Delta k = 2$ and two frequency bins are reserved at pilot subcarriers for pilots with only one pilot being sent at each transmit antenna. The pilot
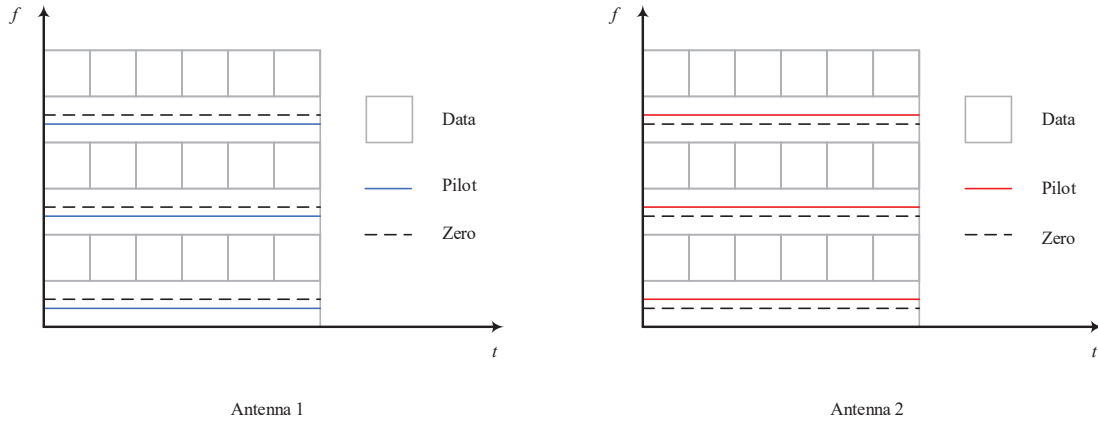

Figure 3.2: Illustration of the interference-free pilot pattern for a 2×2 MIMO channel.

signal received at receive antenna r is

$$\mathbf{y}_{\mathrm{p}r}^{\mathrm{f}} = \sum_{t=1}^{N_{\mathrm{t}}^{\mathrm{UL}}} \mathbf{X}_{\mathrm{p}t} \mathbf{h}_{\mathrm{p}t,r}^{\mathrm{f}} + \mathbf{n}_{\mathrm{p}r}^{\mathrm{f}}, \tag{3.12}$$

where $\mathbf{X}_{\mathrm{p}t} = \mathrm{diag}\left(\mathbf{F}_{N_{\mathrm{p}} \times N} \mathbf{x}_t\right)$, $\mathbf{h}_{\mathrm{p}t,r}^{\mathrm{f}} = \mathbf{F}_{N_{\mathrm{p}} \times L} \mathbf{h}_{t,r}$ and $\mathbf{n}_{\mathrm{p}r}^{\mathrm{f}} = \mathbf{F}_{N_{\mathrm{p}} \times N} \mathbf{n}_r$. N_{p} is the number of pilot samples and is given by $\lfloor MK/\Delta k \rfloor$. $\mathbf{F}_{N_{\mathrm{p}} \times N} \subset \mathbf{F}_N$ and $\mathbf{F}_{N_{\mathrm{p}} \times L} \subset \mathbf{F}_{N \times L}$ only contain the rows of $\mathbf{F}_N$ and $\mathbf{F}_{N \times L}$ that are associated to the pilots from transmit antenna t, respectively.

In order to include all the transmit-receive antenna pairs in one expression, let

$$\mathbf{Y}_{\mathrm{p}} = \left(\mathbf{y}_{\mathrm{p}1}^{\mathrm{f}}, \ldots, \mathbf{y}_{\mathrm{p}r}^{\mathrm{f}}, \ldots, \mathbf{y}_{\mathrm{p}N_{\mathrm{r}}^{\mathrm{UL}}}^{\mathrm{f}}\right),$$

$$\mathbf{X}_{\mathrm{p}} = \left(\mathbf{X}_{\mathrm{p}1}, \ldots, \mathbf{X}_{\mathrm{p}t}, \ldots, \mathbf{X}_{\mathrm{p}N_{\mathrm{t}}^{\mathrm{UL}}}\right),$$

$$F = I_{N_t^{UL}} \otimes F_{N_p \times L},$$

$$H = \begin{pmatrix} h_{1,1} & \cdots & h_{1,N_r^{UL}} \\ \vdots & \ddots & \vdots \\ h_{N_t^{UL},1} & \cdots & h_{N_t^{UL},N_r^{UL}} \end{pmatrix},$$

and

$$N = \left(n_{p1}^f, \ldots, n_{pr}^f, \ldots, n_{pN_r^{UL}}^f \right).$$

Then, we have

$$Y_p = X_p FH + N. \tag{3.13}$$

Based on the fact that $vec(ABC) = (C^T \otimes A) vec(B)$ [107], the vectorization of Y_p is

$$y_p = vec(Y_p) = Xh + n, \tag{3.14}$$

where $X = (I_{N_r^{UL}} \otimes X_p F)$, $h = vec(H)$ and $n = vec(N)$.

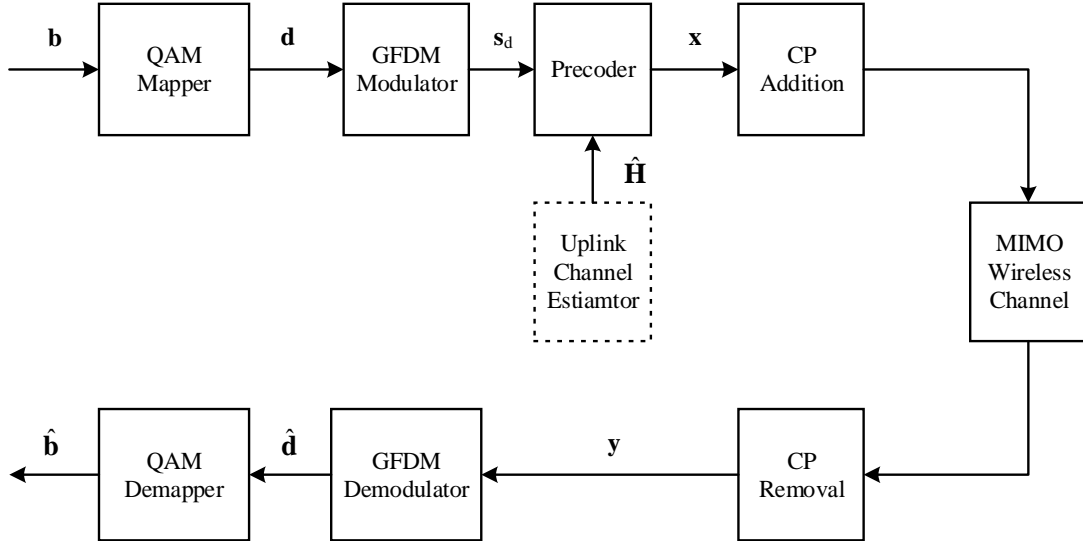### 3.2.3 Downlink Data Transmission with Precoding

Figure 3.3: Illustration of the downlink data transmission involving a precoder.

Fig. 3.3 illustrates the downlink data transmission which involves a precoder. We consider a single-cell massive MIMO system that operates in time-division duplex (TDD) mode, where the downlink channel

can be obtained from the transpose of the uplink channel. Precoding is performed at the base station to provide high-quality downlink transmission. There is one BS which is equipped with $N_{\mathrm{t}}^{\mathrm{DL}}$ antennas serving $N_{\mathrm{r}}^{\mathrm{DL}}$ user terminals in the cell, where the superscript "DL" means the corresponding parameter is for the downlink. The transmitted signal at BS is

$$\mathbf{x} = \mathbf{W}\mathbf{s}_{\mathrm{d}} = \sum_{n=1}^{N_{\mathrm{r}}^{\mathrm{DL}}} \mathbf{W}_n \mathbf{s}_n, \tag{3.15}$$

where $\mathbf{s}_{\mathrm{d}} = \left[\mathbf{s}_1^{\mathrm{T}}, \ldots, \mathbf{s}_{N_{\mathrm{r}}^{\mathrm{DL}}}^{\mathrm{T}}\right]^{\mathrm{T}}$ with $\mathbf{s}_n$ denoting the source signal for user terminal n. $\mathbf{W} = \left[\mathbf{W}_1, \ldots, \mathbf{W}_{N_{\mathrm{r}}^{\mathrm{DL}}}\right]$ denotes the precoding matrix with $\mathbf{W}_n$ being the subprecoding matrix for $\mathbf{s}_n$. The received signal vector at the rth user terminal is

$$\begin{aligned} \mathbf{y}_r &= \mathbf{H}_r^{\mathrm{H}}\mathbf{x} + \mathbf{n}_r \\ &= \mathbf{H}_r^{\mathrm{H}}\mathbf{W}\mathbf{s}_{\mathrm{d}} + \mathbf{n}_r \\ &= \mathbf{H}_r^{\mathrm{H}}\mathbf{W}_r\mathbf{s}_r + \sum_{n=1, n \neq r}^{N_{\mathrm{r}}^{\mathrm{DL}}} \mathbf{H}_r^{\mathrm{H}}\mathbf{W}_n\mathbf{s}_n + \mathbf{n}_r, \end{aligned} \tag{3.16}$$

where $\mathbf{n}_r$ denotes the AWGN at the user terminal r. $\mathbf{H}_r = \left[\mathbf{H}_{r,1}^{\mathrm{T}}, \ldots, \mathbf{H}_{r,N_{\mathrm{t}}^{\mathrm{DL}}}^{\mathrm{T}}\right]^{\mathrm{T}}$ with $\mathbf{H}_{r,t}$ being the circular convolution matrix between transmit antenna t and receive antenna r. The signal vector which involves the signals received by all user terminals is given by $\mathbf{y} = \left[\mathbf{y}_1^{\mathrm{T}}, \ldots, \mathbf{y}_{N_{\mathrm{r}}^{\mathrm{DL}}}^{\mathrm{T}}\right]^{\mathrm{T}}$.

The signal-to-interference-plus-noise ratio (SINR) at the user terminal r is given by

$$SINR_r = \frac{\mathrm{Tr}\left(\mathbf{H}_r^{\mathrm{H}}\mathbf{W}_r\mathbf{W}_r^{\mathrm{H}}\mathbf{H}_r\right)}{\mathrm{Tr}\left(\mathbf{H}_r^{\mathrm{H}}\mathbf{W}\mathbf{W}^{\mathrm{H}}\mathbf{H}_r\right) - \mathrm{Tr}\left(\mathbf{H}_r^{\mathrm{H}}\mathbf{W}_r\mathbf{W}_r^{\mathrm{H}}\mathbf{H}_r\right) + \sigma^2}, \tag{3.17}$$

where σ^2 denotes the noise variance. Then the achievable rate is

$$R_r = \log_2\left(1 + SINR_r\right). \tag{3.18}$$

3.3 Polynomial Expansion-Based MMSE Channel Estimation

3.3.1 MMSE Estimator

Bayesian MMSE estimators provide accurate estimations for MIMO channels when the channel statistics are known at the receiver. The Bayesian MMSE estimation calculates the coefficients of a linear filter and minimizes the MSE. Let $\hat{\mathbf{H}}$ be the estimate of $\mathbf{H}$. Thus, we have

$$\hat{\mathbf{h}}_{\mathrm{MMSE}} = \mathbf{C}_{\mathrm{h}}\mathbf{X}^{\mathrm{H}}\left(\mathbf{X}\mathbf{C}_{\mathrm{h}}\mathbf{X}^{\mathrm{H}} + \mathbf{C}_{\mathrm{n}}\right)^{-1}\mathbf{y}_{\mathrm{p}}, \tag{3.19}$$

where $\hat{\mathbf{h}}_{\mathrm{MMSE}} = \mathrm{vec}\left(\hat{\mathbf{H}}\right)$, $\mathbf{C}_{\mathrm{h}} \in \mathbb{C}^{LN_{\mathrm{t}}^{\mathrm{UL}}N_{\mathrm{r}}^{\mathrm{UL}} \times LN_{\mathrm{t}}^{\mathrm{UL}}N_{\mathrm{r}}^{\mathrm{UL}}}$ denotes the covariance matrix of $\mathbf{H}$ and $\mathbf{C}_{\mathrm{n}} \in \mathbb{C}^{N_{\mathrm{p}}N_{\mathrm{r}}^{\mathrm{UL}} \times N_{\mathrm{p}}N_{\mathrm{r}}^{\mathrm{UL}}}$ denotes the covariance matrix of $\mathbf{N}$. The MSE metric is

$$\begin{aligned} MSE_{\mathrm{MMSE}} &= \mathbb{E}\left\{\left\|\mathbf{H} - \hat{\mathbf{H}}\right\|_{\mathrm{F}}^2\right\} \\ &= \mathrm{Tr}\left(\mathbf{C}_{\mathrm{h}} - \mathbf{C}_{\mathrm{h}}\mathbf{X}^{\mathrm{H}}\left(\mathbf{X}\mathbf{C}_{\mathrm{h}}\mathbf{X}^{\mathrm{H}} + \mathbf{C}_{\mathrm{n}}\right)^{-1}\mathbf{X}\mathbf{C}_{\mathrm{h}}\right). \end{aligned} \tag{3.20}$$

We observe that there is a matrix inversion operation in the MMSE estimators which have the computational complexity $O\left(\left(N_p N_r^{UL}\right)^3\right)$. It is acceptable in conventional MIMO settings where N_r^{UL} are in general smaller than 10. However, in the context of massive MIMO, there might be hundreds of antennas at the BS. The computational complexity increases exponentially and will be an obstacle to a practical implementation. Therefore, it is necessary to find low-complexity estimators for massive MIMO channels.

3.3.2 Polynomial Expansion-Based MMSE Estimator

Polynomial expansion-based estimators [97] have been proposed to reduce the computational complexity in channel estimation for massive MIMO. In this section, we propose low-complexity MMSE channel estimators for massive MIMO-GFDM systems based on the concept of polynomial expansion.

Proposition 1: For any positive-definite Hermitian matrix $\mathbf{Z}$, we have [97]

$$
\begin{aligned}
\mathbf{Z}^{-1} &= \alpha \left(\mathbf{I} - (\mathbf{I} - \alpha \mathbf{Z})\right)^{-1} \\
&= \alpha \sum_{v=0}^{V} (\mathbf{I} - \alpha \mathbf{Z})^v + \mathbf{E},
\end{aligned}
\tag{3.21}
$$

where $0 < \alpha < 2/\max_n \lambda_n(\mathbf{Z})$ and the sum term on the right side is a V-degree polynomial expansion approximation. $\mathbf{E}$ is an error term which vanishes as $V \to \infty$.

A low-complexity PE-MMSE estimator is obtained by applying the approximation in Proposition 1 to (3.19), as follows

$$
\hat{\mathbf{h}}_{\text{PE-MMSE}} = \mathbf{C_h X^H} \alpha \sum_{v=0}^{V} \left(\mathbf{I} - \alpha \left(\mathbf{X C_h X^H} + \mathbf{C_n}\right)\right)^v \mathbf{y_p}.
\tag{3.22}
$$

α should be properly selected to satisfy the convergence condition in Proposition 1. In addition, the convergence speed of the polynomial expansion is determined by the value of α. For the consideration of complexity, α can be set to $2/\text{Tr}\left(\mathbf{X C_h X^H} + \mathbf{C_n}\right)$ [108]. In order to obtain the fastest asymptotic convergence speed, α can be set to $2/\left(\max_n \lambda_n\left(\mathbf{X C_h X^H} + \mathbf{C_n}\right) + \min_n \lambda_n\left(\mathbf{X C_h X^H} + \mathbf{C_n}\right)\right)$ [109]. The MSE of the PE-MMSE estimator is

$$
MSE_{\text{PE-MMSE}} = \text{Tr}\left(\mathbf{C_h} + \mathbf{C_h X^H A}_V \left(\mathbf{X C_h X^H} + \mathbf{C_n}\right) \mathbf{A}_V^H \mathbf{X C_h} - 2\mathbf{C_h X^H A}_V \mathbf{X C_h}\right),
\tag{3.23}
$$

where $\mathbf{A}_V = \sum_{v=0}^{V} \alpha \left(\mathbf{I} - \alpha \left(\mathbf{X C_h X^H} + \mathbf{C_n}\right)\right)^v$. For a given V and constant symbol energy, $MSE_{\text{PE-MMSE}}$ reaches its limit

$$
MSE_{\text{PE-MMSE}}^{\text{Limit}} = \text{Tr}\left(\mathbf{C_h} + \mathbf{C_h X^H} \tilde{\mathbf{A}}_V \mathbf{X C_h X^H} \tilde{\mathbf{A}}_V^H \mathbf{X C_h} - 2\mathbf{C_h X^H} \tilde{\mathbf{A}}_V \mathbf{X C_h}\right)
\tag{3.24}
$$

as $\mathbf{C_n} \to \mathbf{0}$, where $\tilde{\mathbf{A}}_V = \sum_{v=0}^{V} \tilde{\alpha} \left(\mathbf{I} - \tilde{\alpha} \mathbf{X C_h X^H}\right)^v$ and $\tilde{\alpha} = 2/\text{Tr}\left(\mathbf{X C_h X^H}\right)$. This implies that the MSE in (3.23) cannot be efficiently reduced by simply increasing the E_s/N_0, especially in the high E_s/N_0 region. Therefore, the limit in (3.24) can be used as a practical tool in predicting the estimators' performance in the high E_s/N_0 region.

The polynomial expansion-based estimator approaches the conventional MMSE estimator if V is sufficiently large and it suffers degradation in terms of the estimation performance for a finite V. Therefore, weighted V-degree polynomial expansions can be exploited to improve the approximation accuracy. To be specific, for a given V, different weights are assigned to the terms and then optimized in order to minimize the MSE metric. The weighted PE-MMSE (WPE-MMSE) estimator is formulated as [97]

$$\hat{\mathbf{h}}_{\text{WPE-MMSE}} = \mathbf{C}_h \mathbf{X}^H \sum_{v=0}^{V} w_v \alpha^{v+1} \left(\mathbf{X} \mathbf{C}_h \mathbf{X}^H + \mathbf{C}_n \right)^v \mathbf{y}_p, \tag{3.25}$$

where w_v is the $(v+1)^{\text{th}}$ element of the weight vector $\mathbf{w} = (w_0, w_1, \ldots, w_V)^{\text{T}}$. The optimal weights are obtained by minimizing the MSE with the help of the partial derivatives of the coefficients.

$$\mathbf{w}_{\text{opt}} = \mathbf{Q}^{-1} \mathbf{b}, \tag{3.26}$$

where the $(i, j)^{\text{th}}$ element of $\mathbf{Q} \in \mathbb{C}^{(V+1) \times (V+1)}$ and the ith element of $\mathbf{b} \in \mathbb{C}^{V+1}$ are

$$q_{i,j} = \alpha^{i+j} \text{Tr} \left(\mathbf{C}_h \mathbf{X}^H \left(\mathbf{X} \mathbf{C}_h \mathbf{X}^H + \mathbf{C}_n \right)^{i+j-1} \mathbf{X} \mathbf{C}_h \right)$$

and

$$b_i = \alpha^i \text{Tr} \left(\mathbf{C}_h \mathbf{X}^H \left(\mathbf{X} \mathbf{C}_h \mathbf{X}^H + \mathbf{C}_n \right)^{i-1} \mathbf{X} \mathbf{C}_h \right),$$

respectively.

With the optimal weights, the MSE of the WPE-MMSE estimator is given by

$$MSE_{\text{WPE-MMSE}} = \text{Tr} \left(\mathbf{C}_h \right) - \mathbf{b}^H \mathbf{Q}^{-1} \mathbf{b}. \tag{3.27}$$

Similarly, for a given V and constant symbol energy, $MSE_{\text{WPE-MMSE}}$ reaches its limit

$$MSE_{\text{WPE-MMSE}}^{\text{Limit}} = \text{Tr} \left(\mathbf{C}_h \right) - \tilde{\mathbf{b}}^H \tilde{\mathbf{Q}}^{-1} \tilde{\mathbf{b}} \tag{3.28}$$

as $\mathbf{C}_n \to \mathbf{0}$, where the $(i, j)^{\text{th}}$ element of $\tilde{\mathbf{Q}}$ and the ith element of $\tilde{\mathbf{b}}$ are defined as

$$\tilde{q}_{i,j} = \tilde{\alpha}^{i+j} \text{Tr} \left(\mathbf{C}_h \mathbf{X}^H \left(\mathbf{X} \mathbf{C}_h \mathbf{X}^H \right)^{i+j-1} \mathbf{X} \mathbf{C}_h \right)$$

and

$$\tilde{b}_i = \tilde{\alpha}^i \text{Tr} \left(\mathbf{C}_h \mathbf{X}^H \left(\mathbf{X} \mathbf{C}_h \mathbf{X}^H \right)^{i-1} \mathbf{X} \mathbf{C}_h \right),$$

respectively. The limit in (3.28) is also a useful tool which can predict the estimators' performance in the high E_s/N_0 region.

3.3.3 Cramér-Rao Lower Bound

The Cramér-Rao bound provides a lower bound on the variance of unbiased estimators and usually acts as a benchmark for evaluating different channel estimators. In this section, we derive the CRLB for the pilot-aided channel estimation model proposed in this chapter. According to (3.14), the received signal

follows a complex Gaussian distribution, i.e., $\mathbf{y}_p \sim N(\mathbf{Xh}, \mathbf{C}_n)$ and its probability density function (PDF) is formulated as

$$p(\mathbf{y}_p; \mathbf{h}) = \frac{1}{\pi^{N_p N_r^{\mathrm{UL}}} \det(\mathbf{C}_n)} e^{-\frac{1}{2}(\mathbf{y}_p - \mathbf{Xh})^H \mathbf{C}_n^{-1}(\mathbf{y}_p - \mathbf{Xh})}. \tag{3.29}$$

By conducting derivative, we have

$$\begin{aligned} \frac{\partial \ln p(\mathbf{y}_p; \mathbf{h})}{\partial \mathbf{h}^*} &= \mathbf{X}^H \mathbf{C}_n^{-1}(\mathbf{y}_p - \mathbf{Xh}) \\ &= \mathbf{X}^H \mathbf{C}_n^{-1} \mathbf{X}(\mathbf{X}^{-1} \mathbf{y}_p - \mathbf{h}), \end{aligned} \tag{3.30}$$

and then

$$\mathbb{E}\left[\frac{\partial \ln p(\mathbf{y}_p; \mathbf{h})}{\partial \mathbf{h}^*}\right] = \mathbf{0}, \quad \text{for all } \mathbf{h}. \tag{3.31}$$

Therefore, the "regularity" conditions [110] are satisfied. Let the estimates of $\mathbf{h}$ be denoted by $\hat{\mathbf{h}}$. Then, the CRLB on the variance matrix of any unbiased estimator is given by

$$\mathbf{C}_{\hat{\mathbf{h}}} = \mathbb{E}\left[(\hat{\mathbf{h}} - \mathbf{h})(\hat{\mathbf{h}} - \mathbf{h})^H\right] \geq J(\mathbf{h})^{-1}, \tag{3.32}$$

where $J(\mathbf{h})$ is the so-called Fisher information matrix [42] and the equality is attained if and only if

$$\frac{\partial \ln p(\mathbf{y}_p; \mathbf{h})}{\partial \mathbf{h}^*} = J(\mathbf{h})(\mathbf{f}(\mathbf{y}_p) - \mathbf{h}) \tag{3.33}$$

for some function $\mathbf{f}$ and matrix $\mathbf{J}$. Recall (3.30), the CRLB on the covariance matrix for a minimum variance unbiased (MVU) estimator is

$$\mathbf{C}_{\mathrm{CRLB}} = \left(\mathbf{X}^H \mathbf{C}_n^{-1} \mathbf{X}\right)^{-1}. \tag{3.34}$$

The MSE corresponding to the CRLB is defined as

$$MSE_{\mathrm{CRLB}} = \mathrm{Tr}\left(\left(\mathbf{X}^H \mathbf{C}_n^{-1} \mathbf{X}\right)^{-1}\right). \tag{3.35}$$

3.4 Polynomial Expansion-Based Precoding

With the CSI estimated in the previous section, we can generate precoding vectors using appropriate precoding algorithms to process the data before it is transmitted. This operation mitigates the effect of the channel on signals at the transmitting end and thus provides reliable data transmission.

For MMSE precoding,

$$\mathbf{W}_{\mathrm{MMSE}} = \xi \bar{\mathbf{H}}\left(\bar{\mathbf{H}}^H \bar{\mathbf{H}} + \mu \mathbf{I}_{N N_r^{\mathrm{DL}}}\right)^{-1}, \tag{3.36}$$

where ξ ensures that the power constraint is satisfied at the BS, i.e. $\mathrm{Tr}(\mathbf{WW}^H) = P$. $\bar{\mathbf{H}} = [\mathbf{H}_1, \ldots, \mathbf{H}_{N_r^{\mathrm{DL}}}]$. μ is a regularization factor. The MMSE precoder becomes a ZF precoder when $\mu \to 0$ and an MF precoder when $\mu \to \infty$. It is seen that there is a matrix inversion operation in (3.36). The direct computation of a matrix inverse incurs a cubic computational complexity which is expensive for massive MIMO applications.

The polynomial expansion technique can be used to reduce the computational complexity. Based on Proposition 1 in Section 3.3, the MMSE precoding matrix becomes

$$\mathbf{W}_{\text{PE-MMSE}} = \xi \bar{\mathbf{H}} \sum_{v=0}^{V} \alpha \left(\mathbf{I} - \alpha \left(\bar{\mathbf{H}}^{\text{H}} \bar{\mathbf{H}} + \mu \mathbf{I} \right) \right)^{v}, \tag{3.37}$$

where V denotes the polynomial degree. In order to obtain the fastest asymptotic convergence speed of the polynomial expansion, let $\alpha = 2 / \left(\max_n \lambda_n \left(\bar{\mathbf{H}}^{\text{H}} \bar{\mathbf{H}} + \mu \mathbf{I}_{NN_{\text{r}}^{\text{DL}}} \right) + \min_n \lambda_n \left(\bar{\mathbf{H}}^{\text{H}} \bar{\mathbf{H}} + \mu \mathbf{I}_{NN_{\text{r}}^{\text{DL}}} \right) \right)$ [109].

3.5   Complexity Analysis

The MMSE estimator and the MMSE precoder have computational complexity of $O\left(\left(N_{\text{p}} N_{\text{r}}^{\text{UL}} \right)^{3} \right)$ and $O\left(\left(NN_{\text{r}}^{\text{DL}} \right)^{3} \right)$, respectively, due to the direct computation of the matrix inverse.

For the convenience of description and without loss of generality, let $\mathbf{V} = \mathbf{I} - \alpha \left(\mathbf{X} \mathbf{C}_{\text{h}} \mathbf{X}^{\text{H}} + \mathbf{C}_{\text{n}} \right)$. The polynomial can be computed in a recursive way, as follows

$$\sum_{v=0}^{V} \mathbf{V}^{v} \mathbf{y}_{\text{p}} = \mathbf{y}_{\text{p}} + \mathbf{V} \left(\mathbf{y}_{\text{p}} + \mathbf{V} \left(\mathbf{y}_{\text{p}} + \mathbf{V} \left(\ldots \right) \right) \right). \tag{3.38}$$

There are only matrix-vector multiplications in (3.38) and thus, its computational complexity is $O\left(V \left(N_{\text{p}} N_{\text{r}}^{\text{UL}} \right)^{2} \right)$. Therefore, the computational complexity of the PE-MMSE estimator in (3.22) is also $O\left(V \left(N_{\text{p}} N_{\text{r}}^{\text{UL}} \right)^{2} \right)$ and is reduced, compared with an MMSE estimator, whenever $V < N_{\text{p}} N_{\text{r}}^{\text{UL}}$. Similarly, the computational complexity of of the PE-MMSE precoder becomes $O\left(V \left(NN_{\text{r}}^{\text{DL}} \right)^{2} \right)$. The PE-MMSE precoder, therefore, provides a reduced computational complexity when $V < NN_{\text{r}}^{\text{DL}}$. In addition, the value of V can be properly selected to balance the performance against the complexity.

For the WPE-MMSE estimator, the computational complexity is $O\left(\left(N_{\text{p}} N_{\text{r}}^{\text{UL}} \right)^{3} \right)$ because there are matrix-matrix multiplications and matrix inverse in finding the optimal weights. However, by using a low-complexity algorithm for computing the optimal weights, the complexity can be reduced to $O\left(V \left(N_{\text{p}} N_{\text{r}}^{\text{UL}} \right)^{2} + V^{3} \right)$. We refer readers to [97] for more details on this low-complexity algorithm.

3.6   Numerical Results

The derived channel estimators are verified by computer simulations using MATLAB. The related parameters are summarized in Table 3.1. No interfering cells are assumed. For all transmit-receive antenna pairs, the PDP vector is first exponentially generated according to $\mathbf{p}_{t,r} = e^{-\tau/10}$ with $\tau = (0, 1, \ldots, L-1)^{\text{T}}$, and then is normalized. Pilots are placed at the subcarriers with spacing Δk from the first one. The permutation matrix $\mathbf{P}' = \mathbf{I}_M$, which means that pilots are placed at the first N_{t}^{UL} subsymbols of the pilot subcarriers. The MSE is normalized by the trace of the channel covariance matrix, i.e., $MSE / \text{Tr} \left(\mathbf{C}_{\text{h}} \right)$.

The MSE of different estimators is shown in Fig. 3.4 for different values of E_s / N_0. E_s denotes the average energy of the symbols in a 16-QAM constellation and N_0 denotes the variance of the AWGN.

Table 3.1: Simulation Parameters

Parameter	Symbol	Value
No. of BS antennas	N_r^{UL} or N_t^{DL}	112
No. of single-antenna terminals	N_t^{UL} or N_r^{DL}	8
Prototype filter	-	RC
Roll-off factor of the RC filter	ω	0.5
No. of subcarriers	K	96
No. of subsymbols	M	11
No. of channel taps	L_{ch}	5
Pilot subcarrier spacing	Δk	$[4, 6, 8, 12, 16]$
Pilot sequence	-	1st root Zadoff-Chu [111]
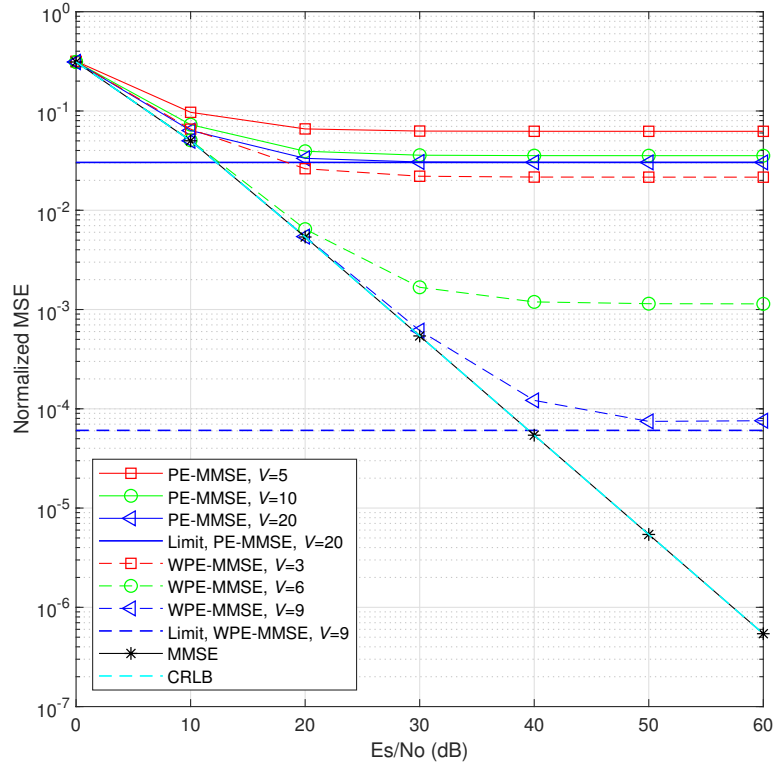
Figure 3.4: MSE of the PE-MMSE and WPE-MMSE estimators for different E_s/N_0.

$\Delta k = 8$ and the polynomial degree V is set to 5, 10 and 20 for PE-MMSE and set to 3, 6 and 9 for WPE-MMSE. The MSE of an MMSE estimator and the CRLB are also shown for comparison. It is shown that the MMSE estimator coincides with the CRLB in terms of MSE. We can see that the MSE decreases with the increase of E_s/N_0. Both the PE-MMSE and WPE-MMSE estimators reach their limits in terms of MSE as E_s/N_0 increases, showing flatness in the high E_s/N_0 region. The WPE-MMSE estimator reaches a lower MSE level compared to the PE-MMSE estimator because of the introduction and optimization of weights. The PE-MMSE and WPE-MMSE estimators show larger MSE values than the MMSE estimator, which is the cost of the polynomial expansion approximation with a finite V. The MSE gaps between polynomial expansion-based estimators and the MMSE estimator decrease with an increasing V. With a sufficiently large V, the polynomial expansion-based estimators will approach the MMSE estimator at the cost of complexity. With $V = 9$, the WPE-MMSE estimator matches the MMSE estimator well in the low E_s/N_0 region.
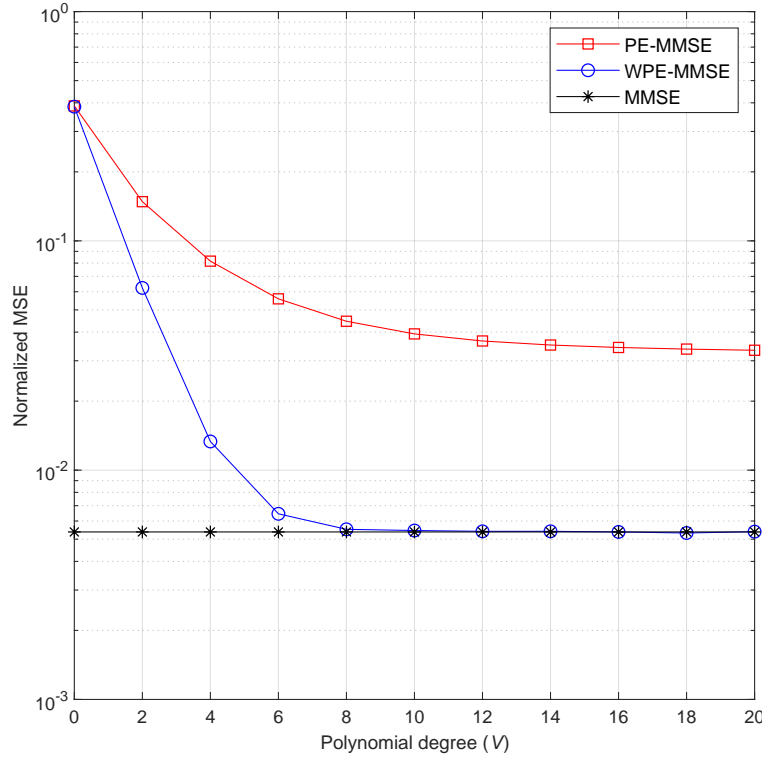

Figure 3.5: MSE of the PE-MMSE and WPE-MMSE estimators for different polynomial degrees at $E_s/N_0 = 20$ dB.

Fig. 3.5 clearly shows the impact of the polynomial degree on the MSE of the PE-MMSE and WPE-MMSE estimators. $\Delta k = 8$ and E_s/N_0 is set to 20 dB. As before, the MSE of an MMSE estimator is also shown for comparison. We can see that the MSE of the PE-MMSE and WPE-MMSE estimators decreases as V increases, but there is a noticeable difference between them. The WPE-MMSE estimator shows a faster speed approaching the MMSE estimator compared to the PE-MMSE estimator and for $V \geq 8$ (this value may vary for different parameter settings), the MSE of the WPE-MMSE estimator is

very close to that of the MMSE estimator so that the difference can be ignored.
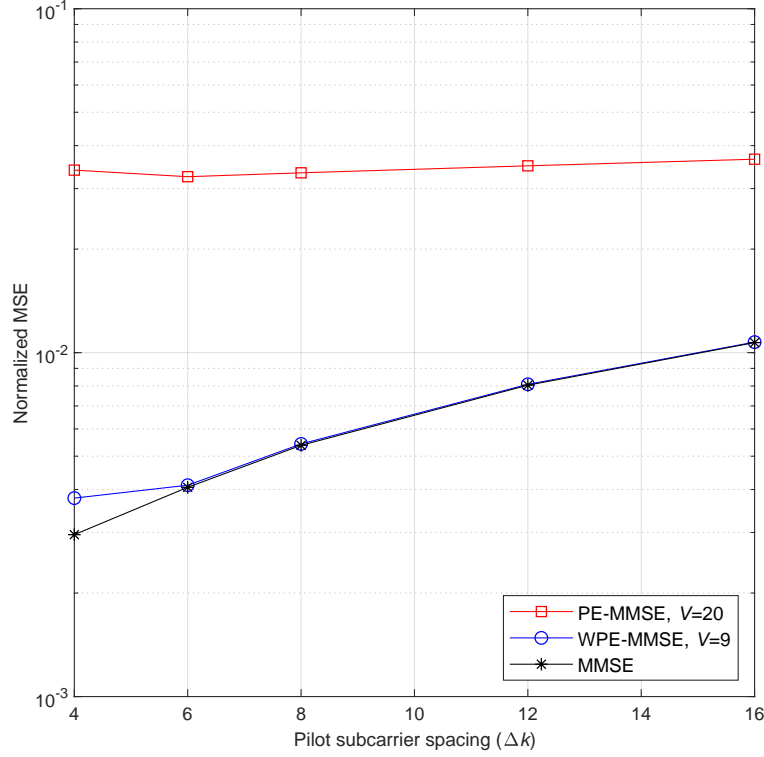

Figure 3.6: The influence of the pilot subcarrier spacing on the MSE of the estimators at $E_s/N_0 = 20$ dB.

The influence of the pilot subcarrier spacing Δk on the MSE of the MMSE, PE-MMSE and WPE-MMSE estimators is shown in Fig. 3.6. V is set to 20 and 9 for the PE-MMSE and WPE-MMSE estimator, respectively, and E_s/N_0 is set to 20 dB. We confine Δk to values by which K is divisible. We can see that the MSE of all the channel estimators increases with the increase of Δk. This increase is expected because increasing Δk means decreasing the number of pilot symbols. The WPE-MMSE estimator shows nearly the same MSE as the MMSE estimator while the PE-MMSE estimator exhibits higher values. One of the findings worth noting here is that the difference between the PE-MMSE estimator and the MMSE estimator decreases as Δk increases. This implies that the PE-MMSE estimator can be a good alternative to the MMSE estimator in a case where only limited amount of pilots are allowed.

Let the average achievable rate $R = \left(1/N_{\mathrm{r}}^{\mathrm{DL}}\right) \sum_{r=1}^{N_{\mathrm{r}}^{\mathrm{DL}}} R_r$. The average achievable rates of the MMSE and PE-MMSE precoders for various transmit power-to-noise ratio ($TPNR$) are shown in Fig. 3.7. $TPNR = P / \left(N_{\mathrm{r}}^{\mathrm{DL}} \sigma^2\right)$. The channel matrices in (3.36) and (3.37) are obtained from the WPE-MMSE channel estimation in the uplink with $E_s/N_0 = 30$ dB and $V = 9$. The average achievable rate of the PE-MMSE precoder inceases to approach that of the MMSE precoder as the polynomial degree increases. We can see that with $V = 30$, the PE-MMSE precoder shows an average achievable rate very close to that of the MMSE precoder, especially in the low $TPNR$ region.
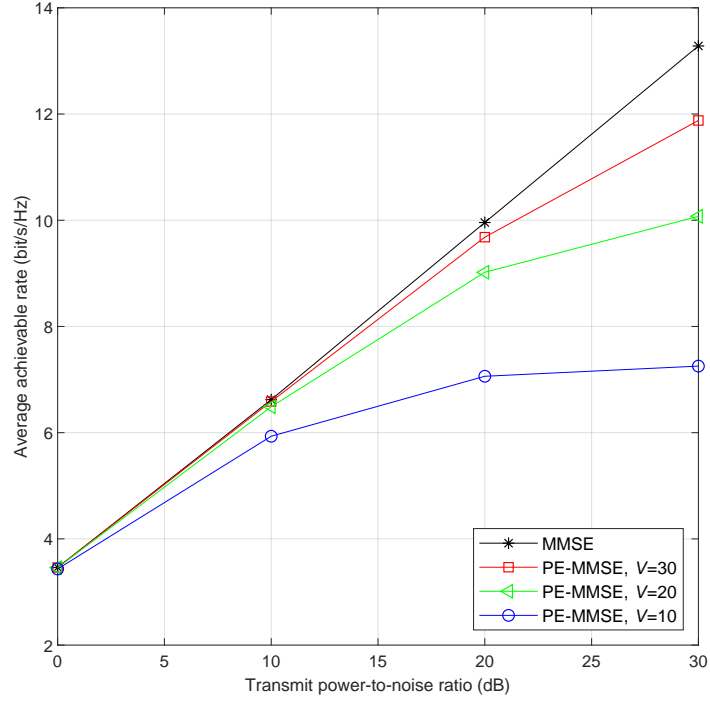
Figure 3.7: Average achievable rates of the MMSE and PE-MMSE precoders for varying $TPNR$ with $V = 10$, 20 and 30.
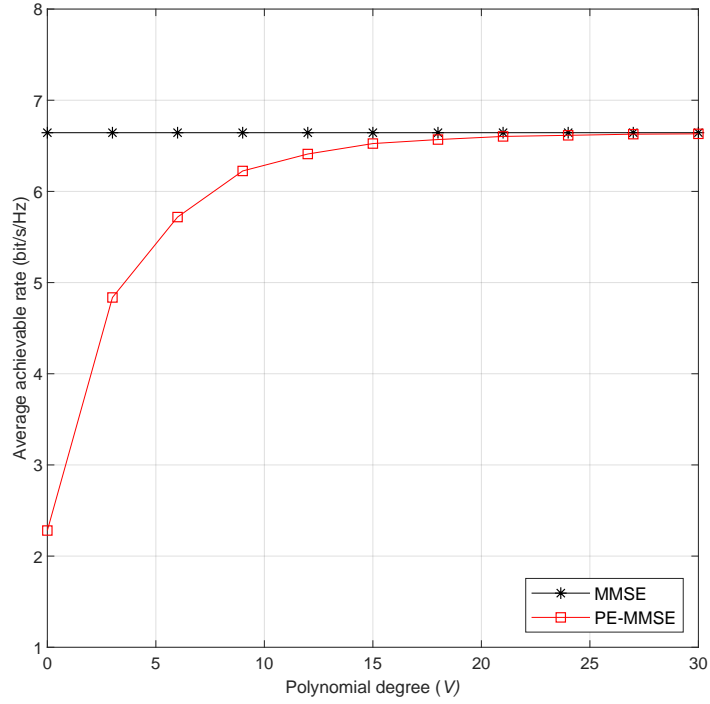

Figure 3.8: Average achievable rates of the MMSE and PE-MMSE precoders for different polynomial degrees with $TPNR = 10$ dB.

The impact of the polynomial degree on the average achievable rate is shown in Fig. 3.8, where $TPNR$ is set to 10 dB. It can be seen that the average achievable rate of the PE-MMSE precoder increases rapidly with an increasing polynomial degree. The PE-MMSE precoder matches the MMSE precoder when $V \geq 20$.
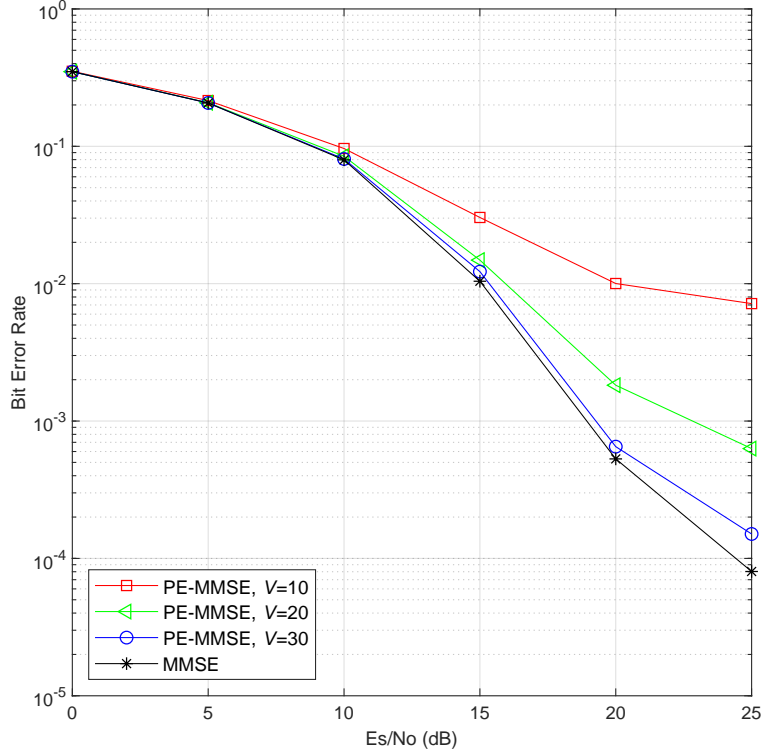

Figure 3.9: Bit error rate performance of the downlink transmission for different E_s/N_0.

Finally, the bit error rate (BER) performances in the downlink are shown in Figs. 3.9 and 3.10. The polynomial degee of the WPE-MMSE estimator and E_s/N_0 in the uplink are set to 9 and 30 dB, respectively. For Fig. 3.9, $\Delta k = 8$ and $V = 10$, 20 and 30. We can see that the BER of the PE-MMSE precoder approaches that of the MMSE precoder as V increases and with $V = 30$, they match well, especially in the low E_s/N_0 region. For Fig. 3.10, $V = 30$ and $E_s/N_0 = 20$ dB. It is seen that the downlink BER of MMSE and PE-MMSE precoders increases with the increase of Δk. This is due to the fact that with a larger Δk, less pilots are sent and then, less pilot information can be used by the channel estimators, which increases the channel estimation errors. The increased errors in channel estimation give rise to the larger BER in Fig. 3.10.

3.7   Conclusion

Massive MIMO-GFDM systems can provide flexible waveforms and high spatial resolution at the same time. Accurate acquisition of CSI is the key to recovering the signals at the receiver. Interference-free pilot patterns can be used to eliminate the influence of the non-orthogonality in GFDM on the received
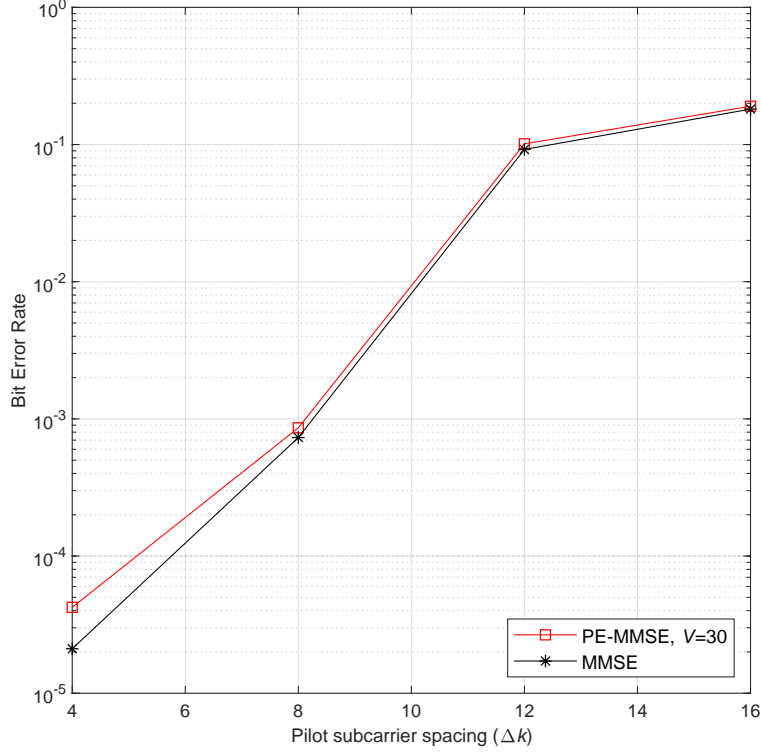
Figure 3.10: Influence of the pilot subcarrier spacing on the downlink bit error rate at $E_s/N_0 = 20$ dB.

pilots. MMSE estimators are optimal when the channel statistics are known at the receiver. At the same time, the MMSE precoder is a good trade-off between the ZF and MRT precoders. However, the cubic computational complexity in the MMSE algorithm is unaffordable for massive MIMO applications. In this chapter, we proposed polynomial expansion-based MMSE estimators and precoders for massive MIMO-GFDM systems, which reduce the cubic computational complexity to square order through approximating the matrix inverse with a finite V-degree matrix polynomial. In practice, V can be appropriately selected to balance complexity against estimation performance. Limits on the MSE of the proposed estimators are derived to analyze their performance in the high E_s/N_0 region. Numerical results show that, for the proposed channel estimators and precoders, near-optimal performance can be obtained in the low E_s/N_0 region with small polynomial degrees.

Chapter 4

Performance Analysis of LDPC Coded GFDM systems

Résumé

Ce chapitre analyse les performances de probabilités d'erreurs des codes de contrôle de parité à faible densité (LDPC) utilisés avec des systèmes de multiplexage généralisé par répartition en fréquence (GFDM) dans des canaux de Rayleigh et des canaux à bruit blanc gaussien additif (AWGN). Les expressions du rapport de vraisemblance logarithmique (LLR) initiale utilisées dans l'algorithme de somme de produits (SPA) pour les décodeurs sont d'abord dérivées pour le modèle du système présenté dans ce chapitre. Basé sur le seuil de décodage du système, le taux d'erreurs de trame (FER) dans la région de bas E_b/N_0 est estimé en modélisant les variations de canal à l'aide du taux d'erreurs sur les bits (BER) observé. Ensuite, une borne inférieure basée sur les ensembles absorbants est proposée pour le FER lorsque des décodeurs SPA quantifiés sont utilisés. Pour des canaux à bruit blanc gaussien additif, la borne inférieure peut agir comme un estimé du FER dans la région du plancher d'erreurs si l'ensemble absorbant est dominant et que sa multiplicité est connue. Pour les canaux de Rayleigh, la borne inférieure peut encore être utilisé pour estimer la performance du FER pour les codes sélectionnés. L'approche d'estimation pour le FER dans la région de bas E_b/N_0 et la borne inférieure du FER dans la région de haut E_b/N_0 peuvent être utilisées comme outils pratiques pour évaluer différentes conceptions de systèmes basés sur le GFDM en termes de performance de probabilité d'erreur. La méthode de quantification a un impact important sur les performances du FER et du BER. Des codes LDPC construits aléatoirement et basés sur des tableaux sont utilisés pour obtenir des résultats numériques qui démontrent les performances du système et la précision des estimations proposées pour le FER.

Abstract

This chapter analyzes the error probability performance of low-density parity-check (LDPC) coded generalized frequency division multiplexing (GFDM) systems over Rayleigh fading and additive white

Gaussian noise (AWGN) channels. The initial log-likelihood ratio (LLR) expressions used in the sum-product algorithm (SPA) decoder are first derived for the system model presented in this chapter. Based on the decoding threshold of the system, the frame error rate (FER) in the low E_b/N_0 region is estimated by modeling the channel variations using the observed bit error rate (BER). Then, a lower bound based on the absorbing sets is proposed for the FER when quantized SPA decoders are used. For AWGN channels, the lower bound can act as an estimate of the FER in the error-floor region if the absorbing set is dominant and its multiplicity is known. For Rayleigh channels, the lower bound can still be used to estimate the FER performance of selected codes. The estimation approach for the FER in the low E_b/N_0 region and the lower bound on the FER in the high E_b/N_0 region can be used as practical tools for evaluating different designs of GFDM-based systems in terms of the error probability performance. The quantization scheme has an important impact on the FER and BER performances. Randomly constructed and array-based LDPC codes are used to obtain numerical results that show the system performance and the accuracy of the proposed FER estimations.

4.1 Introduction

Generalized frequency division multiplexing (GFDM) [10], [1] is a block-processing based multi-carrier modulation (MCM) scheme which can generate flexible waveforms. The filtering operation introduced in GFDM reduces the out-of-band (OOB) radiation, which enables dynamic spectrum allocation in cognitive radio (CR) systems [67]. However, the subcarriers are no longer orthogonal due to the filtering operation. Therefore, GFDM systems also suffer inter-carrier interference (ICI) in addition to the inter-symbol interference (ISI). The number of subcarriers and subsymbols can be easily adjusted to meet the low-latency requirement for the Tactile Internet [69]. In GFDM, a cyclic prefix (CP) and a cyclic suffix (CS) are assigned to an entire block instead of each symbol, which increases the spectral efficiency. This can relax the synchronization requirements in machine type communications (MTC) [68]. Due to its flexibilty, GFDM can be an important candidate waveform for beyond 5G systems.

Low-density parity-check (LDPC) codes are capacity-approaching linear block error correction codes, which were initially discovered by Gallager in 1962 [8]. The advantages of LDPC codes include simple description, great flexibility, high throughput and low decoding complexity. In addition, LDPC decoding can also provide low latency and more parallelization. Due to these advantages, LDPC codes have been adopted in several standards, including worldwide interoperability for microwave access (WiMAX), digital video broadcasting (DVB-S2), and the enhanced mobile broadband (eMBB) scenario in 5G. Despite excellent asymptotic performance, when decoded by a practical message-passing decoder, finite-length LDPC codes exhibit error floors where the slope of the error probability curve decreases. The low E_b/N_0 region where the error probability falls quickly is called the waterfall region. The asymptotic performance of LDPC codes can be efficiently analyzed by density evolution [112] when assuming the code's block length goes to infinity. However, density evolution cannot provide accurate analysis for finite-length codes. The finite-length analysis of LDPC codes over the binary

erasure channel (BEC) was presented in [113] using a combinatorial method. The performance of LDPC codes in the waterfall region, over the BEC, was proved to follow a scaling law for iterative decoders [114]. An efficient estimation method based on the decoding threshold and observed bit error rate (BER) was proposed for the finite-length performance of LDPC codes over symmetric channels [115]. In addition, the performance analysis of finite-length LDPC codes over asymmetric memoryless channels was presented in [116]. Some error-prone structures in the Tanner graphs [47] of LDPC codes, such as near-codewords [117], trapping sets [118], and absorbing sets [119], have been identified to contribute to the error floor. An importance sampling based method was proposed to estimate the frame error rate (FER) of LDPC codes with the knowledge of trapping sets [118]. Error floor estimates based on absorbing sets were proposed for array-based codes in [120]. A code-independent lower bound has been proposed for LDPC codes, which was based on the dominant absorbing sets and can be used to estimate the error floor performance [121]. Monte-Carlo simulations has been widely used to estimate the error probabilities of communications systems. However, for LDPC coded systems, such simulations take too much time to obtain reliable numerical results for very low error probabilities. Therefore, developing accurate estimators or performance bounds is of great practical importance due to the fact that they usually need less time and thus, provide quick analyses for systems of interest.

In this chapter, we analyze the error probability performances of LDPC coded GFDM systems over Rayleigh and additive white Gaussian noise (AWGN) channels. To the best of our knowledge, this work is the first to report such analyses, although there have been some simulation results for LDPC coded GFDM systems [122], [123]. We first derive the initial log-likelihood ratio (LLR) that is the input of the SPA decoders for our system model. Then, we estimate the FER in the low E_b/N_0 region by using the observed BER to interpret the channel variations. The decoding threshold obtained from the Gaussian approximation method is used along with the observed BER to derive the FER estimation. Finally, a lower bound is derived for the FER based on absorbing sets while assuming the use of quantized SPA decoders. In developing the lower bound, we take into consideration the dynamics of the LLRs input to the check nodes connected to the absorbing set from outside the set. Saturation in the LLR values of the quantized SPA decoder is assumed to make the decoding more practical. In the case of a Rayleigh channel, we make a conjecture to facilitate the probability computation. We then apply our methods to randomly constructed and array-based LDPC codes and analyze the error performance of LDPC coded systems. Numerical results show that the introduction of LDPC codes into GFDM systems can substantially improve the error probability performance and the FER estimation and lower bound are valid.

The rest of the chapter is organized as follows. Necessary concepts, such as absorbing sets, SPA decoding and Gaussian approximation, are introduced in Section 4.2. A system model for the LDPC coded GFDM system is provided in Section 4.3. In Section 4.4, we first derive the initial LLR that is required for the SPA decoding and then estimate the FER in the low E_b/N_0 region. In addition, we propose a lower bound on the FER for the LDPC coded GFDM system with quantized SPA decoders. Numerical results are presented in Section 4.5. Finally, Section 4.6 concludes the chapter.
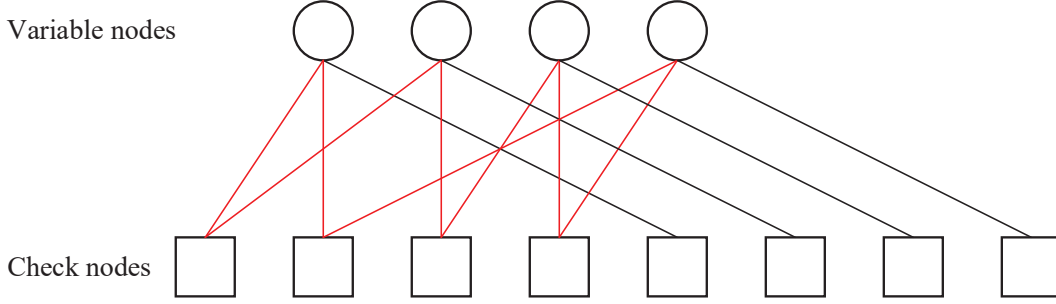
Figure 4.1: Illustration of a $(4,4)$ absorbing set.

Notation: Scalars are denoted by italic lower/upper case letters. Vectors are denoted by bold lower case letters. Matrices are denoted by bold upper case letters. $a_{i,j}$ refers to the $(i,j)^{\text{th}}$ element of matrix **A**. $(\cdot)^{\text{T}}$ and $(\cdot)^{\text{H}}$ denote the matrix transpose and conjugate transpose, respectively. $|\cdot|$ denotes the norm of a number or the cardinality of a set. $\lfloor x \rfloor$ rounds x down to the largest integer that is not greater than x. $\lceil x \rceil$ rounds x up to the smallest integer that is not less than x. $\Re[\cdot]$ and $\Im[\cdot]$ denote the real and imaginary parts of a complex number, respectively.

4.2 Preliminaries

4.2.1 Absorbing Sets

For a Tanner graph of an LDPC code, let sets $\mathbb{V} = \{v_1, v_2, \ldots, v_n\}$ and $\mathbb{C} = \{c_1, c_2, \ldots, c_m\}$ denote the variable nodes (VNs) and check nodes (CNs), respectively. $\mathbb{A} = \{v_1, v_2, \ldots, v_a\}$ is a subset of $\mathbb{V}$, whose cardinality is $|\mathbb{A}| = a$. The sets of the CNs that are connected to the VNs in $\mathbb{A}$ with even and odd degrees are denoted by $\mathbb{E}(\mathbb{A})$ and $\mathbb{O}(\mathbb{A})$, respectively. Let $\mathbb{C}(\mathbb{A}) = \mathbb{E}(\mathbb{A}) \cup \mathbb{O}(\mathbb{A})$. $|\mathbb{O}(\mathbb{A})| = b$ and $|\mathbb{C}(\mathbb{A})| = \theta$. $\mathbb{A}$ is a so-called (a,b) *trapping set* [118]. $\mathbb{A}$ is an (a,b) *absorbing set* [119] if each node in $\mathbb{A}$ is connected to fewer nodes in $\mathbb{O}(\mathbb{A})$ than $\mathbb{E}(\mathbb{A})$. Fig. 4.1, as an example, shows the bipartite graph of a $(4,4)$ absorbing set. The edges highlighted in red show a shortest cycle in the absorbing set, whose length is defined as the *girth*.

4.2.2 Sum-Product Algorithm

Let L_j denotes the jth initial LLR. $\mathbb{N}(i)$ and $\mathbb{N}(j)$ denote the sets of neighbors to the CN i and VN j, respectively. The Gallager Sum–Product Algorithm [124] is summarized as follows:

1. **Initialization:**

$$L_j = L(v_j|y_j) = \log\left(\frac{\Pr(v_j = 0|y_j)}{\Pr(v_j = 1|y_j)}\right), \tag{4.1}$$

where v_j and y_j denote the jth transmitted and j^{th} received bits, respectively. For all i,j for which $h_{i,j} = 1$, set $L_{j\rightarrow i} = L_j$. $h_{i,j}$ is an entry of the parity-check matrix $\mathbf{H}_{\text{PC}}$.

2. **CN updates:** Compute outgoing CN messages $L_{i \to j}$ and then transmit to VNs.

$$L_{i \to j} = \prod_{j' \in \mathbb{N}(i) - \{j\}} \gamma_{j'i} \cdot \Phi \left(\sum_{j' \in \mathbb{N}(i) - \{j\}} \Phi \left(\eta_{j'i} \right) \right), \tag{4.2}$$

where $\gamma_{ji} = \text{sign} \left(L_{j \to i} \right)$ and $\eta_{ji} = \left| L_{j \to i} \right|$ such that $L_{j \to i} = \gamma_{ji} \eta_{ji}$, and

$$\Phi(x) = \log \left(\frac{e^x + 1}{e^x - 1} \right).$$

3. **VN updates:** Compute outgoing VN messages $L_{j \to i}$ and then transmit to CNs.

$$L_{j \to i} = L_j + \sum_{i' \in \mathbb{N}(j) - \{i\}} L_{i' \to j}. \tag{4.3}$$

4. **LLR sum:**

$$L_j^{\text{total}} = L_j + \sum_{i \in \mathbb{N}(j)} L_{i \to j}, \tag{4.4}$$

for all j.

5. **Stopping criteria:** Make decisions based on

$$\hat{v}_j = \begin{cases} 1, & \text{if } L_j^{\text{total}} < 0; \\ 0, & \text{else,} \end{cases} \tag{4.5}$$

to obtain the estimated codeword $\hat{\mathbf{v}}$. If $\hat{\mathbf{v}} \mathbf{H}_{\text{PC}}^{\text{T}} = \mathbf{0}$ or the maximum number of iterations is reached, then stop; else, repeat steps 2 - 5.

4.2.3 Gaussian Approximation

For AWGN channels, a Gaussian approximation can be used to simplify the computation of density evolution by approximating the probability density functions (PDFs) of messages with Gaussian probability densities. Let $m^{(v)}$ be the outgoing message of a variable node in the Tanner graph and $m^{(c)}$ be a check node. Assume the messages satisfy the consistency condition with respect to their PDFs. If a normal distribution $X \sim \mathcal{N} \left(\mu, \sigma^2 \right)$ satisfies the consistency condition, then $\sigma^2 = 2\mu$, i.e. $X \sim \mathcal{N}(\mu, 2\mu)$. Therefore, in this case, the distribution can be characterized only by a single parameter, i.e. the mean. Let d_v and d_c denote the variable-node degree and check-node degree, respectively. For message updates at variables,

$$m_l^{(v)} = m_0 + \sum_{j=1}^{d_v - 1} m_{j,l-1}^{(c)}. \tag{4.6}$$

By taking expectation, the means are

$$\begin{aligned} \mu_l^{(v)} &= \mu_0 + \sum_{j=1}^{d_v - 1} \mu_{j,l-1}^{(c)} \\ &= \mu_0 + (d_v - 1) \mu_{l-1}^{(c)}. \end{aligned} \tag{4.7}$$

58

For message updates at check nodes,

$$\mu_l^{(c)} = \phi^{-1}\left(1 - \left(1 - \phi\left(\mu_0 + (d_v - 1)\mu_{l-1}^{(c)}\right)\right)^{d_c - 1}\right),\tag{4.8}$$

where

$$\phi(x) = \begin{cases} 1 - \frac{1}{\sqrt{4\pi x}}\int_{\mathbb{R}}\tanh\frac{x}{2}e^{-\frac{(u-x)^2}{4x}}\,du, & \text{if } x > 0; \\ 1, & \text{if } x = 0. \end{cases}\tag{4.9}$$

After l decoding iterations, we can get the mean of the messages for variable nodes. Then the PDF can be found for a variable node message based on its mean. According to the desicion criterion used in the SPA algorithm, the probability of bit error is

$$p_e = \Pr\left(m_l^{(v)} < 0\right).\tag{4.10}$$

By predefining an error probability level, e.g. 10^{-10}, the decoding threshold can be determined.

4.2.4 Uniform Quantization

Let $Q_{\beta_1.\beta_2}$ denote a uniform quantizer which represents a fixed-point number with β_1 bits for representing the integer part and β_2 bits for representing the fractional part of the number. An additional bit is used to represent the sign. Therefore, the total number of bits of the quantizer is $\beta = \beta_1 + \beta_2 + 1$. The minimum and maximum values that the quantizer can provide are $q_{\min} = -2^{\beta_1}$ and $q_{\max} = 2^{\beta_1} - 2^{-\beta_2}$, respectively. The step size is $\Delta = 2^{-\beta_2}$. For a real number x, its quantized representation can be given by

$$Q(x) = \begin{cases} \lfloor x/\Delta + 0.5 \rfloor \cdot \Delta, & \text{if } x \geq \Delta/2; \\ \lceil x/\Delta - 0.5 \rceil \cdot \Delta, & \text{if } x \leq -\Delta/2; \\ 0, & \text{otherwise,} \end{cases}\tag{4.11}$$

and be bounded by $q_{\min}$ and $q_{\max}$, i.e.,

$$Q(x) = \begin{cases} q_{\min}, & \text{if } Q(x) < q_{\min}; \\ q_{\max}, & \text{if } Q(x) > q_{\max}. \end{cases}\tag{4.12}$$

4.3 System Description

We consider an LDPC coded GFDM system that is depicted in Fig. 4.2. The B-bit-long information vector $\mathbf{b}$ is processed by an LDPC encoder to produce a C-bit-long codeword vector $\mathbf{v}$ with a coding rate $r = B/C$. $\mathbf{v}$ is mapped to the symbols in a constellation to generate the symbol vector $\mathbf{d}$. The number of information bits required to generate one symbol is $\mu = \log_2 J$ given that J is the size of the constellaion. The BPSK mapping is used in the chapter. Then the symbols are modulated by a GFDM modulator to produce a signal vector $\mathbf{x}$. There are K subcarriers and M subsymbols in each GFDM
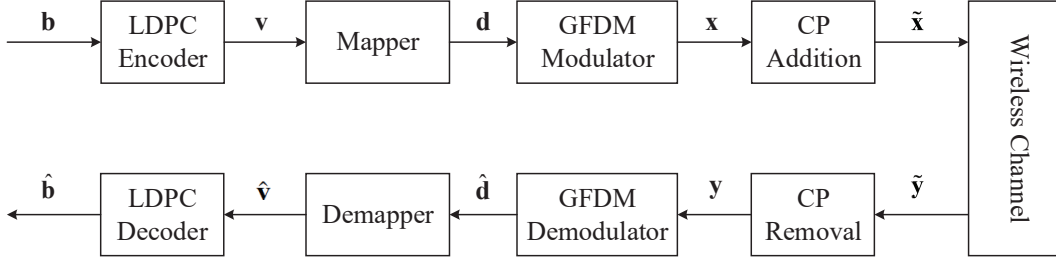
Figure 4.2: Transceiver diagram of an LDPC coded GFDM system.

block, leading to a total of $N = K \times M$ symbols. $\mathbf{x} = (x[0], x[1], \ldots, x[N-1])^{\mathrm{T}}$ and

$$x[n] = \sum_{k=0}^{K-1} \sum_{m=0}^{M-1} g_{k,m}[n] d_{k,m}, \quad n = 0, \ldots, N-1, \tag{4.13}$$

where $d_{k,m}$ denotes the symbol transmitted on the kth subcarrier and in the mth time slot of the GFDM block [1] and $g_{k,m}[n]$ is obtained by the time and frequency shift of a prototype filter $g[n]$,

$$g_{k,m}[n] = g[(n - mK) \bmod N] e^{j2\pi \frac{k}{K} n}. \tag{4.14}$$

Equation (4.13) can be rewritten to obtain a compact expression, as follows

$$\mathbf{x} = \mathbf{A}\mathbf{d}, \tag{4.15}$$

where

$$\mathbf{d} = \left(\mathbf{d}_0^{\mathrm{T}}, \mathbf{d}_1^{\mathrm{T}}, \ldots, \mathbf{d}_{K-1}^{\mathrm{T}}\right)^{\mathrm{T}} \tag{4.16}$$

with $\mathbf{d}_k = (d_{k,0}, d_{k,1}, \ldots, d_{k,M-1})^{\mathrm{T}}$. $\mathbf{A}$ is the $N \times N$ transmitter matrix, denoted by

$$\mathbf{A} = \begin{pmatrix} \mathbf{g}_{0,0} & \mathbf{g}_{0,1} & \cdots & \mathbf{g}_{0,M-1} & \mathbf{g}_{1,0} & \cdots & \mathbf{g}_{K-1,M-1} \end{pmatrix}, \tag{4.17}$$

where $\mathbf{g}_{k,m} = (g_{k,m}[0], g_{k,m}[1], \ldots, g_{k,m}[N-1])^{\mathrm{T}}$. A CP is added to the signal $\mathbf{x}$ to generate $\tilde{\mathbf{x}}$. Then, the signal $\tilde{\mathbf{x}}$ goes through a wireless channel and $\tilde{\mathbf{y}}$ is the received signal. By assuming perfect synchroniztion, the received signal after CP removal is given by

$$\mathbf{y} = \mathbf{H}\mathbf{x} + \mathbf{n}, \tag{4.18}$$

where $\mathbf{H}$ denotes a circulant convolution matrix of size $N \times N$, which is an equivalent channel matrix. A special case is the AWGN channel ($\mathbf{H} = \mathbf{I}$), where the received signal becomes $\mathbf{y} = \mathbf{x} + \mathbf{n}$. $\mathbf{n}$ denotes the complex-valued AWGN, i.e. $\mathbf{n} \sim \mathcal{CN}(0, N_0\mathbf{I})$, where N_0 is the noise power density. GFDM is a filtered MCM scheme and particularly useful for fading channels in combating narrowband interference and multipath fading. Therefore, theoretical analyses of GFDM systems over fading channels are of practical importance. In this chapter, both Rayleigh and AWGN channels are used. The channel matrix

H in the case of Rayleigh fading has the following structure.

$$\mathbf{H} = \begin{bmatrix} h_1 & 0 & \cdots & 0 & h_{N_{\text{ch}}} & \cdots & h_2 \\ h_2 & h_1 & & \vdots & 0 & \ddots & \vdots \\ \vdots & h_2 & \ddots & 0 & \vdots & & h_{N_{\text{ch}}} \\ h_{N_{\text{ch}}} & \vdots & & h_1 & 0 & & 0 \\ 0 & h_{N_{\text{ch}}} & & h_2 & h_1 & & \vdots \\ \vdots & 0 & \ddots & \vdots & h_2 & \ddots & 0 \\ 0 & \vdots & \cdots & h_{N_{\text{ch}}} & \vdots & \cdots & h_1 \end{bmatrix}, \tag{4.19}$$

where $(h_1, h_2, \ldots, h_{N_{\text{ch}}})^{\text{T}} = \mathbf{h}$ denote the channel impulse response of length N_{ch}. The entries of $\mathbf{h}$ are independent and identically distributed (i.i.d.) complex Gaussian random variables with zero mean and unit variance (0.5 for real or imaginary parts). By assuming that perfect channel state information is available at the receiver, a zero-forcing (ZF) equalizer can be used to yield

$$\begin{aligned} \mathbf{z} &= \mathbf{H}^{-1}\mathbf{y} \\ &= \mathbf{x} + \mathbf{H}^{-1}\mathbf{n}. \end{aligned} \tag{4.20}$$

The euqalization takes place following the CP removal and is unnecessary for AWGN channels. Then, we obtain the recovered symbols $\hat{\mathbf{d}}$ by demodulating $\mathbf{y}$, as follows

$$\hat{\mathbf{d}} = \mathbf{B}\mathbf{z}, \tag{4.21}$$

where $\mathbf{B}$ is the receiver matrix and when the ZF criterion is used, $\mathbf{B} = \mathbf{A}^{-1}$.

$\hat{\mathbf{d}}$ is transformed to the estimated codeword vector $\hat{\mathbf{v}}$ after SPA decoding and BPSK demapping. Finally, $\hat{\mathbf{v}}$ is converted to the recovered information vector $\hat{\mathbf{b}}$.

4.4 Performance Analysis of Error Probability for LDPC Coded GFDM Systems

4.4.1 Initial LLR Calculation

For the purpose of simplicity, we consider a BPSK mapper. The jth bit of the codeword $\mathbf{v}$ and the jth element in the symbol vector $\mathbf{d}$ are denoted by v_j and d_j, respectively. For BPSK, $v_j = 0$ is mapped to $d_j = +1$ and $v_j = 1$ is mapped to $d_j = -1$. Recalling (4.15) and following (4.20) and (4.21), we have

$$\begin{aligned} \hat{\mathbf{d}} &= \mathbf{d} + (\mathbf{HA})^{-1}\mathbf{n} \\ &= \mathbf{d} + \mathbf{E}\mathbf{n} \\ &= \mathbf{d} + \tilde{\mathbf{n}}, \end{aligned} \tag{4.22}$$

where $\tilde{\mathbf{n}}$ is directly defined in the equation.

The received symbol corresponding to d_j is given by

$$\hat{d}_j = d_j + \tilde{n}_j. \tag{4.23}$$

$\tilde{n}_j$ is formulated as

$$\tilde{n}_j = \mathbf{e}_j \mathbf{n}$$
$$= \sum_{l=1}^{N} e_{j,l} n_l, \tag{4.24}$$

where $\mathbf{e}_j$ is the jth row of the matrix $\mathbf{E}$. $e_{j,l}$ and n_l, $l = 1, 2, \ldots, N$, are the lth elements in $\mathbf{e}_j$ and $\mathbf{n}$, respectively. Both $k_{j,l}$ and n_l are complex numbers. It is obvious from (4.24) that $\tilde{n}_j$ is a linear combination of all n_l's. Recall that $\mathbf{n}$ is a complex Gaussian random vector and each entry n_l has a mean zero and variance N_0. Then, the real and imaginary parts of n_l have Gaussian distributions with mean zero and variance σ^2, i.e. $\Re[n_l] \sim \mathcal{N}(0, \sigma^2)$ and $\Im[n_l] \sim \mathcal{N}(0, \sigma^2)$, where $\sigma^2 = N_0/2$. Therefore, $\tilde{n}_j$ is also a Gaussian random variable, i.e. $\Re[\tilde{n}_j] \sim \mathcal{N}\left(0, \tilde{\sigma}_j^2\right)$ and $\Im[\tilde{n}_j] \sim \mathcal{N}\left(0, \tilde{\sigma}_j^2\right)$, whose variance is given by

$$\tilde{\sigma}_j^2 = \sum_{l=1}^{N} |e_{j,l}|^2 \sigma^2$$
$$= \mathbf{e}_j \mathbf{e}_j^{\mathsf{H}} \sigma^2. \tag{4.25}$$

The received symbol $\hat{d}_j$ also has a Gaussian distribution with mean ± 1 (corresponding to $d_j = \pm 1$) and variance $2\tilde{\sigma}_j^2$. Thus, the PDF of $\Re\left[\hat{d}_j\right]$ can be formulated as

$$f(\hat{d}_j) = \frac{1}{\sqrt{2\pi}\tilde{\sigma}_j} e^{-\frac{\left(\hat{d}_j \mp 1\right)^2}{2\tilde{\sigma}_j^2}} \tag{4.26}$$

for $d_j = \pm 1$.

$\Re\left[\hat{d}_j\right]$ is used to generate the prior LLR. Under the assumption that $\Pr(v_j = 0) = \Pr(v_j = 1)$, the initial LLR in (4.1) becomes

$$
\begin{aligned}
L_j &= \log\left(\frac{\Pr\left(v_j = 0 \mid \Re\left[\hat{d}_j\right]\right)}{\Pr\left(v_j = 1 \mid \Re\left[\hat{d}_j\right]\right)}\right) \\
&= \log\left(\frac{\Pr\left(\Re\left[\hat{d}_j\right] \mid v_j = 0\right)}{\Pr\left(\Re\left[\hat{d}_j\right] \mid v_j = 1\right)}\right) \\
&= \frac{2\Re\left[\hat{d}_j\right]}{\tilde{\sigma}_j^2}.
\end{aligned} \tag{4.27}
$$

Because $\Re\left[\hat{d}_j\right]$ has a normal distribution, L_j is also normally distributed. Without loss of generality, we assume all-zero codewords are transmitted. Therefore, we have

$$L_j \sim \mathcal{N}\left(\frac{2}{\tilde{\sigma}_j^2}, \frac{4}{\tilde{\sigma}_j^2}\right). \tag{4.28}$$

4.4.2 FER Estimation in the Low E_b/N_0 Region

In this section, we estimate the low-E_b/N_0-region FER performance of LDPC coded GFDM systems over AWGN channels.

The decoding threshold is defined as

$$\alpha^* = \sup\{\alpha : \lim_{l\to\infty} \int_{-\infty}^{0} p_l^{(v)}(\tau)\, d\tau = 0\}. \tag{4.29}$$

α is the channel parameter. For the AWGN channel, $\alpha = \sigma$ and the corresponding decoding threshold is denoted by σ^*. $\tilde{\sigma}^* = \sqrt{\mathbf{e}_j \mathbf{e}_j^{\mathrm{H}}}\sigma^*$. In order to determine the decoding threshold, we use the Gaussian approximation approach in Section 4.2.3 with the following approximation to $\phi(x)$ [125] to facilitate computation,

$$\phi(x) \approx \begin{cases} e^{-0.4527x^{0.864}+0.0218}, & \text{if } 0 \le x \le 10; \\ \sqrt{\frac{\pi}{x}}e^{-\frac{x}{4}}\left(1 - \frac{\pi^2}{8x}\right), & \text{if } x > 10. \end{cases} \tag{4.30}$$

A bit is received in error if the LLR L from the channel is smaller than 0. The probability of error is

$$\begin{aligned} p_0 &= \int_{-\infty}^{0} f_L(l)\, dl \\ &= Q_{\mathrm{n}}\left(\frac{1}{\tilde{\sigma}}\right), \end{aligned} \tag{4.31}$$

where $f_L(l)$ denotes the PDF of L and $Q_{\mathrm{n}}(x) = \frac{1}{\sqrt{2\pi}}\int_{0}^{\infty} e^{-\frac{\tau^2}{2}}\, d\tau$ is the tail distribution function of the standard normal distribution. Therefore, the probability of error at σ^* is $p^* = Q_{\mathrm{n}}\left(\frac{1}{\tilde{\sigma}^*}\right)$.

The observed BER, P_{obs}, is the ratio of the number of bit errors to the code length in the transmission of a codeword. P_{obs} is a random variable and used to model the error rate of the channel. Let N_{e} denote the number of bit errors. Thus, $P_{\mathrm{obs}} = N_{\mathrm{e}}/N$. The probability mass function (PMF) of N_{e} is

$$f_{N_{\mathrm{e}}}(\tilde{\sigma}, N, N_{\mathrm{e}}) = \binom{N}{N_{\mathrm{e}}} p_0^{N_{\mathrm{e}}} (1 - p_0)^{N - N_{\mathrm{e}}}, \tag{4.32}$$

where N_{e} is an integer and $0 \le N_{\mathrm{e}} \le N$. For sufficiently large N, the above discrete binomial distribution, $\mathcal{B}(N, p_0)$, can be approximated by a continuous Gaussian distribution whose mean is equal to Np_0 and variance is equal to $Np_0(1 - p_0)$, i.e. $Y \sim \mathcal{N}(Np_0, Np_0(1 - p_0))$. The continuity correction is applied in order to improve the approximation accuracy.

$$\Pr(N_{\mathrm{e}} > n_{\mathrm{e}}) = \Pr(N_{\mathrm{e}} \ge n_{\mathrm{e}} + 1) \approx \Pr(Y > n_{\mathrm{e}} + 0.5). \tag{4.33}$$

A frame error occurs when $P_{\mathrm{obs}} > p^*$ by assuming that a decoding failure results from an observed channel worse than the decoding threshold [115]. Therefore, the FER can be estimated as follows

$$FER = \Pr(P_{\mathrm{obs}} > p^*) = \Pr(N_{\mathrm{e}} > Np^*) \approx \Pr(Y > Np^* + 0.5), \tag{4.34}$$

where *FER* is the average frame error rate. Recall that Y is normally distributed, thus

$$\Pr\left(Y > Np^* + 0.5\right) = Q_n\left(\frac{Np^* + 0.5 - Np_0}{\sqrt{Np_0\left(1 - p_0\right)}}\right). \tag{4.35}$$

In this section, decoding thresholds are computed using Gaussian approximation and all the bits are assumed to have the same error probability p_0. Therefore, the above estimation method is only valid for AWGN channels.

4.4.3 Lower Bound on the FER in the High E_b/N_0 Region With Quantized Decoders

In this section, we propose lower bounds on the FER of LDPC coded GFDM systems with quantized decoders, which apply to both AWGN and Rayleigh channels.

$\xi\left(\mathbb{A}\right)$ is defined as the event that there are still bit errors in absorbing set $\mathbb{A}$ after T decoding iterations operating on the absorbing set. The probability of error can be given by [121]

$$\begin{aligned}\Pr\left(\xi\left(\mathbb{A}\right)\right) = \\ \sum_i\sum_k\Pr\left(\xi\left(\mathbb{A}\right)|\mathbf{s} = \mathbf{x}_i, \mathbf{U} = \mathbf{W}_k\right)\cdot\Pr\left(\mathbf{s} = \mathbf{x}_i, \mathbf{U} = \mathbf{W}_k\right),\end{aligned} \tag{4.36}$$

where $\mathbf{s}$ denotes the quantized channel LLR vector corresponding to the VNs in $\mathbb{A}$ and $\mathbf{x}_i$ is the realization of $\mathbf{s}$. Matrix $\mathbf{U}$ denotes the LLRs input to CNs in $\mathbb{C}\left(\mathbb{A}\right)$ from VNs outside $\mathbb{A}$ and $\mathbf{W}_k$ is the realization of $\mathbf{U}$. The set of all possible $\mathbf{W}_k$ is denoted by W. $\Pr\left(\xi\left(\mathbb{A}\right)|\mathbf{s} = \mathbf{x}_i, \mathbf{U} = \mathbf{W}_k\right)$ takes only values 0 or 1 according to whether the $\mathbf{x}_i$ is correctly decoded or not. By assuming that $\mathbf{s}$ and $\mathbf{U}$ are independent we have

$$\Pr\left(\xi\left(\mathbb{A}\right)\right) = \sum_{(\mathbf{x}_i, \mathbf{W}_k)\in\psi}\Pr\left(\mathbf{s} = \mathbf{x}_i\right)\cdot\Pr\left(\mathbf{U} = \mathbf{W}_k\right), \tag{4.37}$$

where $\psi = \{(\mathbf{x}_i, \mathbf{W}_k)|\Pr\left(\xi\left(\mathbb{A}\right)|\mathbf{s} = \mathbf{x}_i, \mathbf{U} = \mathbf{W}_k\right) = 1\}$. Then a lower bound on the error probability of the absorbing set can be found as follows [121]

$$\Pr\left(\xi\left(\mathbb{A}\right)\right) \geq \lambda\left(\mathbb{A}\right) \triangleq \sum_{\mathbf{x}_i\in\Psi(W)}\Pr\left(\mathbf{s} = \mathbf{x}_i\right), \tag{4.38}$$

where $\Psi\left(W\right)$ is the set of $\mathbf{x}_i$ that cannot be correctly decoded for all $\mathbf{W}_k$, i.e. $\Psi\left(W\right) = \{\mathbf{x}_i|\left(\mathbf{x}_i, \mathbf{W}_k\right)\in\psi, \forall\,\mathbf{W}_k\in W\}$. $\Pr\left(\mathbf{s} = \mathbf{x}_i\right)$ can be obtained according to (4.28) with the quantization taken into account.

Note that in the case of an AWGN channel, all $\tilde{\sigma}_j^2$'s in (4.28) are equal. However, when a Rayleigh channel is used, the values of $\tilde{\sigma}_j^2$'s are different for different variable nodes, implying that their LLRs have different Gaussian distributions. In this case, the exact position of the absorbing set needs to be known to compute $\Pr\left(\mathbf{s} = \mathbf{x}_i\right)$ for Rayleigh channels. In order to simpify the computation of $\Pr\left(\mathbf{s} = \mathbf{x}_i\right)$ over Rayleigh channels, we propose to use an average value $\tilde{\sigma}_a^2$ to replace all $\tilde{\sigma}_j^2$ to obtain the same distribution for all LLRs. The ideal way for finding this average is to theoretically determine the dstributions of $\tilde{\sigma}_j^2$ and then, compute the expexted value. Recall (4.25), then we find that $\tilde{\sigma}_j^2$ is

determined by $e_{j,l}$, which are the entries of $\mathbf{E}$. $\mathbf{E} = (\mathbf{HA})^{-1} = \mathbf{A}^{-1}\mathbf{H}^{-1}$, where $\mathbf{A}$ is deterministic and $\mathbf{H}$ is a circulant matrix whose nonzero entries are normally distributed.

$$\mathbf{H} = \mathbf{F\Lambda F}^{*}, \tag{4.39}$$

where $\mathbf{F}$ is the matrix composed of the eigenvectors, whose entries are fixed. $\mathbf{\Lambda} = \text{diag}(\lambda_k)$ with λ_k being the eigenvalue. The inverse of $\mathbf{H}$ can be given by

$$\mathbf{H}^{-1} = \mathbf{F\Lambda}^{-1}\mathbf{F}^{*}. \tag{4.40}$$

Therefore, the distribution of $\mathbf{H}^{-1}$ can be found when the distribution of $\mathbf{\Lambda}^{-1}$ is known. λ_k is normally distributed. However, unfortunately, the distribution of its reciprocal, $1/\lambda_k$, cannot be found. Thus, theoretically determining the distribution of $\mathbf{E}$ through $\mathbf{H}^{-1}$ is impossible. In this case, a practical approach is to use Monte-Carlo simulations to find the statistics of interest. Given that in (4.25), σ is fixed, we only have to find the average value of $\mathbf{e}_j\mathbf{e}_j^{\text{H}}$. In the case of an AWGN channel, $\mathbf{e}_i\mathbf{e}_i^{\text{H}} = \mathbf{e}_j\mathbf{e}_j^{\text{H}} = \omega_{\text{A}}, \forall\, i,j \in [1,N]$. For Rayleigh channels, let $\omega_j = \mathbf{e}_j\mathbf{e}_j^{\text{H}}$ and $\bar{\omega} = \frac{1}{N}\sum_{j=1}^{N}\omega_j$. After carefully examining the values of $\bar{\omega}$ that are averaged over 10^5 realizations of $\mathbf{H}$, we obtain the following conjecture regarding the relationship among $\bar{\omega}$, ω_{A} and N_{ch}.

$$\bar{\omega} = \frac{2\omega_{\text{A}}^3}{\omega_{\text{A}}^{N_{\text{ch}}/3} - \omega_{\text{A}}^{-N_{\text{ch}}/3}}. \tag{4.41}$$

Fig. 4.3 shows an example of the conjecture for GFDM systems over Rayleigh channels, whose block size is $K \times M = 48 \times 21$. This conjecture enables one to determine $\bar{\omega}$ and compute $\Pr(\mathbf{s} = \mathbf{x}_i)$ quickly.

Define $\varepsilon(\mathbb{V})$ as the event that there are still bit errors in set $\mathbb{V}$ after decoding the bits on the full code graph for T iterations. The FER is formulated as $FER = \Pr(\varepsilon(\mathbb{V}))$. Let $\varepsilon(\mathbb{A})$ denote the event that there are still bit errors in A after T decoding iterations operating on the full code graph. Then we have

$$FER \geq \Pr(\varepsilon(\mathbb{A})). \tag{4.42}$$

If there are N independent isomorphic absorbing sets $\mathbb{A}$, by assuming that all of them have the same probability of error we have

$$\begin{aligned} FER &\geq \Pr\left(\bigcup_{i=1}^{N}\varepsilon(\mathbb{A}_i)\right) \\ &\geq N\Pr(\varepsilon(\mathbb{A})) - \binom{N}{2}(\Pr(\varepsilon(\mathbb{A})))^2, \end{aligned} \tag{4.43}$$

where $\mathbb{A}_i$ denotes the ith absorbing set. The value of $\Pr(\varepsilon(\mathbb{A}))$ is generally quite small in the high E_b/N_0 region so that $\Pr(\varepsilon(\mathbb{A})) \gg (\Pr(\varepsilon(\mathbb{A})))^2$. Thus, we further have
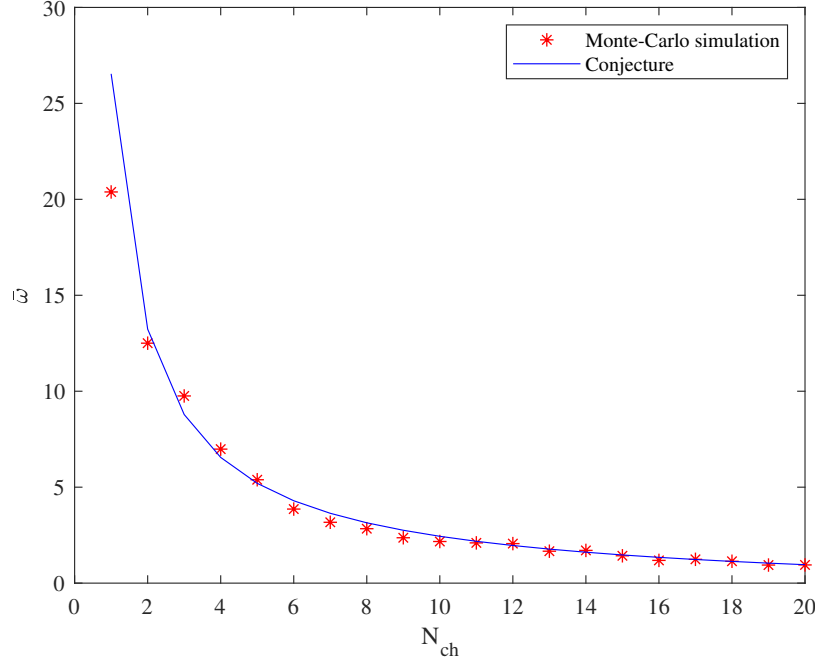
$$FER \geq N\Pr(\varepsilon(\mathbb{A})). \tag{4.44}$$

Figure 4.3: Conjecture on $\bar{\omega}$ for GFDM systems with $K = 48$ and $M = 21$.

Based on the following inequality [121]

$$\Pr(\varepsilon(\mathbb{A})) \geq \lambda(\mathbb{A}), \tag{4.45}$$

a lower bound on the FER can be given by

$$FER \geq N\lambda(\mathbb{A}). \tag{4.46}$$

Determining the set $\Psi(W)$ is required in order to calculate $\lambda(\mathbb{A})$. However, determinig $\Psi(W)$ requires to go over all $\mathbf{W}_k$ for each $\mathbf{x}_i$, which is time-consuming for practical quantization schemes and iteration numbers. Therefore, approximating $\Psi(W)$ using a small number of $\mathbf{W}_k$ is necessary. In order to select reasonable $\mathbf{W}_k$, we examine the dynamics of the external LLR values input to $\mathbb{C}(\mathbb{A})$ from VNs outside $\mathbb{A}$. Such dynamics can be found via running the SPA decoder on the full code graph for T iterations and averaging over sufficient frame transmissions. As an example, Fig. 4.4 shows the dynamics of the external LLRs at $E_b/N_0 = 5$ dB for a $(3,3)$ absorbing set of the randomly constructed $(3,6)$ code of length 1008 [126]. Note that the LLR values increase quickly to a saturation level $\Phi(0)$ [127] within a small number of iterations. The value of $\Phi(0)$ influences the decoding performance. As reported in [127], greater values of $\Phi(0)$ result in lower error floors but the performance in the waterfall region deteriorates at the same time. $\Phi(0) = 4.25$ in our setup. Now let $\mathbf{W}_{\text{sat}} = \{\Phi(0)\}_{\theta \times p}$ with all its entries having value $\Phi(0)$. Therefore, by assuming that the VNs in the absorbing set are more likely to be decoded correctly when the external LLRs have the maximum values than when they have smaller values, a straightforward method to identify $\Psi(W)$ is to just examine the set $\mathbf{W}_{\text{sat}}$ to find the incorrectly
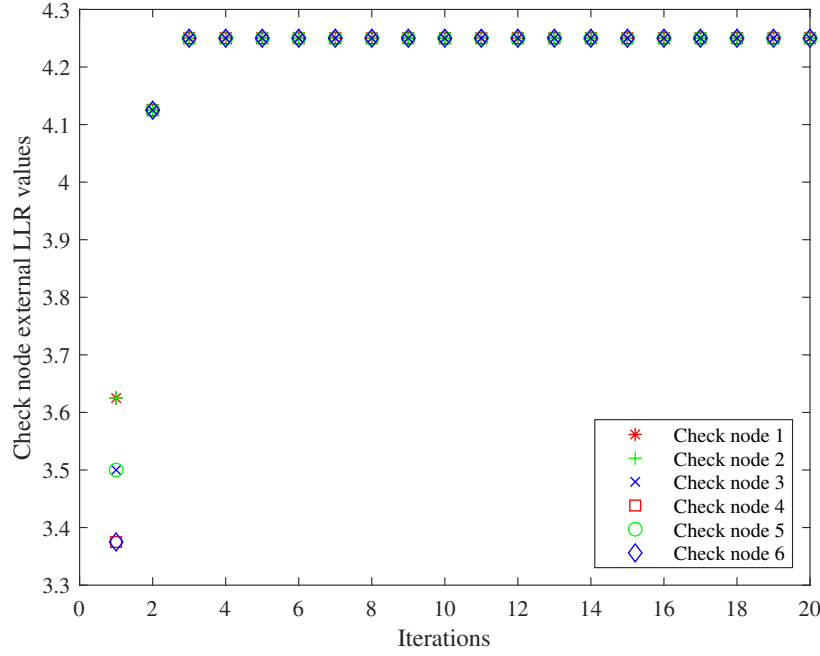
Figure 4.4: Dynamics of the external LLRs input to $\mathbb{C}(\mathbb{A})$ from outside $\mathbb{A}$ for a $(3,3)$ absorbing set of the randomly constructed $(3,6)$ code of length 1008 at $E_b/N_0 = 5$ dB.

decoded VN inputs $\mathbf{x}_i$. The numerical results shown in Figs. 4.7 and 4.8 verify this selection. However, for some LDPC codes, the $\mathbf{W}_{\text{sat}}$ based approximation of the lower bound in (4.46) can have greater values than simulations. This implies that there exist other $\mathbf{W}_k$'s which lead to correct decoding when $\mathbf{W}_{\text{sat}}$ leads to incorrect decoding. Motivated by the results in [128], [121], we consider a matrix $\mathbf{W}_{\text{linc}}$ whose entries increase linearly when decoding iterations proceed. All the entries in the tth column of $\mathbf{W}_{\text{linc}}$ have the same value w_t which increases linearly. w_t is formulated as

$$w_t = Q\left(\frac{t\Phi(0)}{T}\right), \tag{4.47}$$

where $1 \leq t \leq T$. The numerical results in Figs. 4.9 and 4.10 show the validity of the selection of $\mathbf{W}_{\text{linc}}$.

4.5 Numerical Results

In this section, we present numerical results and related discussions for the error probability performances of LDPC coded GFDM systems. The randomly constructed $(3,6)$ codes of length 1008 and length 2640 (Margulis code) [126] and array codes [119] are used to support the analyses of the FER and BER performances. For the GFDM block, K and M are configured to include a whole codeword. At least 100 frame errors were observed for each simulation. The maximum number of iterations in SPA decoding is set to 20. In calculating the decoding threshold by Gaussian approximation, the

predefined error probability level is 10^{-10}. All the numerical results are obtained using the MATLAB software.

Table 4.1: Simulation parameters for the analyses of low-E_b/N_0-region FER estimations (Figure 4.5)

Parameters	Code of length 1008	Margulis code
Channel	AWGN	AWGN
K	48	176
M	21	15
Filter	Raised cosine	Raised cosine
Roll-off factor	0.3	0.3
Mapper	BPSK	BPSK
Decoder	SPA	SPA

Table 4.2: Simulation parameters for the analyses of the lower bounds on FER (Figures 4.6, 4.7, 4.8, 4.9 and 4.10)

Parameters	Code of length 1008	(19,3) array code
Channel	AWGN and Rayleigh ($N_{ch} = 5$)	AWGN and Rayleigh ($N_{ch} = 5$)
K	48	19
M	21	19
Filter	Raised cosine	Raised cosine
Roll-off factor	0.3	0.3
Mapper	BPSK	BPSK
Decoder	Quantized SPA	Quantized SPA
Quantization scheme	$Q_{3.2}$ and $Q_{3.3}$	$Q_{3.2}$
$\Phi(0)$	4.25	4.25

The low-E_b/N_0-region FER estimations based on P_{obs} and σ^* are shown in Fig. 4.5, in which the related simulation results are also plotted. Both the Margulis code and the randomly constructed $(3,6)$ code of length 1008 are used. Related simulation parameters are summarized in Table 4.1. No quantization is considered in SPA decoders for Fig. 4.5. The FER performance of the uncoded GFDM system is shown for comparison. The uncoded GFDM system has the same simulation settings as in the case of the $(3,6)$ code of length 1008 except that the SPA decoder is not used. It is shown that LDPC coded GFDM systems have obviously improved FER performance compared to the uncoded system, and a longer code can provide lower FER values. It can be seen that in the low E_b/N_0 region, the FER estimations are close to the simulations. For example, at $FER = 10^{-3}$, the differences between the estimations and simulations are around 0.33 dB and 0.06 dB for code lengths of 1008 and 2640, respectively. The estimation accuracy gets better as the code length increases.

Fig. 4.6 shows the BER performances of LDPC coded GFDM systems, where the performance of an uncoded GFDM system is also incorporated for ease of comparison. The related simulation parameters are shown in Table 4.2. The randomly constructed $(3,6)$ code of length 1008 is used, and both
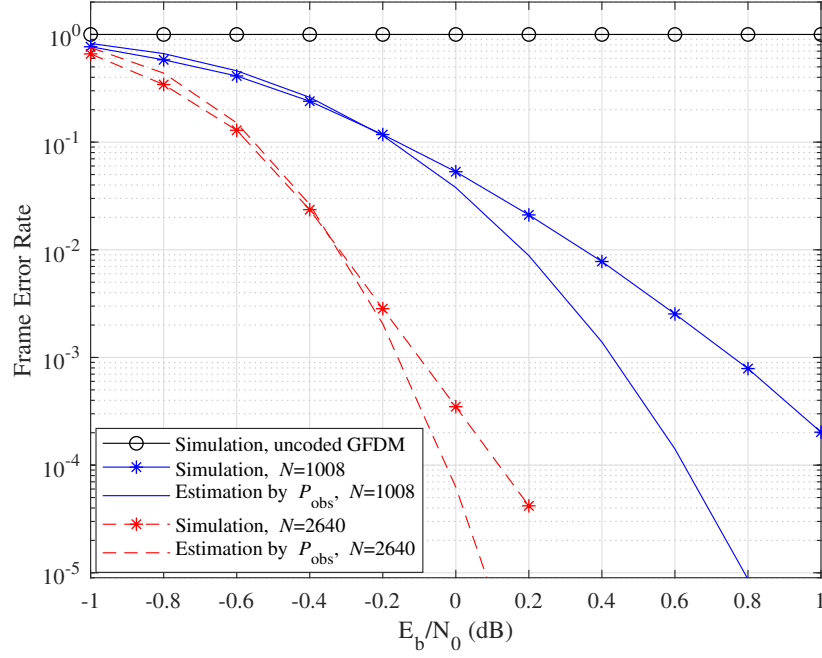
Figure 4.5: FER performance of LDPC coded GFDM systems in the low E_b/N_0 region. Both the Margulis code and the randomly constructed $(3,6)$ code of length 1008 are used.
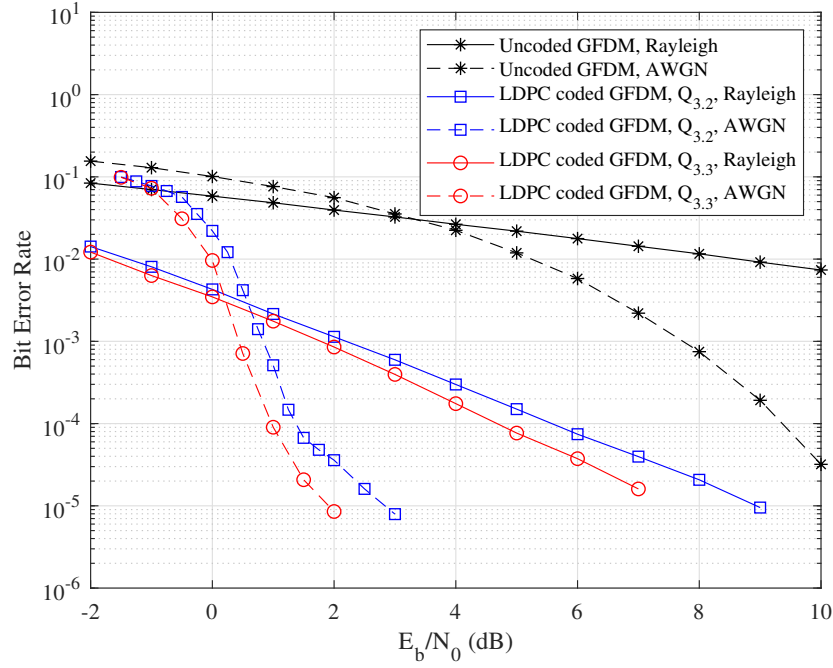

Figure 4.6: BER performances of LDPC coded GFDM systems with different quantized SPA decoders. The LDPC code used here is the randomly constructed $(3,6)$ code of length 1008.

Rayleigh and AWGN channels are considered. We can see that the LDPC coded GFDM systems have substantially improved BER performance compared to the uncoded case for both Rayleigh and AWGN channels. It can also be seen that for AWGN channels, quantized SPA decoders can exhibit error floors when E_b/N_0 increases to a certain value. For Rayleigh channels, no error floors are observed in the E_b/N_0 range in Fig. 4.6. The BER decreases as the number of quantization bits increases, which agrees with the common observations in the literature.
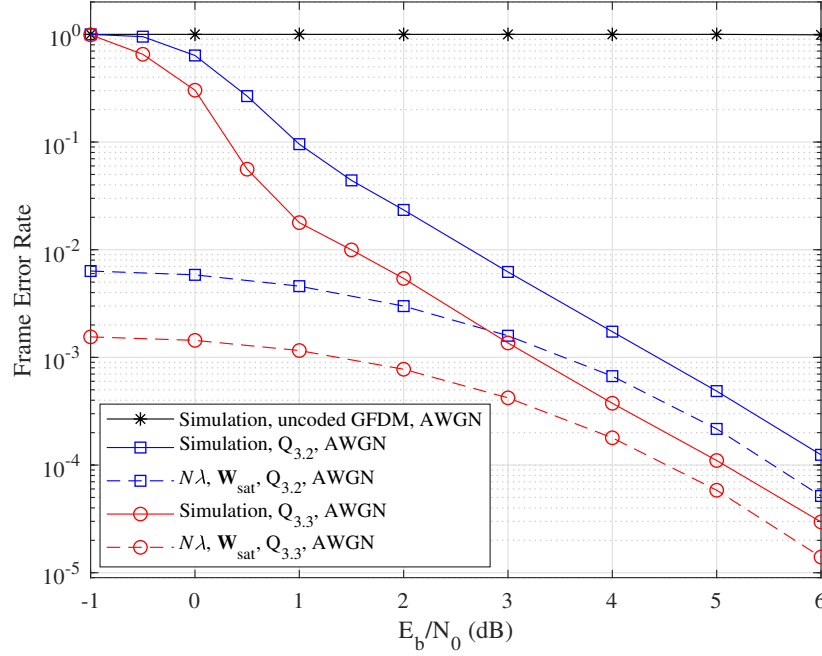
Figure 4.7: Lower bounds on the FER of the LDPC coded GFDM system with a $(3,6)$ code of length 1008 over AWGN channels. In the legend, $N\lambda$ is used to denote $N\lambda\,(\mathbb{A})$ for convenience.

The proposed lower bounds on the FER of the LDPC coded GFDM system over AWGN and Rayleigh channels are shown in Figs. 4.7 and 4.8, respectively. Simulation results of an uncoded GFDM system are also shown for comparison. Related simulation parameters can be found in Table 4.2. The code used here is the randomly constructed $(3,6)$ code of length 1008. The lower bounds are based on $(3,3)$ absorbing sets whose multiplicity in the code is 153 [129]. It can be seen that the LDPC coded GFDM system has smaller FER than the uncoded system. Similar to the case of BER, the FER performance improves as the number of quantization bits increases. It is shown that the proposed lower bounds are valid for both $Q_{3.2}$ and $Q_{3.3}$ quantization schemes. For the region $E_b/N_0 \geq 4$ dB in Fig. 4.7 and the region $E_b/N_0 \geq 8$ dB in Fig. 4.8, the lower bounds can be used as estimates of the FER with acceptable accuracy. For example, for FER at 10^{-4} in Fig. 4.7, the difference between the bound and the simulated value is around 0.5 dB when using a $Q_{3.3}$ quantizer. However, in the lower E_b/N_0 region, the lower bounds cannot be used to estimate the FER because they obviously diverge from the simulations. This divergence is due to the fact that the contribution of the $(3,3)$ absorbing set to incorrect decoding is not
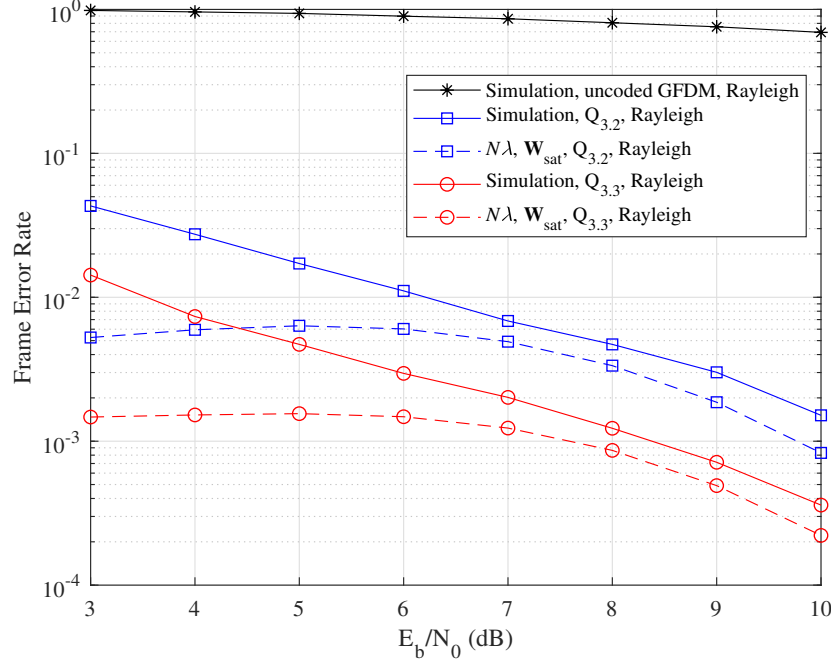
Figure 4.8: Lower bounds on the FER of the LDPC coded GFDM system with a $(3,6)$ code of length 1008 over Rayleigh channels. In the legend, $N\lambda$ is used to denote $N\lambda(\mathbb{A})$ for convenience.

the only factor in the lower E_b/N_0 region where the high FER is mainly attributed to the strong noise.

The FER performances of the GFDM system with a $(19,3)$ array code over AWGN and Rayleigh channels are shown in Figs. 4.9 and 4.10, respectively. Again, the simulated FERs of an uncoded GFDM system are incorporated for comparison. Related simulation parameters are summarized in Table 4.2. The lower bounds are based on $(3,3)$ absorbing sets whose multiplicity is 6498. It is shown that the GFDM system with a $(19,3)$ array code has lower FER compared to the uncoded case. We can see that for both AWGN and Rayleigh channels, the bound $N\lambda(\mathbb{A})$ can exceed the simulation in some E_b/N_0 region when $\mathbf{W}_{\text{sat}}$ is selected. However, $N\lambda(\mathbb{A})$ is a lower bound on FER when $\mathbf{W}_{\text{linc}}$ is used. For AWGN channels, this lower bound closely follows the simulation in the high E_b/N_0 region and thus, can act as an estimate of the FER. However, for Rayleigh channels, the difference between the lower bound and simulation cannot be neglected.

4.6 Conclusion

GFDM mudulation can provide flexible waveforms for future wireless systems due to its block based structure and the introduction of the filtering operation. LDPC codes have shown excellent asymptotic performances that are close to the Shannon limit and iterative message-passing decoders, such as SPA decoder, make their practical applications more feasible. Applying LDPC codes to GFDM systems can substantially improve the error probability performances. In adddition, the quantization scheme has an
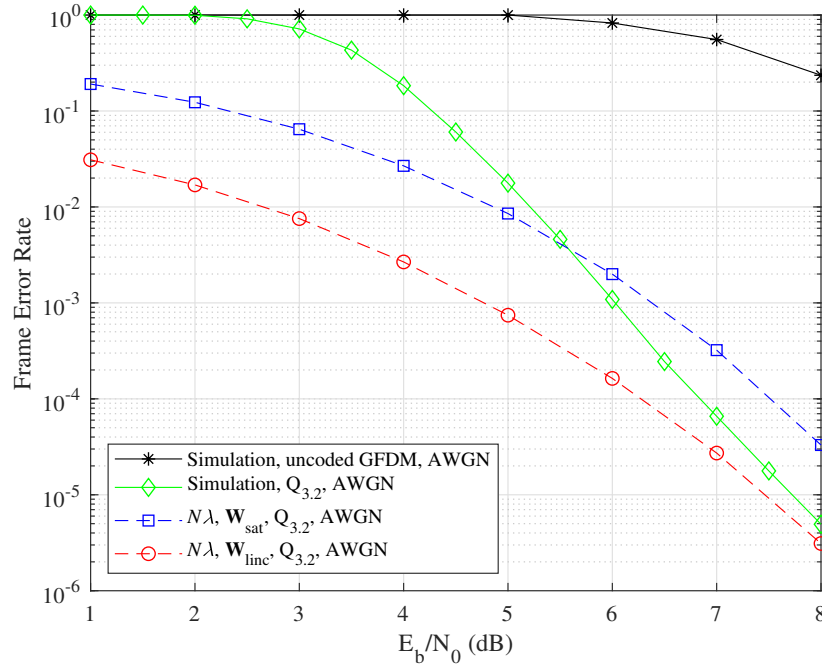
Figure 4.9: FER performance of the LDPC coded GFDM system with a (19,3) array code over AWGN channels. In the legend, $N\lambda$ is used to denote $N\lambda\left(\mathbb{A}\right)$ for convenience.
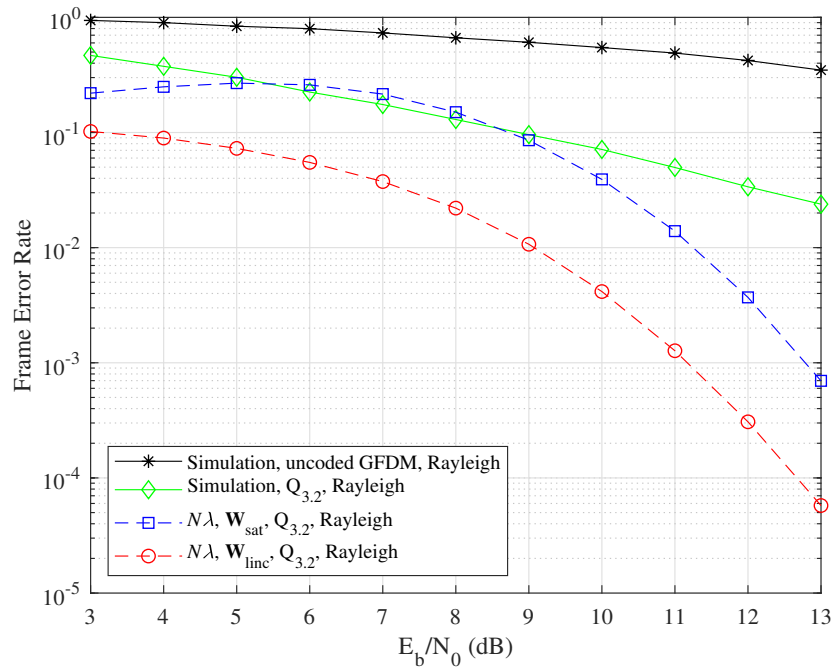

Figure 4.10: FER performance of the LDPC coded GFDM system with a (19,3) array code over Rayleigh channels. In the legend, $N\lambda$ is used to denote $N\lambda\left(\mathbb{A}\right)$ for convenience.

important impact on the performance of practical SPA decoders. Absorbing sets of the LDPC codes are identified as the main cause of the error floors for some codes. This chapter first derived the initial LLR expressions for the SPA decoders in LDPC coded GFDM systems. Then, based on the decoding threshold, we estimated the FER in the low E_b/N_0 region by considering the observed BER. This estimation method is valid for AWGN channels. Finally, we proposed a lower bound on the FER based on the absorbing sets when quantized SPA decoders are used. Both Rayleigh and AWGN channels are considered in deriving the lower bound. The numerical results reveal that the proposed FER estimation is efficient for the performance analysis in the low E_b/N_0 region and that the lower bound is valid for different quantized SPA decoders. The bound can be used to estimate the FER of the investigated codes in the high E_b/N_0 region for AWGN channels. In the case of Rayleigh channels, the lower bound can only estimate the FER performance of some selected code. The proposed estimation approach and lower bound for the FER can be used to efficiently evaluate the error probability performances of LDPC coded GFDM systems. A future work could be the joint design of the GFDM modulation and LDPC codes to lower the error floors.

Conclusion

In this thesis, we investigated GFDM-based systems. MIMO, massive MIMO and LDPC codes were integrated into the systems. For each case, we provided a system model and then analyzed the system performance or propose new algorithms. Under the assumption of ML detection, a union bound on the BER was derived for MIMO-GFDM systems based on exact PEPs. The MGF was used in order to calculate the exact PEP. The Kronecker model and an additive model were used to describe the spatial correlation and channel estimation errors in the multipath MIMO channel, respectively. This union bound provides an upper bound which can serve as a reference for the future design of MIMO-GFDM systems. Numerical results show that both the spatial correlation and channel estimation errors have important impacts on the BER performance and the derived bound. To be specific, the bound increases as the correlation strength or the variance of channel estimation errors increases. For massive MIMO-GFDM systems, low-complexity channel estimators and precoders were proposed based on polynomial expansion. The cubic computational complexity was reduced to square order due to the use of the technique of polynomial expansion. The performances of the channel estimators and precoders improve as the polynomial degree increases. However, in the meantime, a larger polynomial degree will increase the computational complexity. Therefore, there is a trade-off in determining the value of the polynomial degree. For a given polynomial degree value, the MSE of the proposed channel estimators reaches a limit as E_s/N_0 increases which implies that the MSE cannot be lower than a certain value as the channel quality improves. From another aspect, this limit can act as a tool in predicting the performance of estimators in the high E_s/N_0 region. We also analyzed the error probability performance of LDPC coded GFDM systems. The initial LLRs were first derived for the system model in question. Then, the FER in the low E_b/N_0 region was estimated based on the decoding threshold, where the channel variations were modeled through the observed BER. A lower bound on the FER was proposed based the absorbing sets when quantized SPA decoders are assumed. Numerical results indicate that the introduction of LDPC codes in GFDM systems substantially improve the error probability performance. The lower bound can be an estimate of the FER in the error-floor region when the absorbing set used is dominant and its multiplicity in the code is known.

Presented below are some interesting research directions that are worth investigating in the future. These investigations can further extend the work in this thesis. We considered Rayleigh fading channels in analyzing MIMO-GFDM systems in Chapter 2. However, other multipath fading channels can be further investigated, such as Rician, Nakagami, Beaulieu-Xie, etc. Although the precoders proposed

in Chapter 3 can relieve the signal processing burden at the user terminal, the receiver may still be complex for massive MIMO-GFDM systems. Therefore, the design of low-complexity receivers is an important topic to study. In Chapter 4, we analyzed the error probability performance of LDPC coded GFDM systems over AWGN and Rayleigh fading channels. Analyses of these systems over other fading channels, such as Nakagami and Rician channels, are also necessary and interesting due to the fact that GFDM is one of MCM schemes and powerful in mitigating multipath fading and narrowband interference. In addition, performance analyses of LDPC coded GFDM systems over channel models in 5G specifications are of practical importance. As seen in the literature, finite-length LDPC codes usually exhibit error floors in the high E_b/N_0 region. Therefore, in the future, joint design of GFDM modulation and LDPC codes can be investigated to lower the error floors.

Bibliography

[1] N. Michailow, M. Matthé, I. S. Gaspar, A. N. Caldevilla, L. L. Mendes, A. Festag, and G. Fettweis. Generalized frequency division multiplexing for 5th generation cellular network. *IEEE Transactions on Communications*, 62(9):3045–3061, September 2014.

[2] V. Vakilian, T. Wild, F. Schaich, S. ten Brink, and J.-F. Frigon. Universal-filtered multi-carrier technique for wireless systems beyond LTE. In *2013 IEEE Globecom Workshops*, Atlanta, GA, USA, December 2013.

[3] B. Farhang-Boroujeny. OFDM versus filter bank multicarrier. *IEEE Signal Processing Magazine*, 28(3):92–112, May 2011.

[4] X. Zhang, M. Jia, L. Chen, J. Ma, and J. Qiu. Filtered-OFDM - Enabler for flexible waveform in the 5th generation cellular networks. In *2015 IEEE Global Communications Conference (GLOBECOM)*, San Diego, CA, USA, December 2015.

[5] E. G. Larsson, O. Edfors, F. Tufvesson, and T. L. Marzetta. Massive MIMO for next generation wireless systems. *IEEE Communications Magazine*, 52(2):186–195, February 2014.

[6] L. Sanguinetti, E. Björnson, and J. Hoydis. Toward massive MIMO 2.0: Understanding spatial correlation, interference suppression, and pilot contamination. *IEEE Transactions on Communications*, 68(1):232–257, January 2020.

[7] E. Björnson, L. Sanguinetti, H. Wymeersch, J. Hoydis, and T. L. Marzetta. Massive MIMO is a reality—What is next?: Five promising research directions for antenna arrays. *Digital Signal Processing*, 94:3–20, November 2019. Special Issue on Source Localization in Massive MIMO.

[8] R. G. Gallager. Low-density parity-check codes. *IRE Transactions on Information Theory*, 8(1):21–28, January 1962.

[9] D. J. C. MacKay and R. M. Neal. Near Shannon limit performance of low density parity check codes. *Electronics Letters*, 32(18):1645–1646, August 1996.

[10] G. Fettweis, M. Krondorf, and S. Bittner. GFDM - Generalized frequency division multiplexing. In *IEEE 69th Vehicular Technology Conference (VTC Spring 2009)*, Barcelona, Spain, April 2009.

[11] B. Sklar. *Digital Communications: Fundamentals and Applications*. Prentice-Hall, New York, NY, USA, 2nd edition, 2001.

[12] M. Matthé, N. Michailow, I. Gaspar, and G. Fettweis. Influence of pulse shaping on bit error rate performance and out of band radiation of generalized frequency division multiplexing. In *2014 IEEE International Conference on Communications Workshops (ICC)*, Sydney, NSW, Australia, June 2014.

[13] N. Michailow, S. Krone, M. Lentmaier, and G. Fettweis. Bit error rate performance of generalized frequency division multiplexing. In *2012 IEEE Vehicular Technology Conference (VTC Fall)*, Québec City, QC, Canada, September 2012.

[14] Z. Zhang, S. W. Cheung, T. I. Yuk, and H. Kuo. Union bounds for BER evaluation and code optimization of space-time codes in 2-by-2 MIMO systems. In *IEEE 63rd Vehicular Technology Conference*, Melbourne, Vic., Australia, May 2006.

[15] M. K. Simon and M. S. Alouini. *Digital Communication over Fading Channels*. John Wiley & Sons, Inc., Hoboken, New Jersey, 2nd edition, 2005. Chapter 13.

[16] X.-G. Xia. A family of pulse-shaping filters with ISI-free matched and unmatched filter properties. *IEEE Transactions on Communications*, 45(10):1157–1158, October 1997.

[17] A. Kumar and M. Magarini. Improved Nyquist pulse shaping filters for generalized frequency division multiplexing. In *8th IEEE Latin-American Conference on Communications (LATINCOM)*, Medellin, Colombia, November 2016.

[18] A. Assalini and A. M. Tonello. Improved Nyquist pulses. *IEEE Communications Letters*, 8(2):87–89, February 2004.

[19] Y. Meyer. *Ondelettes et opérateurs: Ondelettes*. Actualités mathématiques. Hermann, 1990.

[20] R. Datta, N. Michailow, M. Lentmaier, and G. Fettweis. GFDM interference cancellation for flexible cognitive radio PHY design. In *2012 IEEE Vehicular Technology Conference (VTC Fall)*, Quebec City, QC, Canada, September 2012.

[21] I. Gaspar, N. Michailow, A. Navarro, E. Ohlmer, S. Krone, and G. Fettweis. Low complexity GFDM receiver based on sparse frequency domain processing. In *IEEE 77th Vehicular Technology Conference (VTC Spring 2013)*, Dresden, Germany, June 2013.

[22] M. Matthé, L. L. Mendes, and G. Fettweis. Generalized frequency division multiplexing in a Gabor transform setting. *IEEE Communications Letters*, 18(8):1379–1382, August 2014.

[23] D. Gabor. Theory of communication. *Journal of the Institution of Electrical Engineers - Part III: Radio and Communication Engineering*, 93(26):429–457, November 1946.

[24] A. Farhang, N. Marchetti, and L. E. Doyle. Low-complexity modem design for GFDM. *IEEE Transactions on Signal Processing*, 64(6):1507–1518, March 2016.

[25] T. M. Schmidl and D. C. Cox. Robust frequency and timing synchronization for OFDM. *IEEE Transactions on Communications*, 45(12):1613–1621, December 1997.

[26] A. B. Awoseyila, C. Kasparis, and B. G. Evans. Improved preamble-aided timing estimation for OFDM systems. *IEEE Communications Letters*, 12(11):825–827, November 2008.

[27] A. R. S. Bahai, B. R Saltzberg, and M. Ergen. *Multi-Carrier Digital Communications: Theory and Applications of OFDM*, pages 99–107. Springer, New York, NY, USA, 2nd edition, October 2004. Chapter 5.

[28] P.-S. Wang and D. W. Lin. Maximum-likelihood blind synchronization for GFDM systems. *IEEE Signal Processing Letters*, 23(6):790–794, June 2016.

[29] J.-H. Choi, B.-J. Lim, Y.-J. Kim, and Y.-C. Ko. Effect of timing and frequency synchronization errors on GFDM systems. In *2015 International Conference on Information and Communication Technology Convergence (ICTC)*, Jeju, South Korea, October 2015.

[30] L. Lu, G. Y. Li, A. L. Swindlehurst, A. Ashikhmin, and R. Zhang. An overview of massive MIMO: Benefits and challenges. *IEEE Journal of Selected Topics in Signal Processing*, 8(5):742 – 758, October 2014.

[31] F. Rusek, D. Persson, B. K. Lau, E. G. Larsson, T. L. Marzetta, O. Edfors, and F. Tufvesson. Scaling up MIMO: Opportunities and challenges with very large arrays. *IEEE Signal Processing Magazine*, 30(1):40–60, January 2013.

[32] C. Shepard, H. Yu, N. Anand, L. E. Li, T. Marzetta, R. Yang, and L. Zhong. Argos: Practical many-antenna base stations. In *Proceedings of the 18th annual international conference on Mobile computing and networking*, Istanbul, Turkey, August 2012.

[33] E. Björnson, J. Hoydis, and L. Sanguinetti. Pilot contamination is not a fundamental asymptotic limitation in massive MIMO. In *2017 IEEE International Conference on Communications (ICC)*, Paris, France, May 2017.

[34] M. Costa. Writing on dirty paper. *IEEE Transactions on Information Theory*, 29(3):439–441, May 1983.

[35] C. Windpassinger, R. F. H. Fischer, and J. B. Huber. Lattice-reduction-aided broadcast precoding. *IEEE Transactions on Communications*, 52(12):2057–2060, December 2004.

[36] B. M. Hochwald, C. B. Peel, and A. L. Swindlehurst. A vector-perturbation technique for near-capacity multiantenna multiuser communication-Part II: Perturbation. *IEEE Transactions on Communications*, 53(3):537–544, March 2005.

[37] J. Hoydis, C. Hoek, T. Wild, and S. ten Brink. Channel measurements for large antenna arrays. In *2012 International Symposium on Wireless Communication Systems (ISWCS)*, Paris, France, August 2012.

[38] T. L. Marzetta. Noncooperative cellular wireless with unlimited numbers of base station antennas. *IEEE Transactions on Wireless Communications*, 9(11):3590–3600, November 2010.

[39] J. Jose, A. Ashikhmin, P. Whiting, and S. Vishwanath. Channel estimation and linear precoding in multiuser multiple-antenna TDD systems. *IEEE Transactions on Vehicular Technology*, 60(5):2102–2116, June 2011.

[40] S. L. H. Nguyen and A. Ghrayeb. Compressive sensing-based channel estimation for massive multiuser MIMO systems. In *2013 IEEE Wireless Communications and Networking Conference (WCNC)*, Shanghai, China, April 2013.

[41] H. Q. Ngo, E. G. Larsson, and T. L. Marzerray. Massive MU-MIMO downlink TDD systems with linear precoding and downlink pilots. In *51st Annual Allerton Conference on Communication, Control, and Computing (Allerton)*, Monticello, IL, USA, October 2013.

[42] H. L. Van Trees. *Detection, Estimation amd Modulation Theory*, volume 1. John Wiley, New York, 1968.

[43] C. Lee, C.-B. Chae, T. Kim, S. Choi, and J. Lee. Network massive MIMO for cell-boundary users: From a precoding normalization perspective. In *2012 IEEE Globecom Workshops*, Anaheim, CA, USA, December 2012.

[44] H. Yang and T. L. Marzetta. Performance of conjugate and zero-forcing beamforming in large-scale antenna systems. *IEEE Journal on Selected Areas in Communications*, 31(2):172–179, February 2013.

[45] H. Prabhu, J. Rodrigues, O. Edfors, and F. Rusek. Approximative matrix inverse computation for very-large MIMO and applications to linear pre-coding systems. In *2013 IEEE Wireless Communications and Networking Conference (WCNC)*, Shanghai, China, April 2013.

[46] S. Zarei, W. Gerstacker, R. R. Müller, and R. Schober. Low-complexity linear precoding for downlink large-scale MIMO systems. In *IEEE 24th International Symposium on Personal Indoor and Mobile Radio Communications (PIMRC)*, London, UK, September 2013.

[47] R. M. Tanner. A recursive approach to low complexity codes. *IEEE Transactions on Information Theory*, 27(5):533–547, September 1981.

[48] W. K. Harrison, J. Almeida, M. R. Bloch, S. W. Mclaughlin, and J. Barros. Coding for secrecy: An overview of error-control coding techniques for physical-layer security. *IEEE Signal Processing Magazine*, 30(5):41–50, September 2013.

[49] Z. Tu and S. Zhang. Overview of LDPC codes. In *7th IEEE International Conference on Computer and Information Technology*, Aizu-Wakamatsu, Fukushima, Japan, October 2007.

[50] M. G. Luby, M. Mitzenmacher, M. A. Shokrollahi, and D. A. Spielman. Improved low-density parity-check codes using irregular graphs. *IEEE Transactions on Information Theory*, 47(2):585–598, February 2001.

[51] X.-Y. Hu, E. Eleftheriou, and D. M. Arnold. Regular and irregular progressive edge-growth tanner graphs. *IEEE Transactions on Information Theory*, 51(1):386–398, January 2005.

[52] Y. Kou, S. Lin, and M. P. C. Fossorier. Low-density parity-check codes based on finite geometries: A rediscovery and new results. *IEEE Transactions on Information Theory*, 47(7):2711–2736, November 2001.

[53] S. Tanno, T. Nishimura, T. Ohgane, and Y. Ogawa. A comparison of serial and parallel LLR updates for LDPC coded massive MIMO detection with belief propagation. In *2016 International Symposium on Information Theory and Its Applications (ISITA)*, Monterey, CA, USA, November 2016.

[54] Y.-M. Chen, C.-F. Lin, and Y.-L. Ueng. An LDPC-coded generalized space shift keying scheme using a codebook-assisted low-complexity massive MIMO detector. *IEEE Communications Letters*, 20(3):454–457, March 2016.

[55] S. Kudekar, T. J. Richardson, and R. L. Urbanke. Threshold saturation via spatial coupling: Why convolutional LDPC ensembles perform so well over the BEC. *IEEE Transactions on Information Theory*, 57(2):803–834, February 2011.

[56] R. M. Tanner. Convolutional codes from quasi-cyclic codes: A link between the theories of block and convolutional codes. Tech. Rep. UCSC-CRL-87-21, Univ. California, Santa Cruz, CA, USA, 1987.

[57] D. Achlioptas, H. Hassani, W. Liu, and R. Urbanke. Time-invariant LDPC convolutional codes. In *2017 IEEE International Symposium on Information Theory (ISIT)*, Aachen, Germany, June 2017.

[58] D. J. Costello, L. Dolecek, T. Fuja, J. Kliewer, D. Mitchell, and R. Smarandache. Spatially coupled sparse codes on graphs: Theory and practice. *IEEE Communications Magazine*, 52(7):168–176, July 2014.

[59] A. J. Felström and K. S. Zigangirov. Time-varying periodic convolutional codes with low-density parity-check matrix. *IEEE Transactions on Information Theory*, 45(6):2181–2191, September 1999.

[60] D. G. M. Mitchell, M. Lentmaier, and D. J. Costello. Spatially coupled LDPC codes constructed from protographs. *IEEE Transactions on Information Theory*, 61(9):4866–4889, September 2015.

[61] J. Thorpe. Low density parity check (LDPC) codes constructed from protographs. Tech. rep., JPL, California Inst. Technol. (CALTECH), CA, USA, 2003.

[62] S. Kudekar, T. Richardson, and R. L. Urbanke. Spatially coupled ensembles universally achieve capacity under belief propagation. *IEEE Transactions on Information Theory*, 59(12):7761–7813, December 2013.

[63] M. Lentmaier, D. G. M. Mitchell, G. P. Fettweis, and D. J. Costello. Asymptotically regular LDPC codes with linear distance growth and thresholds close to capacity. In *2010 Information Theory and Applications Workshop (ITA)*, San Diego, CA, USA, January 2010.

[64] D. Divsalar, S. Dolinar, C. R. Jones, and K. Andrews. Capacity-approaching protograph codes. *IEEE Journal on Selected Areas in Communications*, 27(6):876–888, August 2009.

[65] Z. Li, L. Chen, L. Zeng, S. Lin, and W. H. Fong. Efficient encoding of quasi-cyclic low-density parity-check codes. *IEEE Transactions on Communications*, 54(1):71–81, January 2006.

[66] F. R. Kschischang, B. J. Frey, and H.-A. Loeliger. Factor graphs and the sum-product algorithm. *IEEE Transactions on Information Theory*, 47(2):498–519, February 2001.

[67] Y.-C. Liang, K.-C. Chen, G. Y. Li, and P. Mahonen. Cognitive radio networking and communications: An overview. *IEEE Transactions on Vehicular Technology*, 60(7):3386–3407, September 2011.

[68] G. Wunder, P. Jung, M. Kasparick, T. Wild, F. Schaich, Y. Chen, S. T. Brink, I. Gaspar, N. Michailow, A. Festag, L. Mendes, N. Cassiau, D. Ktenas, M. Dryjanski, S. Pietrzyk, B. Eged, P. Vago, and F. Wiedmann. 5GNOW: Non-orthogonal, asynchronous waveforms for future mobile applications. *IEEE Communications Magazine*, 52(2):97–105, February 2014.

[69] G. P. Fettweis. The Tactile Internet: Applications and challenges. *IEEE Vehicular Technology Magazine*, 9(1):64–70, March 2014.

[70] G. J. Foschini and M. J. Gans. On limits of wireless communications in a fading environment when using multiple antennas. *Wireless Personal Communications*, 6:311–335, March 1998.

[71] M. Matthé, D. Zhang, and G. Fettweis. Low-complexity iterative MMSE-PIC detection for MIMO-GFDM. *IEEE Transactions on Communications*, 66(4):1467–1480, April 2018.

[72] M. Matthé, I. Gaspar, D. Zhang, and G. Fettweis. Near-ML detection for MIMO-GFDM. In *IEEE 82nd Vehicular Technology Conference (VTC2015-Fall)*, Boston, MA, USA, September 2015.

[73] M. Kiessling, J. Speidel, N. Geng, and M. Reinhardt. Performance analysis of MIMO maximum likelihood receivers with channel correlation, colored Gaussian noise, and linear prefiltering. In *IEEE International Conference on Communications (ICC'03)*, pages 3026–3030, Anchorage, AK, USA, May 2003.

[74] M. Towliat, S. M. J. Asgari Tabatabaee, and M. Rajabzadeh. A simple ML detection for coded generalized frequency division multiplexing in MIMO channels. *IEEE Transactions on Signal Processing*, 67(3):798–807, February 2019.

[75] G. Taricco and E. Biglieri. Exact pairwise error probability of space-time codes. *IEEE Transactions on Information Theory*, 48(2):510–513, February 2002.

[76] T. A. Lamahewa, M. K. Simon, R. A. Kennedy, and T. D. Abhayapala. Performance analysis of space-time codes in realistic propagation environments: A moment generating function-based approach. *Journal of Communications and Networks*, 7(4):450–461, December 2005.

[77] G. Gritsch, H. Weinrichter, and M. Rupp. A union bound of the bit error ratio for data transmission over correlated wireless MIMO channels. In *2004 IEEE International Conference on Acoustics, Speech, and Signal Processing*, Montreal, Que., Canada, May 2004.

[78] N. Costa and S. Haykin. *Multiple-Input, Multiple-Output Channel Models: Theory and Practice*. John Wiley & Sons, Inc., Hoboken, New Jersey, 2010. Chapter 3.

[79] A. Forenza, D. J. Love, and R. W. Heath. Simplified spatial correlation models for clustered MIMO channels with different array configurations. *IEEE Transactions on Vehicular Technology*, 56(4):1924–1934, July 2007.

[80] T. Gucluoglu and E. Panayirci. Performance of transmit and receive antenna selection in the presence of channel estimation errors. *IEEE Communications Letters*, 12(5):371–373, May 2008.

[81] V. Tarokh, A. Naguib, N. Seshadri, and A. R. Calderbank. Space-time codes for high data rate wireless communication: Performance criteria in the presence of channel estimation errors, mobility, and multiple paths. *IEEE Transactions on Communications*, 47(2):199–207, February 1999.

[82] B. Vucetic and J. Yuan. *Space-Time Coding*. John Wiley & Sons Ltd, West Sussex, England, 2003. Chapter 2.

[83] G. L. Turin. The characteristic function of Hermitian quadratic forms in complex normal variables. *Biometrika*, 47(1-2):199–201, June 1960.

[84] M. K. Simon and M. S. Alouini. *Digital Communication over Fading Channels*. John Wiley & Sons, Inc., Hoboken, New Jersey, 2nd edition, 2005. Appendix 9B.

[85] S. L. Loyka. Channel capacity of MIMO architecture using the exponential correlation matrix. *IEEE Communications Letters*, 5(9):369–371, September 2001.

[86] M. Matthé, D. Zhang, and G. Fettweis. Iterative detection using MMSE-PIC demapping for MIMO-GFDM systems. In *22th European Wireless Conference*, Oulu, Finland, Finland, May 2016.

[87] D. Zhang, L. L. Mendes, M. Matthé, I. M. Gaspar, N. Michailow, and G. Fettweis. Expectation propagation for near-optimum detection of MIMO-GFDM signals. *IEEE Transactions on Wireless Communications*, 15(2):1045–1062, February 2016.

[88] S. Parkvall, E. Dahlman, A. Furuskar, and M. Frenne. NR: The new 5G radio access technology. *IEEE Communications Standards Magazine*, 1(4):24–30, December 2017.

[89] H. Yin, D. Gesbert, M. Filippou, and Y. Liu. A coordinated approach to channel estimation in large-scale multiple-antenna systems. *IEEE Journal on Selected Areas in Communications*, 31(2):264–273, February 2013.

[90] Y. Liu, T. F. Wong, and W. W. Hager. Training signal design for estimation of correlated MIMO channels with colored interference. *IEEE Transactions on Signal Processing*, 55(4):1486–1497, April 2007.

[91] S. Ehsanfar, M. Matthé, D. Zhang, and G. Fettweis. A study of pilot-aided channel estimation in MIMO-GFDM systems. In *20th International ITG Workshop on Smart Antennas (WSA 2016)*, Munich, Germany, March 2016.

[92] S. Ehsanfar, M. Matthé, D. Zhang, and G. Fettweis. Theoretical analysis and CRLB evaluation for pilot-aided channel estimation in GFDM. In *2016 IEEE Global Communications Conference (GLOBECOM)*, Washington, DC, USA, December 2016.

[93] S. Ehsanfar, M. Matthé, D. Zhang, and G. Fettweis. Interference-free pilots insertion for MIMO-GFDM channel estimation. In *2017 IEEE Wireless Communications and Networking Conference (WCNC)*, San Francisco, CA, USA, March 2017.

[94] N. Shariati, J. Wang, and M. Bengtsson. Robust training sequence design for correlated MIMO channel estimation. *IEEE Transactions on Signal Processing*, 62(1):107–120, January 2014.

[95] S. Moshavi, E. G. Kanterakis, and D. L. Schilling. Multistage linear receivers for DS-CDMA systems. *International Journal of Wireless Information Networks*, 3(1):1–17, January 1996.

[96] N. L. Josse, C. Laot, and K. Amis. Efficient series expansion for matrix inversion with application to MMSE equalization. *IEEE Communications Letters*, 12(1):35–37, January 2008.

[97] N. Shariati, E. Björnson, M. Bengtsson, and Mérouane Debbah. Low-complexity polynomial channel estimation in large-scale MIMO with arbitrary statistics. *IEEE Journal of Selected Topics in Signal Processing*, 8(5):815–830, October 2014.

[98] O. Elijah, C. Y. Leow, T. A. Rahman, S. Nunoo, and S. Z. Iliya. A comprehensive survey of pilot contamination in Massive MIMO—5G system. *IEEE Communications Surveys & Tutorials*, 18(2):905–923, Second Quarter 2016.

[99] N. Fatema, G. Hua, Y. Xiang, D. Peng, and I. Natgunanathan. Massive MIMO linear precoding: A survey. *IEEE Systems Journal*, 12(4):3920–3931, December 2018.

[100] T. Parfait, Y. Kuang, and K. Jerry. Performance analysis and comparison of ZF and MRT based downlink massive MIMO systems. In *Proc. Sixth International Conference on Ubiquitous and Future Networks (ICUFN)*, pages 383–388, Shanghai, China, July 2014.

[101] A. Müller, R. Couillet, E. Björnson, S. Wagner, and M. Debbah. Interference-aware RZF precoding for multicell downlink systems. *IEEE Transactions on Signal Processing*, 63(15):3959–3973, August 2015.

[102] J. Park and B. Clerckx. Multi-user linear precoding for multi-polarized massive MIMO system under imperfect CSIT. *IEEE Transactions on Wireless Communications*, 14(5):2532–2547, May 2015.

[103] A. Müller, A. Kammoun, E. Björnson, and M. Debbah. Linear precoding based on polynomial expansion: Reducing complexity in massive MIMO. *EURASIP Journal on Wireless Communications and Networking*, 2016(Article no.: 63):1–22, February 2016.

[104] I. Gaspar, N. Michailow, A. Navarro, E. Ohlmer, S. Krone, and G. Fettweis. Low complexity GFDM receiver based on sparse frequency domain processing. In *2013 IEEE 77th Vehicular Technology Conference (VTC Spring)*, Dresden, Germany, June 2013.

[105] N. Michailow, I. Gaspar, S. Krone, M. Lentmaier, and G. Fettweis. Generalized frequency division multiplexing: Analysis of an alternative multi-carrier technique for next generation cellular systems. In *2012 International Symposium on Wireless Communication Systems (ISWCS)*, Paris, France, August 2012.

[106] S. Ehsanfar, M. Matthé, M. Chafii, and G. P. Fettweis. Pilot- and CP-aided channel estimation in MIMO non-orthogonal multi-carriers. *IEEE Transactions on Wireless Communications*, 18(1):650–664, January 2019.

[107] R. A. Horn and C. R. Johnson. *Topics in Matrix Analysis*. Cambridge University Press, 1991.

[108] Z. D. Lei and T. J. Lim. Simplified polynomial-expansion linear detectors for DS-CDMA systems. *Electronics Letters*, 34(16):1561–1563, August 1998.

[109] G. M. A. Sessler and F. K. Jondral. Low complexity polynomial expansion multiuser detector for CDMA systems. *IEEE Transactions on Vehicular Technology*, 54(4):1379–1391, July 2005.

[110] S. M. Kay. *Fundamentals of Statistical Signal Processing: Estimation Theory*. Prentice Hall, Upper Saddle River, NJ, 1993.

[111] H.-J. Zepernick and A. Finger. *Pseudo Random Signal Processing: Theory and Application*. John Wiley & Sons Ltd, West Sussex PO19 8SQ, England, November 2005. Chapter 5.

[112] T. J. Richardson and R. L. Urbanke. The capacity of low-density parity-check codes under message-passing decoding. *IEEE Transactions on Information Theory*, 47(2):599–618, February 2001.

[113] C. Di, D. Proietti, I. E. Telatar, T. J. Richardson, and R. L. Urbanke. Finite-length analysis of low-density parity-check codes on the binary erasure channel. *IEEE Transactions on Information Theory*, 48(6):1570–1579, June 2002.

[114] A. Amraoui, A. Montanari, T. Richardson, and R. Urbanke. Finite-length scaling for iteratively decoded LDPC ensembles. *IEEE Transactions on Information Theory*, 55(2):473–498, February 2009.

[115] R. Yazdani and M. Ardakani. Waterfall performance analysis of finite-length LDPC codes on symmetric channels. *IEEE Transactions on Communications*, 57(11):3183–3187, November 2009.

[116] Z. Mei, K. Cai, and G. Song. Performance analysis of finite-length LDPC codes over asymmetric memoryless channels. *IEEE Transactions on Vehicular Technology*, 68(11):11338–11342, November 2019.

[117] D. J. C. MacKay and M. S. Postol. Weaknesses of Margulis and Ramanujan-Margulis low-density parity-check codes. *Electronic Notes in Theoretical Computer Science*, 74:97–104, October 2003.

[118] T. J. Richardson. Error floors of LDPC codes. In *41st Annual Allerton Conference on Communication, Control, and Computing*, pages 1426–1435, October 2003.

[119] L. Dolecek, Z. Zhang, V. Anantharam, M. J. Wainwright, and B. Nikolic. Analysis of absorbing sets and fully absorbing sets of array-based LDPC codes. *IEEE Transactions on Information Theory*, 56(1):181–201, January 2010.

[120] L. Dolecek, P. Lee, Z. Zhang, V. Anantharam, B. Nikolic, and M. Wainwright. Predicting error floors of structured LDPC codes: Deterministic bounds and estimates. *IEEE Journal on Selected Areas in Communications*, 27(6):908–917, August 2009.

[121] H. Hatami, D. G. M. Mitchell, D. J. Costello, and T. E. Fuja. Performance bounds and estimates for quantized LDPC decoders. *IEEE Transactions on Communications*, 68(2):683–696, February 2020.

[122] M. Matthé, D. Zhang, and G. Fettweis. Low-complexity iterative MMSE-PIC detection for MIMO-GFDM. *IEEE Transactions on Communications*, 66(4):1467–1480, April 2018.

[123] M. Matthé, D. Zhang, and G. Fettweis. Sphere-decoding aided SIC for MIMO-GFDM: Coded performance analysis. In *2016 International Symposium on Wireless Communication Systems (ISWCS)*, Poznan, Poland, September 2016.

[124] W. E. Ryan and S. Lin. *Channel Codes: Classical and Modern*. Cambridge University Press, 2009. Chapter 5.

[125] F. Vatta, A. Soranzo, and F. Babich. More accurate analysis of sum-product decoding of LDPC codes using a Gaussian approximation. *IEEE Communications Letters*, 23(2):230–233, February 2019.

[126] D. J. C. MacKay. Encyclopedia of sparse graph codes. [Online] Available: `http://www.inference.org.uk/mackay/codes/data.html`, Accessed August 2020.

[127] Z. Zhang, L. Dolecek, M. Wainwright, V. Anantharam, and B. Nikolic. Quantization effects in low-density parity-check decoders. In *Proc. 2007 IEEE International Conference on Communications*, pages 6231–6237, Glasgow, UK, June 2007.

[128] S. Zhang and C. Schlegel. Controlling the error floor in LDPC decoding. *IEEE Transactions on Communications*, 61(9):3566–3575, September 2013.

[129] G. B. Kyung and C.-C. Wang. Finding the exhaustive list of small fully absorbing sets and designing the corresponding low error-floor decoder. *IEEE Transactions on Communications*, 60(6):1487–1498, June 2012.